

MODELING OF GRINDING PROCESS MECHANICS

by

DENİZ ASLAN

Submitted to the Graduate School of Engineering and Natural Sciences
in partial fulfillment of the requirements for the degree of
Master of Science

Sabanci University

July 2014

MODELING OF GRINDING PROCESS MECHANICS

APPROVED BY:

Prof. Erhan Budak

.....

(Thesis Advisor)

Assoc. Prof. Mustafa Bakkal

.....

Assoc. Prof. Bahattin Koç

.....

Assoc. Prof. Mehmet Yıldız

.....

Dr. Emre Özlü

.....

Date of Approval:

© Deniz Aslan 2014
All Rights Reserved

ABSTRACT

Grinding process is one of the most common methods to manufacture parts that require precision ground surfaces, either to a critical size or for the surface finish. In abrasive machining, abrasive tool consists of randomly oriented, positioned and shaped abrasive grits which act as cutting edges and remove material from the workpiece individually to produce the final workpiece surface. Hence it is almost impossible to achieve optimum process parameters and a repeatable process by experience or practical knowledge. In order to overcome these issues and predict the outcomes of the operation beforehand, modeling of the process is crucial.

The main aim of this thesis is to develop semi-analytical or analytical models in order to represent the true mechanics and thermal behavior of metals during abrasive machining processes, especially grinding operations. Abrasive wheel surface topography identification, surface roughness, thermomechanical and semi-analytical force models and two dimensional moving heat source temperature model are proposed. These models are used to simulate the grinding process accurately. The proposed models are more sophisticated than previous ones as they require less calibration experiments and cover wider range of possible cutting conditions. Once the wheel topography and abrasive grit properties are identified, uncut chip thickness per grain and final workpiece surface profile can be predicted. A novel thermo-mechanical model at primary shear zone with sticking and sliding contact zones on the rake face of the abrasive grit was established to predict cutting forces by assuming each of the abrasive grit similar to a micro milling tool tooth. Knowing the force and total process energy, by using two dimensional moving heat source theory, process temperatures are predicted. Moreover, an initial approach and experimental results are proposed in order to investigate and model dynamics and stability dynamics of the grinding process. All proposed models are verified by experiments and overall good agreement is observed.

Keywords: Grinding, Abrasive Wheel Topography, Surface Roughness, Thermomechanical Force Model, Temperature Model

ÖZET

Taşlama, hassas ölçü ve yüzey kalitesi gerektiren parçaların üretiminde en yaygın olarak kullanılan imalat operasyonlarından biri olarak değerlendirilmektedir. Aşındırıcı imalat operasyonlarında kullanılan kesici takım, rastgele konumlanmış ve şekillenmiş kesici parçacıklardan oluşmaktadır. Dolayısıyla deneyim ve pratik bilgiler ile en iyi süreç parametrelerini elde etmek oldukça zordur. Operasyon esnasında gözlemlenebilecek sorunların engellenebilmesi ve neticelerin önceden tahmin edilebilmesi adına, sürecin modellenmesi büyük bir önem taşımaktadır.

Bu çalışmanın ana amacı, aşındırıcı imalat süreçlerinde (özellikle taşlama) metallerin gerçek mekanik ve termal davranışlarını temsil eden yarı-analitik veya analitik modellerin geliştirilmesidir. Aşındırıcı takım yüzey topografisinin belirlenmesi, yüzey pürüzlülüğü modeli, termomekanik ve yarı-analitik kuvvet modelleri ve iki boyutlu hareket eden ısı kaynağı sıcaklık modeli sunulmuştur. Bu modeller, imalat sürecinin simülasyonunu yapabilmek ve sonuçlarını isabetli bir şekilde tahmin edebilmek adına kullanılmıştır. Sunulan modellerin daha az kalibrasyon deneyine ihtiyaç duyması ve daha fazla kondüsyon için tahmin yapabilme özellikleri dikkate alındığında, literatürde daha önce sunulan modellere göre daha kapsamlı oldukları söylenebilir. Aşındırıcı takım yüzey topografisi ve aşındırıcı parçacık özellikleri belirlendiği takdirde, parçacık başına düşen kesilmemiş talaş kalınlığı ve iş parçasının son yüzey profili tahmin edilebilmektedir. Aşındırıcı imalat yöntemine uyarlanan termomekanik model ise, her bir aşındırıcı parçacığı mikro freze takımı dişine benzeterek, birinci kayma bölgesini değerlendirmekte ve aynı zamanda aşındırıcı parçacığın talaş yüzeyinde yapışkan ve kaygan kontakt analizi yaparak kesme kuvvetlerini hesaplamaktadır. Kuvvetlerin ve operasyon esnasında açığa çıkan toplam enerjinin bilinmesi, iki boyutlu hareket eden ısı kaynağı teorisini kullanarak süreçte oluşan sıcaklıkların tahmin edilebilmesini sağlamaktadır. Ek olarak, taşlama operasyonu dinamiğinin modellenebilmesi adına bir ilk yaklaşım modeli önerilmiş ve deneyler yapılmıştır. Tüm önerilen modeller deneyler ile doğrulanmış ve karşılaştırmalar sonucu hesap edilen değerlerin deney sonuçlarıyla oldukça yakın olduğu gözlemlenmiştir.

Anahtar Kelimeler: Taşlama, Aşındırıcı Takım Topografisi, Yüzey Pürüzlülüğü, Termomekanik Kuvvet Modeli, Sıcaklık Modeli

ACKNOWLEDGEMENTS

Foremost, I would like to offer my sincere gratitude to my advisor Prof. Erhan Budak who has supported me throughout my M.Sc. thesis with his patience and immense knowledge. It was a great privilege for me to work with him. I learned a lot from his extraordinary view of life and open minded and eager motivation to conduct cutting edge research. Not only his valuable scientific guidance, but also the encouragements he provided me through my academic and social life made me who I am right now.

I would also like to thank the members of my committee; Assoc. Prof. Mustafa Bakkal, Dr. Emre Özlü, Assoc. Prof. Bahattin Koç and Assoc. Prof. Mehmet Yıldız.

I am indebted to the members of Manufacturing Research Lab (MRL). Dr. Taner Tunç, Ömer Özkırmı, Hayri Bakiođlu, Mehmet Albayrak, Ceren Çelebi, Esmâ Baytok, Veli Nakşiler, Emre Uysal, Utku Olgun and Alptunç Çomak have always helped and supported me during my master study.

I greatly appreciate the assistance of the technicians of MRL; Mehmet Güler and Tayfun Kalender. They were always available for helping the preparations of the verification experiments.

Finally, I am most thankful to my family, Güven, Gülser and Helin Su Aslan for their sacrifice, continuous support and understanding during the course of this study. I dedicate this work to them.

TABLE OF CONTENTS

1	CONTENTS	
2	INTRODUCTION.....	1
2.1	Introduction and Literature Survey	1
2.2	Objective	10
2.3	Layout of the Thesis	14
3	Identification of Abrasive Wheel Topography and Grain Properties	15
3.1	Wheel Surface and Grain Measurements	15
3.2	Simulation of Abrasive Wheel Topography	22
3.3	Abrasive Grain Analysis.....	25
4	Surface Roughness and Uncut Chip Thickness Calculation	27
4.1	Calculation of Uncut Chip Thickness per Grain	27
4.2	Workpiece Surface Roughness Model	30
4.3	Measured and Predicted Surface Profile and Roughness	34
5	Semi-Analytical Force Model	40
5.1	Modeling of the Process Forces	41
5.2	Prediction of Chip Flow Angle.....	47
5.3	Identification of the Ploughing Forces	48
5.4	Measured and Predicted Process Forces.....	50
6	Thermo-mechanical Force & Dual-Zone Contact Model.....	54
6.1	Dual-Zone Contact Theory and Grinding Approach.....	55
6.2	Sticking and Sliding Contact Length Identification	57
6.3	Sliding and Apparent Friction Coefficients and Forces	58
6.4	Sliding Friction Coefficient Identification and Ploughing Forces.....	59
6.5	Johnson-Cook Material Model Parameters	62
6.6	Shear Angle Predictions	63
6.7	Identification of Contact Length Between Grit and Chip.....	63
6.8	Measured and Predicted Cutting Forces.....	65
7	Temperature Model	69
7.1	Total Heat Generated in Cutting Process	70
7.2	Heat Generated in the Primary and Secondary Shear Zones.....	71
7.3	Heat Transferred into the Workpiece Material.....	72
7.4	Finite Difference Model for Temperature Distribution on Workpiece	74

7.5	Simulation of Grinding Temperature	75
7.6	Temperature Experiment Setup.....	76
7.7	Contact Length Identification.....	77
7.8	Results for Measured and Calculated Temperatures	79
8	An Initial Approach to the Dynamic Modeling of the Grinding Processes.....	84
8.1	Single Tooth Approach for Abrasive Wheel	86
8.2	Multi Teeth Approach for Abrasive Wheel.....	88
8.3	Abrasive Wheel - Milling Cutter Tool Analogy.....	89
8.4	Identification of the Abrasive Wheel Modal Parameters	90
8.5	Stability Diagram and Experiment Results	91
9	Suggestions for Further Research.....	94
10	Discussions and Conclusions	96

LIST OF FIGURES

Figure 2.1: Grinding operation and an Alumina wheel	2
Figure 2.2: Abrasive grit and chip removed from workpiece.....	3
Figure 2.3: The three deformation zones in orthogonal cutting	3
Figure 2.4: Wheel kinematics and cutting grit trajectories [11]	6
Figure 2.5: Abrasive grain shapes generally used in the literature.....	6
Figure 2.6: Illustration of the surface grinding process.....	9
Figure 2.7: SAM operation and a CBN wheel	11
Figure 3.1: Areal confocal 3D measurement system.....	15
Figure 3.2: Surface of a SiC 80 M Wheel	16
Figure 3.3: Surface of an Alumina 60 M Wheel	16
Figure 3.4: Abrasive grain per mm ² “C” parameter identification for SiC Wheel	17
Figure 3.5: C parameter identification for Alumina Wheel.....	17
Figure 3.6: Abrasive grit identification by height analysis	18
Figure 3.7: Peak count of abrasive grit heights (SiC 80 M wheel)	18
Figure 3.8: The grain distribution within the abrasive wheel [28]	19
Figure 3.9: Peak count of abrasive grit heights (Alumina 60 M wheel).....	19
Figure 3.10: 50x lens that is used for grit scans	20
Figure 3.11: Samples for scanned grains.....	20
Figure 3.12: Rake and oblique angle distribution for SiC 80 M wheel.....	21
Figure 3.13: Abrasive wheel topography (SiC 80 M wheel).....	23
Figure 3.14: Abrasive wheel topography (Alumina 60 M wheel).....	23
Figure 3.15: Single groove topography (SiC 80 tool)	25
Figure 3.16: Sample rake angle identification.....	26
Figure 4.1: Trajectory and penetration depth of a single grit	28
Figure 4.2: Grit trajectory and chip thickness variation due to the trochoidal movement	29
Figure 4.3: Wheel topography for surface roughness analysis.....	31
Figure 4.4: Abrasive grain trajectories (2 sets included).....	32
Figure 4.5: (a) Experimental setup (b) Dressing operation	34
Figure 4.6: (a) Groove1-B (b) Groove2-C (d) Groove 3-D type wheels.....	35
Figure 4.7: Groove marks on final workpiece surface for Wheel b (feed = 0.11 mm/rev & a = 0.1) .	35
Figure 4.8: Ra for abrasive wheel types (a = 0.1 mm)	36
Figure 4.9: Ra values for regular wheel	37
Figure 4.10: R _a values for X and Y direction – Regular Wheel (a = 0.1 mm)	38
Figure 4.11: Measured and simulated surface profiles for regular and A type wheels	39
Figure 4.12: Scanned single point diamond dresser tip.....	40
Figure 5.1: Grit engagement section and division into sections.....	44
Figure 5.2: Groove profile on the wheel (dressing tool tip)	44
Figure 5.3: Tangential (black), feed (green) and radial (red) directions	45
Figure 5.4: Oblique cutting diagram	45
Figure 5.5: Orthogonal cutting force diagram.....	46
Figure 5.6: Ploughing force identification.....	48
Figure 5.7: Three phases for grit-workpiece interaction	49
Figure 5.8: Setup for force experiments	50

Figure 5.9: (a) Force measurement devices (b) Dressing tool.....	51
Figure 5.10: Experimental & Model Results (Total Forces).....	52
Figure 5.11: Experimental & Model Results (Average forces per grit)	52
Figure 6.1: Chip flow and the pressure distribution on the grit rake face	57
Figure 6.2: Sliding friction coefficient for AISI 1050 steel and SiC abrasive material	60
Figure 6.3: Ploughing force identification for $V_c = 7.85$ m/s	61
Figure 6.4: Ploughing force identification for $V_c = 12.57$ m/s	61
Figure 6.5: Ploughing force identification for $V_c = 15.71$ m/s	61
Figure 6.6: Ploughing force identification for $V_c = 19.63$ m/s	62
Figure 6.7: Ploughing force identification for $V_c = 24.74$ m/s	62
Figure 6.8: Measured and predicted shear angle comparison ($feed_r = 0.11$ mm/rev, $a = 0.03$ mm)	63
Figure 6.9: Stuck material on scanned grains.....	64
Figure 6.10: Regions where stuck material is observed	64
Figure 6.11: Total and sticking contact lengths on the rake face of the grit.....	65
Figure 6.12: Comparison of experimental and predicted results for 7.85(m/s) cutting speed ($a = 0.1$ mm)	66
Figure 6.13: Comparison of experimental and predicted results for 19.63(m/s) cutting speed ($a = 0.1$ mm)	66
Figure 6.14: Comparison of wheel types (0.11 mm/rev feed).....	67
Figure 6.15: Radial forces ($feed_r = 0.11$ mm/rev)	67
Figure 6.16: Comparison of cutting forces with different cutting speeds ($feed_r = 0.11$ mm/rev, $a = 0.03$ mm)	68
Figure 6.17: Comparison of cutting forces per grit with different cutting speeds ($feed_r = 0.11$ mm/rev, $a = 0.03$ mm)	68
Figure 7.1: Orthogonal cutting schematic and Scanning the contact zone between wheel and workpiece	71
Figure 7.2: Contact length heat input to the workpiece material.....	72
Figure 7.3: Contact zone between wheel and workpiece [51].....	73
Figure 7.4: Triangular heat source and meshes on the workpiece [24]	74
Figure 7.5: Experiment setup during operation and the thermocouple junction with the w.p.....	76
Figure 7.6: Thermocouple fixation diagram and exposed thermocouple junction after an operation...	77
Figure 7.7: Comparison of contact lengths identified by geometrical formulation and thermocouple measurement ($feed_r = 0.18$ mm/rev).....	78
Figure 7.8: Comparison of contact lengths identified by geometrical formulation and thermocouple measurement ($feed_r = 0.15$ mm/rev)	78
Figure 7.9: Comparison of contact lengths identified by geometrical formulation and thermocouple measurement ($feed_r = 0.11$ mm/rev)	78
Figure 7.10: Forces for 12th and 5th operations.....	80
Figure 7.11: Workpiece surface inspection	80
Figure 7.12: Surface 3(Figure 7.11) observed operation.....	81
Figure 7.13: Experiment and simulation result for test 12 (dry)	81
Figure 7.14: Experiment and simulation result for test 12 (wet).....	82
Figure 7.15: Simulation results for different process parameters.....	83
Figure 7.16: Measured and predicted temperatures.....	83
Figure 7.17: Surface burn observed operation and wheel condition afterwards	84

Figure 8.1: Abrasive wheel 1DOF.....	86
Figure 8.2: Dynamic milling process	88
Figure 8.3: Scanned grains for cluster (tooth) identification.....	89
Figure 8.4: FRF measurement of the abrasive wheel (X and Z directions, respectively)	90
Figure 8.5: Modal parameters for the wheel illustrated in (Figure 8.4)	90
Figure 8.6: Modal parameters of the spindle and tool holder.....	91
Figure 8.7: Stability diagram and sample experiments	91
Figure 8.8: Experiments for stability diagram validation.....	92
Figure 8.9: Sound measurement from operation 6	92
Figure 8.10: Measured force for operation 6.....	92
Figure 8.11: Wheel condition after operation 6.....	93
Figure 8.12: Stability diagram for a Alumina 60 M wheel	93

LIST OF TABLES

Table 2.1: Geometrical properties of abrasive grits for SiC 80 M wheel.....	21
Table 2.2: Geometrical properties of abrasive grits for Alumina 60 M wheel.....	22
Table 3.1: Flowchart for a surface roughness model.....	33
Table 3.2: Dressing conditions.....	34
Table 4.1: Identified cutting coefficients.....	51
Table 4.2: Ploughing forces for 3 directions	53
Table 4.3: Process Parameters and Shear Angle-Stress Results.....	53
Table 5.1: Johnson-Cook Parameters for AISI 1050 Steel [22]	62
Table 5.2: Selected experiments to present dual zone model results	64
Table 6.1: Temperature simulation methodology.....	75
Table 6.2: Temperature and μ results.....	79
Table 6.3: Chip temperature and Frictional force calculation between tool & chip.....	82

2 Introduction

2.1 Introduction and Literature Survey

The grinding process is one of the oldest methodologies to shape materials, dating from the time prehistoric man discovered that he could sharpen his tools by rubbing them against gritty rocks. Capability to shape and sharpen their tools enabled people to survive and make progress. It can be said that Stone Age people were the first abrasive engineers. We still use abrasives in our everyday lives without even giving them a second thought. Even the toothpaste that we use every day to brush our teeth contains a very mild abrasive like hydrated silica which helps to clean our teeth. Detergents that are used to clean our houses have silica or calcium carbonate which is milder abrasives.

Apart from their daily usage, abrasives and their capability to shape materials become popular in early nineteenth century with Henry Ford and his desire for mass production. Milling, turning and other machining processes were not accurate enough for precision requirements and surface finish criteria in those days. James Watt, George Stevenson and Ford himself stated the demand for consistency, better control of size and surface finish which were essential for the improvements in design and production engineering. They discovered that abrasives deliver these results and started to use abrasive machining. Synthetic abrasives began to replace the natural abrasives of sandstone, crocus rouge and corundum. These types of abrasives are pure, consistent and can be controlled during abrasive cutter production. It was the usage of aluminum oxide and silicon carbide abrasives which brought us the modern grinding technology and more sophisticated machine tools designed for abrasive machining. By the end of nineteenth century, cubic boron nitride (CBN) and synthetic diamond abrasive particles came into the scene and introduced the Super Abrasive Machining to the manufacturing industry which has serious advantages over conventional grinding methodologies.

Nowadays, grinding is a major manufacturing process which accounts for about 20-25% of the total expenditures on machining operations. 70-75% of the precision surface finish operations are conducted by grinding operations in industry. The uniqueness of abrasive machining processes is found in its cutting tool. Grinding wheels and tools are consisted of abrasive grits and softer bond material which holds these grits together in a solid mass. Grinding is undoubtedly the least understood and most neglected machining process in

practice. People usually conduct experimental investigations or try-error methodologies rather than trying to understand the mechanism and modeling the process. Reason for that is the belief that the process is too complicated to understand or model by analytical approach. Irregular geometry of the abrasive grits and multiple cutting points in each process, high cutting speeds, depth and width of cut which vary from grit to grit can be the main actors for this belief. Because of the large number of cutting, ploughing and rubbing events occur during the process in a micro scale, it has been noted that the process can be characterized by a typical average grain which is a great simplification. That approach enabled researchers to focus more on grits and try to understand the mechanism between abrasive grits and workpiece material rather than considering the abrasive wheel as a whole. With that development, it can be said that grinding has been transformed from a practical art to an applied science [1].



Figure 2.1: Grinding operation and an Alumina wheel

The objective of today's manufacturing world is to achieve the lowest piece part cost for the desired quality and quantity of the designed components. Cutting tool and equipment costs are critical in this scope considering the cost of labor is less significant with the developments in automation and computer controlled systems. Grinding process is crucial for this philosophy since it is generally considered as a finishing operation; nevertheless process quality and process parameter selection depends to a large extent on the experience of the operator. Since abrasive wheels have a stochastic nature, even if an operator achieves optimum parameters by experience or practical knowledge; it is hard to obtain a repeatable process. In order to overcome these issues and predict the outcomes of the operation beforehand, modeling of the process is required. In order to be able to model the process, solid understanding of the process geometry, mechanics and abrasive wheel topography are required. As optical and other types of measurement systems develop, having a better insight or performing actual topography measurements of abrasive wheel surface become possible. This advancement led

researchers to agree on that each grain performs cutting action individually similar to the milling process. However, in abrasive machining, each grain has unique geometric and location properties which mean uncut chip thickness, effective axial and width of cuts per grit should be investigated individually. Therefore, it was agreed that the “average grit property” approach was not precise enough to handle the process.

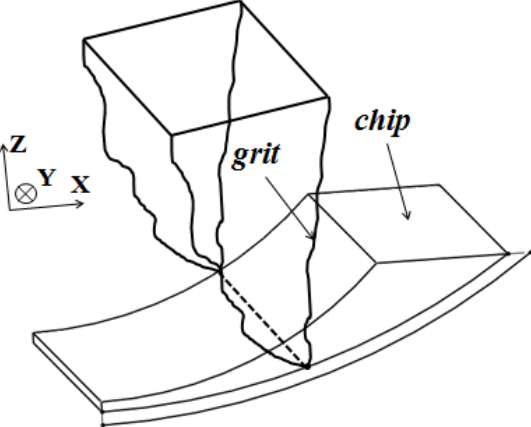


Figure 2.2: Abrasive grit and chip removed from workpiece

Understanding the chip formation mechanism is required for modeling the machining processes. There are several methods of metal cutting such as turning, milling, broaching, boring drilling etc. These types of metal cutting operations usually have their own machining tool types and classified as subtractive manufacturing. For all of these processes, cutting tool is used to remove small chips of material from the work. Although grinding operation is referred as an abrasive machining process, chip formation mechanism by abrasive grits in the micro scale is similar to macro scale machining operations. Therefore, chip formation mechanism can be modeled by using orthogonal and oblique cutting theories with some modifications.

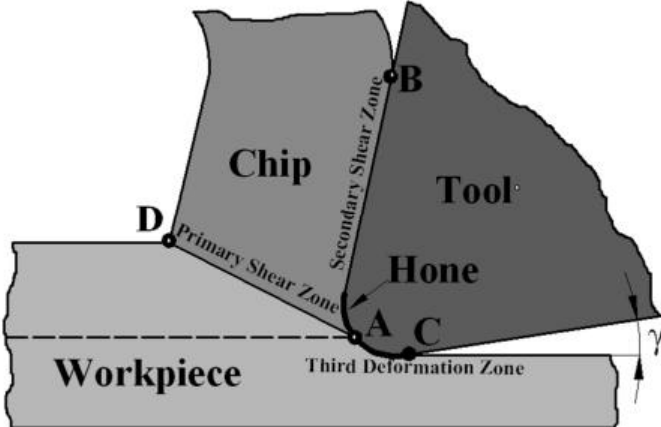


Figure 2.3: The three deformation zones in orthogonal cutting

In Figure 2.3, between A and C points, grit (tool) and workpiece are in contact, however; there is no cutting action. At the very first stage of the interaction between the abrasive grit and the material, plastic deformation occurs, temperature of the workpiece increases and normal stress exceeds yield stress of the material. After a certain point, the abrasive grit starts to penetrate into the material and starts to displace it, which is responsible for the ploughing forces. Finally, shearing action starts and the chip is removed from the workpiece [50]. Since all of the abrasive grains on the grinding wheel have unique geometrical properties, assumptions or generalizations for grain distribution over wheel and their shapes should be used to model the cutting mechanism and predict process outcomes.

The distribution and shape of the abrasive grits strongly influence the surface finish, forces, temperature and dynamics of the process. Tönshoff et al. [2] stated that the kinematics of the process is characterized by a series of statistically irregular and separate engagements. Brinksmeier et al. [3] also claimed that the grinding process is the sum of the interactions among the wheel topology, process kinematics and the workpiece properties. Abrasive wheel topography is generally investigated as a first step for modeling the abrasive machining processes. In machining operations with a defined cutting tool that are listed above, all geometrical properties of the cutting tool is known and one can focus directly to the process itself. However; in abrasive machining, in order to be able to model the chip formation mechanism and perform further analyses, identification of the wheel topography and grit properties is essential as mentioned earlier.

The wheel structure is modeled by using some simplifications such as average distance between abrasive grits and average uniform height of abrasive grits. Lal and Shaw [4] formulated the undeformed chip thickness for surface grinding in term of the abrasive grit radius and discussed the importance of the transverse curvature of the grit. Some parameters such as wheel topography related ones and material properties were often represented by empirical constants [2]. Empirical surface roughness models have had more success in the industry since they do not require abrasive wheel topography identification and further analysis [3]. However; lack of accuracy and need for excessive experimental effort are drawbacks of these models.

There are semi-analytical models to model wheel topography and predict surface roughness of the final workpiece in the literature as well [1,4,5,8,9]. They need experimental calibration of few parameters in semi-analytic formulations. Once these parameters are determined

correctly, it is claimed that wheel topography and roughness can be calculated by these methodologies. It would be an adequate approach to focus on surface roughness-profile models since they provide an insight for both wheel topography identification and final workpiece surface texture predictions.

The approach in the literature for semi-analytical models consists of two analyses, statistical and kinematic approaches. The statistical studies focus on distribution function of the grit protrusion heights whereas kinematic analyses investigate the kinematic interaction between the grains and the workpiece [5]. Hecker and Liang [6] used a probabilistic undeformed chip thickness model and expressed the ground finish as a function of the wheel structure considering the grooves left on the surface by ideal conic grains. Agarwal and Rao [7] examined the chip thickness probability density function and defined the chip thickness as a random variable. They established a simple relationship between the surface roughness and the undeformed chip thickness. These two studies can be classified as statistical analysis and for the kinematic analysis; Zhou and Xi [8] considered the random distribution of the grain protrusion heights and constructed a kinematic method which scans the grains from the highest in a descending order and solves the workpiece profile. Apart from these studies; Gong et al. [9] used a numerical analysis and utilized a virtual grinding wheel by using Monte Carlo method to simulate the process, the roughness of the surface is shown in three-dimensional images. Mohamed et. al [10] examined the circumferentially grooved wheels and showed groove effect on workpiece surface topography by performing creep-feed grinding experiments. Finally, Liu et. al [11] investigated the three different grain shapes (sphere, truncated cone and cone) and developed a kinematic simulation to predict the workpiece surface roughness. They also presented a single-point diamond dressing model having both a ductile cutting and brittle fracture component. Liu et. al [11] and Zhou and Xi [8]'s studies can be considered as the "state of the art" for surface roughness and abrasive grit shape analyses. However, they should be expanded in the sense of wheel topography identification and determination of the abrasive grit geometrical property distributions.

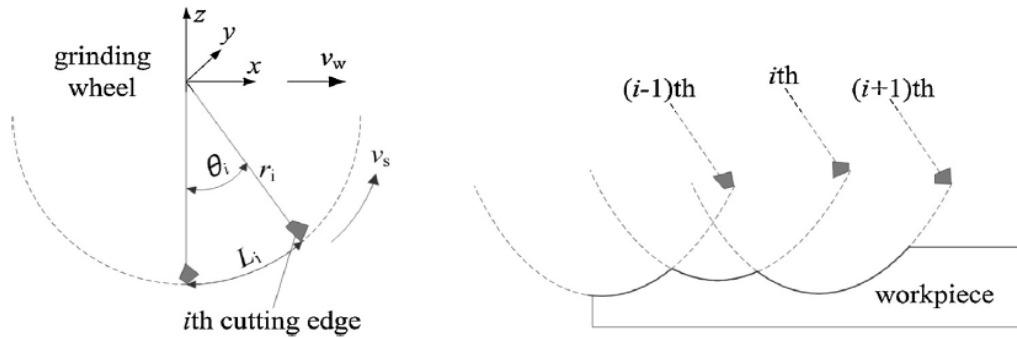


Figure 2.4: Wheel kinematics and cutting grit trajectories [11]

Abrasive grains are usually modeled as they have a certain geometrical shape such as sphere or cone for a particular abrasive material or wheel type in the literature. It is unlikely to have a certain and unique geometrical shape for all abrasive grains on a wheel considering the stochastic nature of the process and fragile structure of these grains. Assigning one of the shapes illustrated in Figure 2.5 to all of the grains is a great simplification, one may obtain satisfactory results by this approach; however, when it comes to expanding that assumption to further, ie. force, temperature or chatter vibration analyses, it can be insufficient. Therefore, complete or partial representation of all possible shapes and locations should be adapted to the process model for better and more accurate predictions.

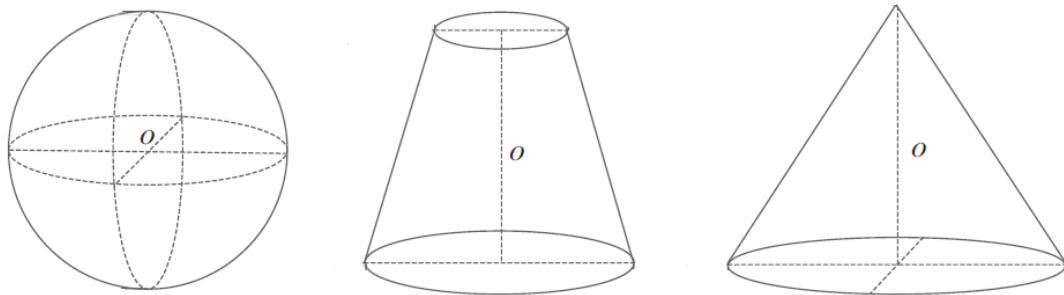


Figure 2.5: Abrasive grain shapes generally used in the literature

After obtaining the topographical properties of the wheel, studies often focus on process force investigations. S. Malkin [1] claimed that the material removal during grinding occurs as abrasive grains interact with the workpiece by presenting scanning electron microscope (SEM) results. According to his theory, material removal occurs by a shearing process of chip formation in a grit scale and although some researchers stated their opinions about similar mechanisms earlier, his theory was well supported by both experimental and theoretical evidence. His model and theories have several important assumptions, yet it is still widely used to understand the basics of the grinding process. Later, many models were proposed on the modeling of the abrasive machining processes.

To begin with the experimental or mechanistic models, Fan and Miller [12] conducted grinding experiments and calibrated constants which depend on the workpiece material, grinding wheel and several other process parameters, in the formulation. Experiments should be performed to identify these constants for different arrangements of workpiece-wheel pair and process parameters. Johnson et al. [13] determined force equations for face grinding operation by regression analysis from experimental data and identified the constants for various grinding wheel-workpiece pairs. The model is claimed to be implemented in industry quickly which is the main advantage of the experimental models. However, lack of accuracy and need for excessive experimental effort are drawbacks of these models.

There are semi-analytical force models in the literature as well. Experimental calibration of few parameters in semi-analytic formulations is also needed for these studies. Once these parameters are determined correctly, it is claimed that process forces can be calculated by presented semi-analytic force equations. Durgumahanti et al. [14] used this approach by assuming variable friction coefficient focusing mainly on the ploughing force. They established force equations for ploughing and cutting phases and need experimental calibration for certain parameters. Single grit tests were performed in order to understand the ploughing mechanism and the measured values are used to calculate the total process forces. Single grit analysis is beneficial since we can get more deterministic data about that particular grit without considering stochastic nature of them on the wheel. Chang and Wang focus more on stochastic nature of the abrasive wheel and tried to establish a force model as a function of the grit distribution on the wheel [15]. It is tricky to identify grit density function and require correct assumptions on grit locations and adequate generalizations. Hecker et al. [6] followed a more deterministic way by analyzing the wheel topography and then generalized the measured data through the entire wheel surface. Afterwards they examined the force per grit and identified the experimental constants. Kinematic analysis of grit trajectories during cutting were performed and chip thickness per grain assumed as a probabilistic random variable which is defined by Rayleigh probability density function [16]. Rausch et al. [17] focused on diamond grits by modeling their geometric and distributive nature individually rather than examining them on the abrasive wheel. Regular hexahedron or octahedron shapes of the grits are investigated and the model is capable of calculating engagement status for each grain on the tool and thus the total process forces. Koshy et al. developed a methodology to place abrasive grains on a wheel with a specific spatial pattern and examined these engineered wheels' performance [18]. Similar methods can be used to obtain the optimum

abrasive wheel for a specific operation in the future. Finally, Mohamed et. al [10] showed that the grinding efficiency can be improved considerably by lowering the forces with circumferentially grooved wheels.

In order to use the full potential of the abrasive machining and achieve higher quality and productivity, optimum selection of process parameters is required. There are several phenomena which govern the cutting process and should be evaluated for optimality; however; surface roughness and force analysis can be considered as the most essential ones since they enable us to predict the final surface topography of the workpiece and total process energy, respectively. Energy required to remove a unit volume chip from workpiece is high in grinding process compared to other operations such as turning or milling. It is generally assumed that all this energy is converted to heat in the grinding zone where the wheel interacts with the workpiece, causing very high temperatures [1]. These high temperature values cause thermal damages to the workpiece, such as surface burn, metallurgical phase transformations and undesired residual tensile stresses. Hence, total process energy has a critical role and can be predicted via presented semi-analytical or thermomechanical force model for circumferential grooved and regular (non-grooved) abrasive wheels.

High temperatures in abrasive machining cause thermal damages to the workpiece, such as surface burn, metallurgical phase transformations and undesired residual tensile stresses. Thermal damage risk is the main constraint for the grinding operations as it limits the production rates drastically. From metallurgical investigations of ground hardened steel surfaces reported in 1950, it was clearly shown that most grinding damage is thermal in origin. Five years later, first attempt to measure process temperatures and obtain the grinding temperature by embedding thermocouples into the workpiece was reported. Since that day, numerous other methods have also been used to measure grinding temperatures either by thermocouples or radiation sensors. It is a difficult task to collect temperature data from cutting zone which is generally few millimeters in wheel-workpiece interaction and few microns in abrasive grit-workpiece interaction scales. Thermocouples and infrared radiation sensors are the most commonly used devices for temperature measurement purposes in abrasive machining.

Therefore, it is crucial to understand cutting mechanism for abrasive grits on the wheel and predict process temperatures in order to prevent thermal damages to the workpiece [19]. Thermal analyses of grinding processes are usually based upon the application of moving heat

source theory. The grinding zone is modeled as a source of heat which moves along the surface of the workpiece. It is agreed that almost all the grinding energy expended (95-98%) is converted to heat at the grinding zone where the wheel interacts with the workpiece. Energy partition to the workpiece, which is the fraction of the total grinding energy transported to the workpiece as heat at the grinding zone, is a crucial phenomenon and should be identified accurately. It depends on the type of grinding, wheel and workpiece materials and process parameters.

The classical moving heat source model for sliding contacts was first studied by Jaeger [20]. Outwater and Shaw [21], used Jaeger's model for grinding operations for the first time by assuming that the contact zone between grinding wheel and the workpiece is moving along the surface of the workpiece material as given in Figure 2.6. Research focusing on abrasive grit-workpiece interaction helped understanding; chip formation and shearing mechanisms for the grinding operations better which lead to more accurate thermal analyses [22]. Therefore, grinding process temperatures can be predicted by calculating temperatures on the shear plane by adequate heat transfer models. Malkin and Guo [19] presented an extensive literature review on modeling of workpiece surface temperatures for dry grinding.

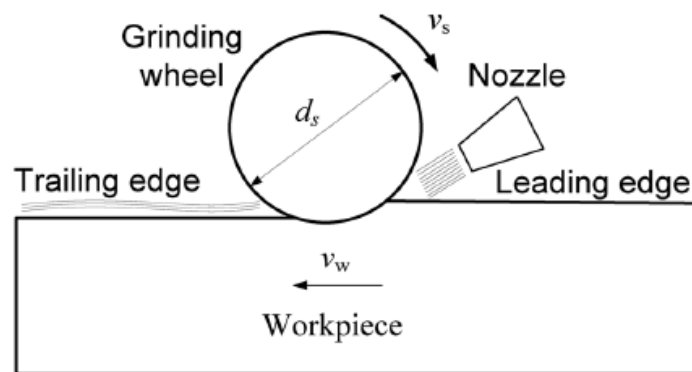


Figure 2.6: Illustration of the surface grinding process

There are several works on grain scale grinding force and heat transfer modeling [4, 10, 16]. Lavine [26] combined the micro and macro scale analysis for temperature modeling where grinding fluid was considered to be a solid moving at the wheel speed. Shen et al. [24] presented a heat transfer model based on finite difference method considering convection heat transfer on the workpiece surface in wet grinding. Later, Shen et al. [25] expanded that work by explaining their thermocouple fixation method into the workpiece, presenting their experimental results for dry, wet and MQL grinding conditions. Apart from thermocouple fixation method, Mohamed et al. [23] used infrared camera to measure process temperature

for surface grinding operations and calculated the heat flux based on average measured power. Tahlivian et al. [27] used both embedded thermocouple and high speed camera to measure total process temperature and chip thickness per abrasive grain, respectively, for robotic grinding process. Temperature distribution in the workpiece is simulated with a 3D transient thermal finite element code.

2.2 Objective

Modeling of grinding operations is needed in the selection of optimum process parameters for industrial or scientific applications. Several process models have been developed as reviewed in the previous section until now. Mechanistic or curve fit models were the most widely used ones until 21st century. They might predict the process outcomes very precisely for some cases; however, they fail to provide insight about the process itself and the number of calibration or investigation experiments to obtain the necessary database can be very high. There are studies which use numerical analysis such as FEM (finite element method) or FDM (finite difference method) which give detailed results about the process and tool-workpiece conditions. Drawback of such studies are; they require long solution times which is not desired if one wants to find the optimum process parameters by scanning a certain range [17, 24]. In addition, there are semi-analytical and analytical models which require calibration of some constants for their formulations and once they are identified, they can be used to predict process outcomes for different cases involving the same material and the abrasive grain with different conditions. However; need for calibration experiments for all wheel-workpiece pairs and cutting velocities can be considered as a weakness. There is a need for process models which are accurate and represents the cutting mechanism in a more detailed manner. In this thesis, our aim is to present semi-analytical and analytical methods which represent the true wheel properties, grinding mechanism and material behavior and eliminate the need for calibration experiments for all wheel-workpiece pairs and cutting velocities.

In addition, in case of some hard-to-machine materials grinding can also be a cost effective alternative even for roughing operations. Grinding operations that use CBN or Diamond abrasive wheels referred as Super Abrasive Machining (SAM) Operations. CBN and Diamond wheels enable higher cutting speeds, longer tool life and higher MRR for hard-to-machine materials (ie. Nickel alloys, titanium alloys). CBN grains have 55 times higher thermal conductivity, 4 times higher the abrasive resistance and twice the hardness of the aluminum oxide abrasives. These properties make SAM wheels well suited for the grinding of

high-speed and super-alloy materials. It is believed that this thesis provides a basis for modeling of SAM operations, considering their similar mechanism with conventional grinding processes.



Figure 2.7: SAM operation and a CBN wheel

In this study, wheel topography and geometrical properties of abrasive grains (i.e. rake and oblique angle, edge radius, width and height) are identified for an abrasive wheel. Their distribution over the wheel is identified by scanning sufficient number of grains and considering their locations over a wheel. Rather than using a single average value for these geometrical parameters, a Gaussian distribution is constructed by identifying the mean and standard deviation of them. Random values from these distributions are assigned to each abrasive grain which means every one of them has unique rake, oblique angle, edge radius, width and height. It is believed that the presented approach is more realistic than assigning a single average value for each of these parameters to all grains.

After topographical identification and grain scanning is done, wheel surface is simulated, hence calculation of final workpiece surface profile and uncut chip thickness per grain become possible. Final workpiece surface profile is obtained through kinematic analysis of abrasive grains' trajectories. It was checked for each abrasive grain that whether it is active or not in the sense of chip formation by cut-off weight analysis. Trajectory of an abrasive grit is calculated and its intersection with the work material is obtained. Volume of the grit that lies inside of the grit penetration depth is subtracted from the workpiece. Same operation is done for each grain by considering its trochoidal movement along the surface. Uncut chip thickness and created surface texture differs for each abrasive grain since their geometric properties are not identical. Such comprehensive representations for wheel topography and grain distribution are essential since it is the basis of all presented models. In addition, once these identifications are done carefully for a regular wheel with a certain abrasive type, it is possible to predict

process outcomes for all variations of that wheel geometry (ie. radial or circumferentially grooved, segmental etc.) which is a noteworthy development.

Being able to calculate uncut chip thickness and knowing the geometrical properties of each abrasive grain lead us to force analyses. In this study, two separate force models are developed; first one is semi-analytical, uses micro-milling analogy and easier to implement. It requires more calibration experiments compared to the second one. Second one is thermomechanical and considers the material behavior by using Johnson-Cook material model which is harder to implement. However, number of calibration experiments for the thermomechanical model is considerably low and once the model is calibrated, it covers all possible variations of process parameters, wheel geometry and grit distributions for a particular abrasive type (ie. SiC, Alumina).

For the semi-analytical force model, equations for total normal and tangential force components as well as average force per grit are established by using the micro milling analogy. Fundamental parameters such as shear stress and friction coefficient between the grits and the work material are identified. Easy implementation and milling analogy can be considered as the main advantages. It was stated in the literature that grinding is similar to a milling process in the sense of multiple cutting teeth [22]. However, there were not many studies in the literature related to that assumption, using milling equations with some modifications and obtaining reasonable results showed that this model can be expanded further by using similar chip formation mechanism.

Lack of analytical models for abrasive machining and observation of similar chip mechanism with milling process lead us to construct a thermomechanical force model which gives more insight about the cutting process. A novel thermo-mechanical model at primary shear zone with sticking and sliding contact zones on the rake face of the abrasive grit was established. Rather than using geometrical contact length, more accurate contact length is obtained by measuring grinding temperature during the process. Majority of the semi-analytical force models presented in the literature, also in this thesis, require calibration of certain coefficients for each cutting velocity and a particular wheel-workpiece pair. By utilizing thermo-mechanical analyses and Johnson-Cook material model, a few calibration tests for an abrasive type-workpiece pair is sufficient to predict process forces for different cases involving the same workpiece and the abrasive material however with different arrangements and process parameters. It was thought that micro milling analogy and modeling of abrasive grits'

kinematic trajectories will also be useful in expanding this model to thermal and stability analyses which appeared to be a nice idea. Thermal analyses can be considered as the most crucial research area for abrasive machining due to very high process temperatures. A methodology is proposed to detect whether there will be a surface burn over workpiece material or not by 2D moving heat source theory. As mentioned earlier, consideration of chip formation in the grain scale enables temperature analyses to be more accurate and detailed.

As a final step, an initial approach and experimental results are proposed in order to model and investigate dynamics of the grinding process. Simulations are in a good agreement with experimental results which means presented approach is promising. Motivation and objective behind this introduction is the lack of dynamic models related to abrasive machining in the literature. Non-linear nature of the process makes it a sophisticated problem. Although grinding chatter is often not visible to a human eye, it considerably decreases the performance of the final product.

2.3 Layout of the Thesis

The thesis is organized as follows:

In Chapter 2, methodology for identification of the abrasive wheel topography and abrasive grain properties are presented. Assumptions and formulations for simulation of wheel surface are given. Construction of distributions for rake angle, oblique angle, grit edge radius, height and width parameters by grit scanning are shown.

In Chapter 3, uncut chip thickness for each grain is calculated which is vital for surface roughness, force, thermal and vibration analyses. Positional and maximum chip thickness calculations are formulated and model for final workpiece surface profile prediction is presented and verified by experiments.

In Chapter 4, semi-analytical force model is presented and verified by several experiments. Methodology and steps for simulation procedure are clearly listed.

In Chapter 5, a thermo-mechanical model at primary shear zone with dual-zones (sticking and sliding) on the rake face of the abrasive grit is presented for regular (non-grooved) and circumferentially grooved abrasive wheels. The detailed formulation is also presented along with simulation procedure and results.

In Chapter 6, a temperature model that uses 2D moving heat source theory is developed. Experiment procedure for measuring temperatures from contact zone is given step by step and results are compared with simulations.

In Chapter 7, an initial approach is proposed in order to model and investigate dynamics of the grinding process. An analogy between grinding and milling processes is introduced in the sense of cutting grit or teeth number for stability analysis.

In Chapter 8, the suggestions for the further research and conclusions are presented.

3 Identification of Abrasive Wheel Topography and Grain Properties

The identification of abrasive wheel topography and simulate the necessary portion of the wheel surface is one of the basic aims of this thesis. The true representation of the wheel topography is essential for all presented models. Presented techniques and assumptions in Section 2 should be carefully applied in order to get accurate predictions from surface profile, force, temperature and vibration models. Kinematic analysis for uncut chip thickness calculation and determination of volume that lies in grit penetration depth to the workpiece are almost impossible without accurate topography analysis.

3.1 Wheel Surface and Grain Measurements

As mentioned earlier, the complexity of the grinding process comes from the abrasive wheel which contains various abrasive particles. Since these grits are randomly distributed on the wheel surface so there is significant variation of the process due to this randomness. Information regarding these random topographical and grit's geometrical parameters is not given by the wheel specifications. Total numbers of grits engaged in grinding, referred as active grit number " A_g " and uncut chip thickness for each of them can't be determined without this information. Even when total number of grits in the contact area between abrasive wheel and workpiece material is known, it should be investigated that whether they are active (ie. remove material by forming chips) or not by peak count analysis.

There are numerous methodologies reported to scan the wheel surface and grain properties [6]. In this study, a camera system with a special lens is utilized to measure the abrasive grain number per mm^2 , " C ", on the abrasive wheel. Then, a special areal confocal 3D measurement system (Figure 3.1) is used to determine the geometric properties of the grains such as rake and oblique angle, edge radius, width, height and their distribution.



Figure 3.1: Areal confocal 3D measurement system

100 nm sensitive dial indicator was used to align the abrasive wheel on X and Y axes of the measurement device. Measurements are done on both type of wheels (Alumina and SiC) presented. Four types of optical zoom lenses (5x, 10x, 20x and 50x) are used throughout the topography identification process for the wheels used in this study. 5x and 10x lenses are usually used to determine C parameter and distribution of the grains on wheel surface. Distance between neighbor grains and other distribution related parameters such as position and peak count analysis require wider range of scans both in X-Y plane and Z direction.

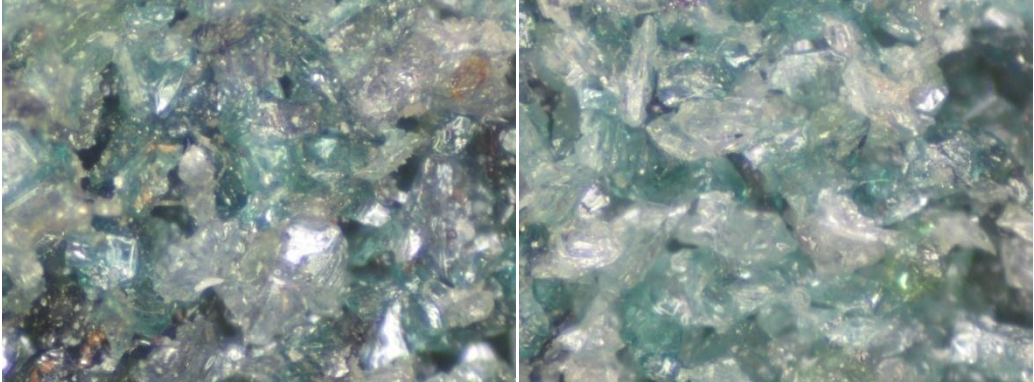


Figure 3.2: Surface of a SiC 80 M Wheel

In Figure 3.2, sample surface scan for a SiC 80 M wheel is presented. White particles are the abrasive grains that are responsible for cutting action and the green parts are the bond material that constructs the solid body structure of the wheel.

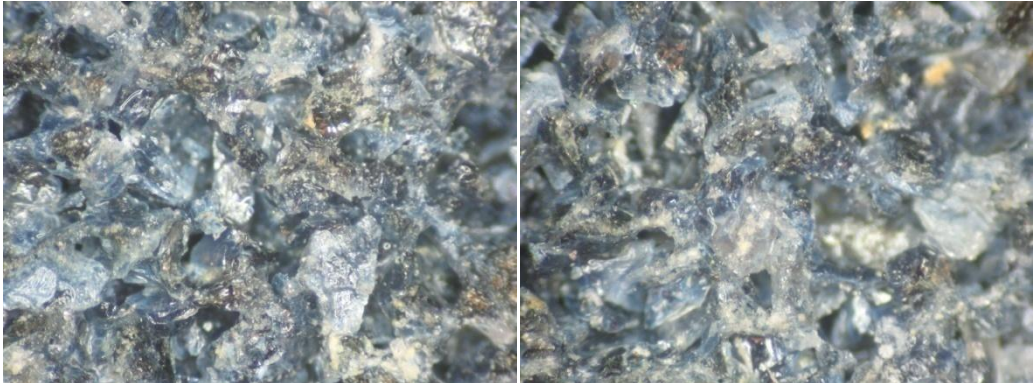


Figure 3.3: Surface of an Alumina 60 M Wheel

It is harder to determine abrasive grits for Alumina wheels compared to SiC wheel. Optical issues such as the reflection of measurement device's light from bond material are the main actors for that issue.

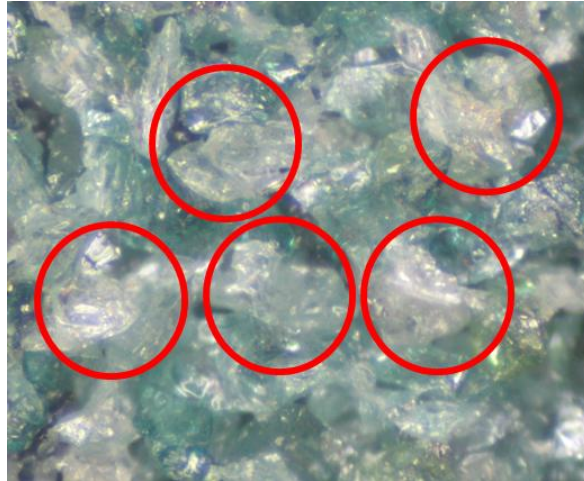


Figure 3.4: Abrasive grain per mm² “C” parameter identification for SiC Wheel

1x1 mm field of view is presented for a SiC wheel in Figure 3.4. As it can be seen, there are 5 peaks which are white abrasive grains and active, in other words, cutting edges. In Figure 3.5 another 1x1 field of view but for an Alumina wheel is presented. 6 active grains are detected for the Alumina 60 M. Reflections of the measurement device light is filtered through $\mu\text{surf}^{\text{®}}$ software and white abrasive grains are detected among the green colored bond material (for SiC wheel).

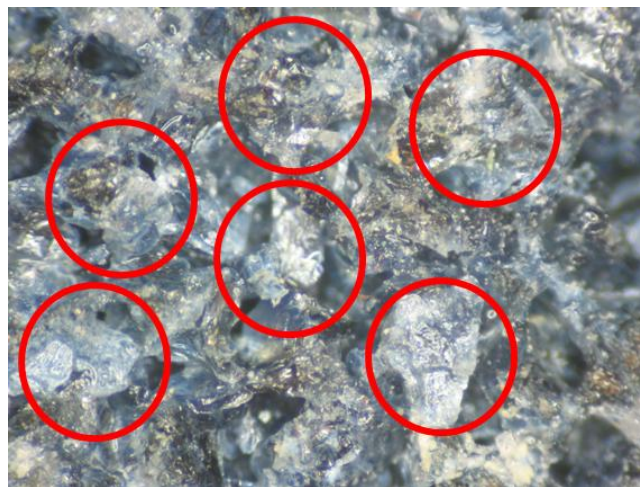


Figure 3.5: C parameter identification for Alumina Wheel

These peak edges are not selected by interpretation and manually. Peak count analysis is used to detect the highest points in the scanned area by the commercial software $\mu\text{surf}^{\text{®}}$ of the measurement system. Confocal microscopy which is an optical imaging technique used to increase optical resolution and contrast of a micrography by using point illumination and eliminates the out of focus light. It is used to detect the peaks as illustrated in Figure 3.6.

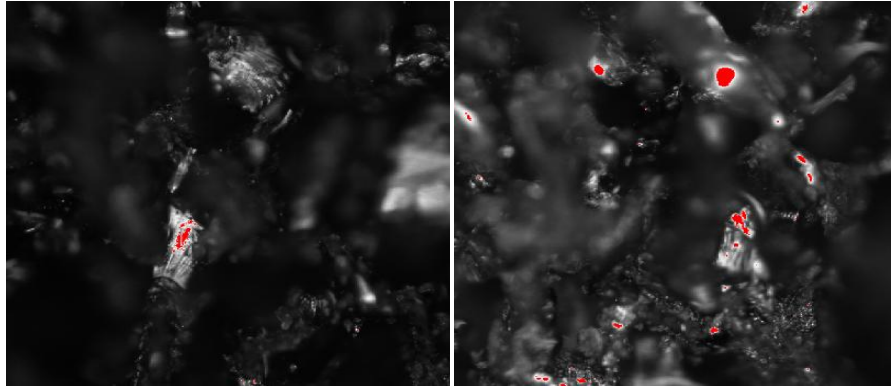


Figure 3.6: Abrasive grit identification by height analysis

Red sections observed in Figure 3.6 reflect more light indicating that these regions are higher than rest of the material around them. By zooming in and out, optimal position is found for a lens in Z direction and all the peaks are counted without consideration of the cut-off weight which determines whether these grits are active or not. C parameter identification should be performed by taking samples from many points. Considering the random distribution of the abrasive grains, observation of a single $1 \times 1 \text{ mm}^2$ will not be enough to determine the C. In this study, fifteen $1 \times 1 \text{ mm}^2$ regions are scanned for each abrasive wheel and a unique C is identified for each of them [69]. Although C does not vary in a large range for the different regions of the same wheel, an average of these fifteen values is taken for more accurate analysis. After that step, whole surface map is extracted as X, Y and Z coordinates and stored in arrays. A peak count method is applied and a sample result is shown in Figure 3.7. It should be noted that performing the peak count is vital to determine active grains.

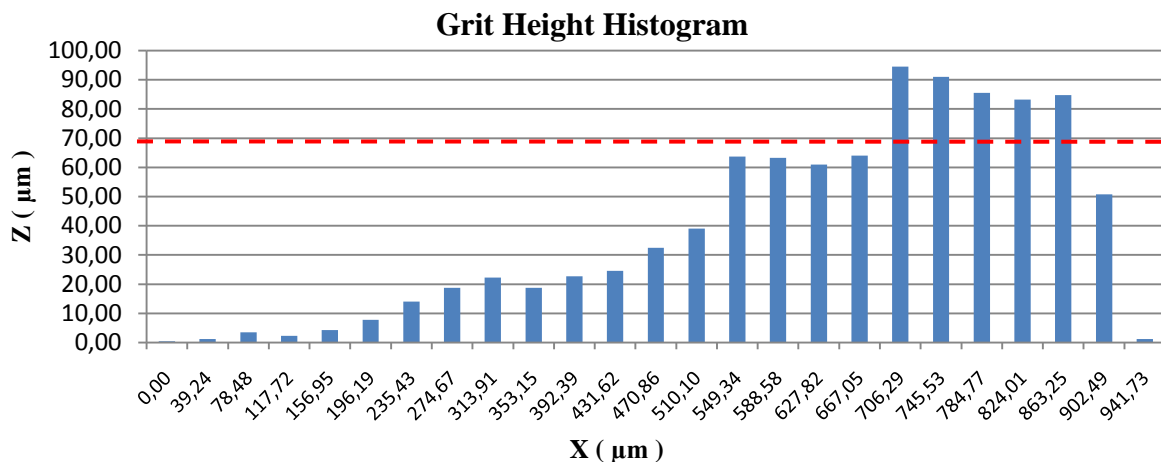


Figure 3.7: Peak count of abrasive grit heights (SiC 80 M wheel)

As Jiang et al. claimed there should be a cut-off height to determine these active grits [28]. Cut-off height is identified as $69 \mu\text{m}$ by volume density analysis on wheel surface for a SiC 80 M wheel (Figure 4.3). $\mu\text{surf}^{\text{®}}$ software has a special volume density analysis module which scans the whole surface and by evaluating the Z coordinates and determine a threshold

according to the selected filter type and parameters [28, 69]. In Figure 3.7, it can be seen that there are 5 grits in 0.94 mm^2 region which are higher than cut-off height, that value also agrees with the camera system measurement presented in Figure 3.4. Cut-off value that is identified by volume density analysis is also validated by the Jiang's active grit height method [28, 69]. The interaction between grain and workpiece material can be divided into three types as mentioned before; rubbing, ploughing and cutting. These phases are related with the grain penetration depth and diameter. Critical condition of ploughing and cutting can be checked from $h_{cuz} = \xi_{plow} d_{gx}$ and $h_{cuz} = \xi_{cut} d_{gx}$ where h_{cuz} is the grain penetration depth and d_{gx} is the maximum grain diameter [69]. ξ_{plow} and ξ_{cut} are identified as 0.015 and 0.025 for SiC wheels [69]. In this study, grains are not assumed as sphere; therefore d_{gx} is taken as the width of the abrasive grain. In Figure 3.8, dashed area represents the bond material and $h_{cuz,max}$ is the maximum penetration depth of a grain and $h_{cu,max}$ is the maximum penetration depth from all over the grains. By using the Equation 1, cut-off distance can be identified to determine number of active abrasive grains per 1 mm^2 [28,69].

$$h_{cuz,max} = h_{cu,max} - (d_{max} - y) \quad (1)$$

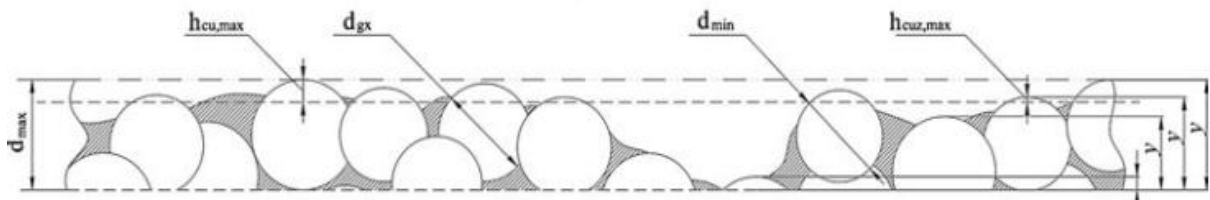


Figure 3.8: The grain distribution within the abrasive wheel [28]

Other grits below the cut-off value are assumed to be inactive in the sense of chip formation during the operation. For the Alumina 60 M wheel, cut-off height is identified as $52 \mu\text{m}$ and peak count histogram is presented in Figure 3.9.

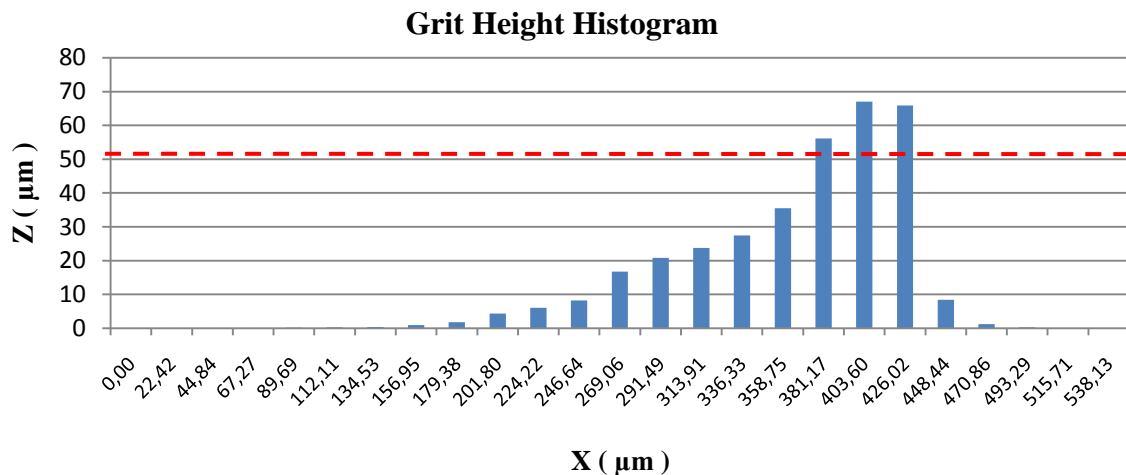


Figure 3.9: Peak count of abrasive grit heights (Alumina 60 M wheel)

Next step after identification of the C parameter is the determination of grit's geometrical properties. 20x and 50x lenses are utilized for this purpose. Abrasive wheels that are often used in the industry have abrasive grits on them with 40 to 150 μm height and 20-200 μm width in general. Specifications on the wheel include general information regarding to the wheel structure such as coarse or fine grit size, dense or sparse distribution. There is no data about geometrical structure and shape of abrasive grains considering the fact that they strongly depend on the dressing conditions. In this study, it is assumed that abrasive grits will always have the same or similar average properties with same dressing procedure as agreed in the literature [28]. Without this assumption, constructing an analytical model in the abrasive grit scale can be an almost impossible task.



Figure 3.10: 50x lens that is used for grit scans

White and shiny abrasive grains on the SiC 80 M wheel are scanned by 50x lens shown in Figure 3.10. Four grains that are scanned are illustrated in Figure 3.11.

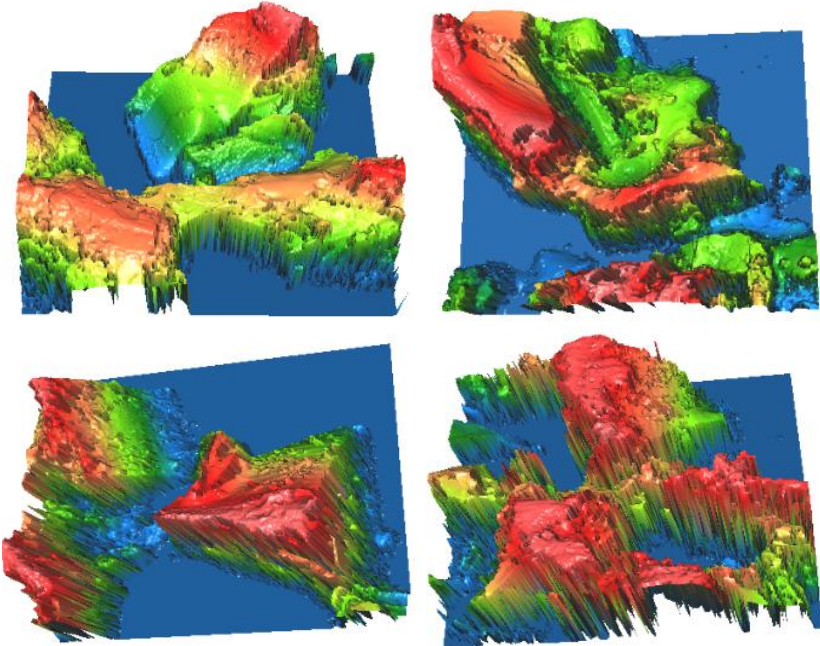


Figure 3.11: Samples for scanned grains

Number of grains that should be scanned to construct the distributions of these parameters is also an important number to decide. Mean and standard deviation of the measured values are needed to construct the corresponding Gaussian distribution. One can obtain these values by scanning ten or thousands grains; however, accuracy of the wheel topography identification increases with the number of grains that are scanned.

Average abrasive grit height and width for SiC 80 M wheel are 64 μm and 52 μm , respectively. Standard deviation for height is 11 μm and for width 8 μm . Geometrical parameters for this wheel which are obtained by hundred abrasive grain scans can be seen in Table 3.1.

Abrasive grit	Mean	Standard Deviation
Height	64 μm	11 μm
Width	52 μm	8 μm
Rake Angle	-17°	4.58°
Oblique Angle	18.55°	7.12°
Edge Radius	0.5 μm	0.2 μm

Table 3.1: Geometrical properties of abrasive grits for SiC 80 M wheel

Sample distribution for rake and oblique angles for SiC 80 M wheel is given in Figure 3.12.

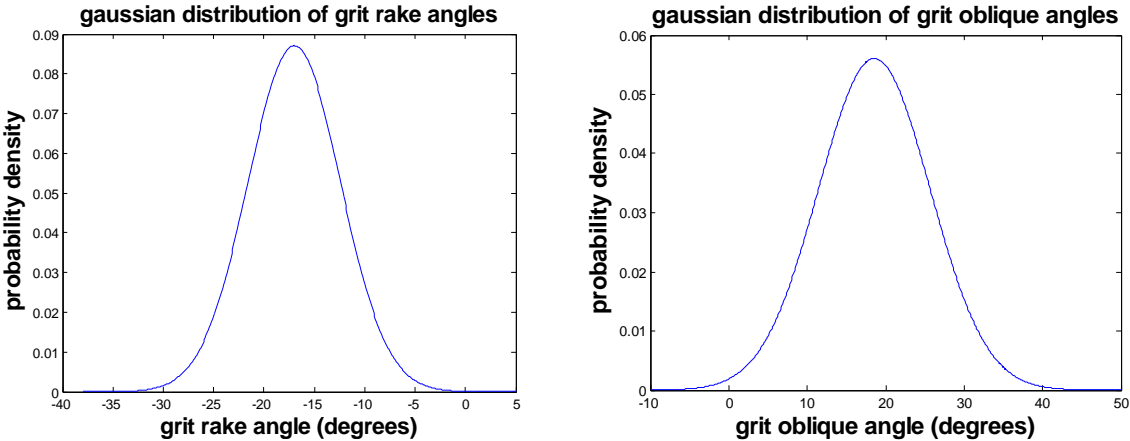


Figure 3.12: Rake and oblique angle distribution for SiC 80 M wheel

Parameters identified for Alumina 60 M wheel by the same procedure is given in Table 3.2.

Abrasive grit	Mean	Standard Deviation
Height	53 μm	16 μm
Width	41 μm	11 μm

Rake Angle	-11°	6.22°
Oblique Angle	23.7°	9.33°
Edge Radius	0.7 μm	0.15 μm

Table 3.2: Geometrical properties of abrasive grits for Alumina 60 M wheel

After obtaining C parameter and geometric parameters of the abrasive grains, it is possible to simulate the abrasive wheel surface as described in next section.

3.2 Simulation of Abrasive Wheel Topography

Abrasive wheel topographies for regular and circumferentially grooved wheels are simulated via MATLAB[®]. Same simulation procedure is followed for both SiC and Alumina wheels.

$$\Delta = 137.9 \times M^{-1.4} \sqrt{\frac{\pi}{32 - S}} \quad (2)$$

Δ value is the average distance between abrasive grits, M is the grit number and S is the structure number in Equation 2 which are required for simulation of the wheel topography, however; the equation does not consider whether these grits are active or not [5]. Peak count method that was described in previous section solves this issue (Figure 3.7). However, when simulating the wheel surface, non-active grits are also included to represent the real wheel better.

Another important parameter is C, which was identified as a first step. It is introduced as a constraint to a wheel simulation code, there can't be more than C number of active grains in a 1 mm² area. There should be a minimum distance between active grits in order to avoid intersection analysis for two very close abrasive grains in the sense of uncut chip thickness calculation, since it is rarely observed (4 grains out of 100 for this analysis), these types of intersections are ignored in the scope of this study. Area that is occupied by a single abrasive grit is represented by Equation 3 [5].

$$g_d = 15.2M^{-1}$$

(3)

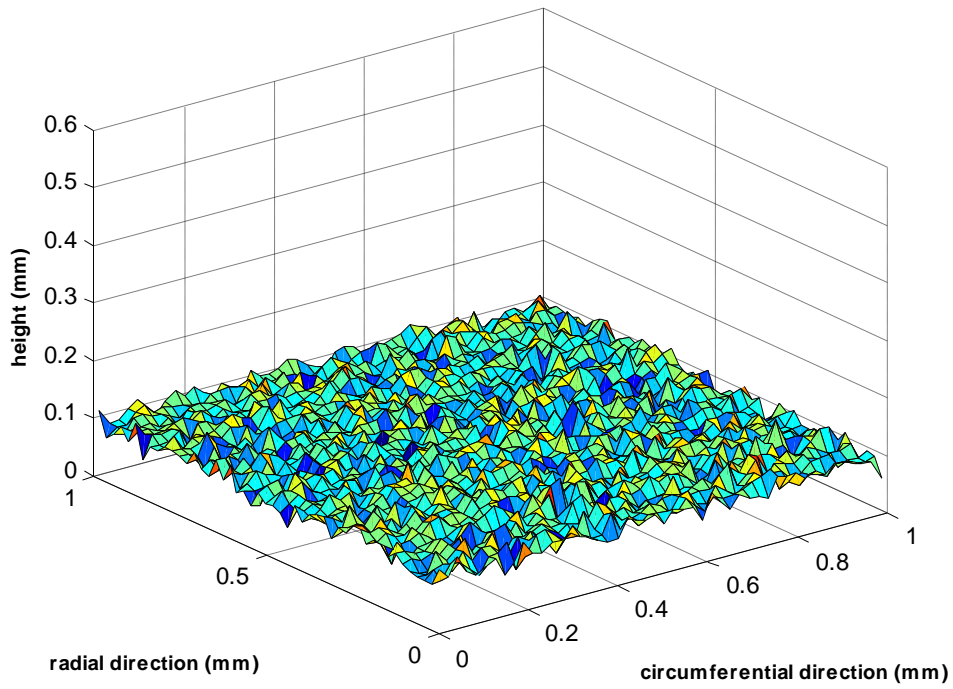


Figure 3.13: Abrasive wheel topography (SiC 80 M wheel)

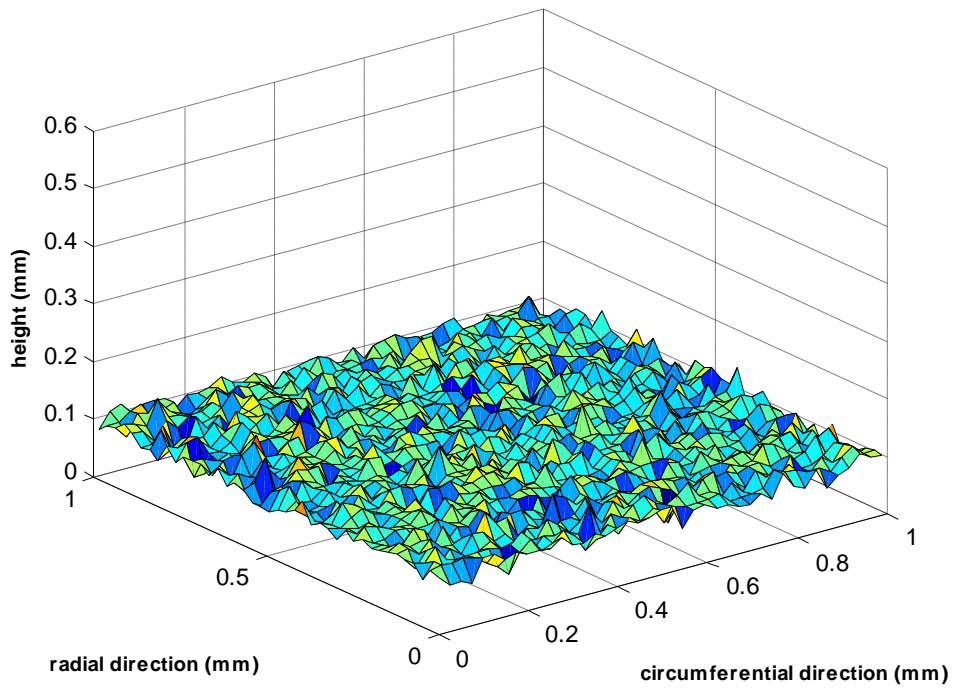


Figure 3.14: Abrasive wheel topography (Alumina 60 M wheel)

Topographies that are presented in Figure 3.13 and Figure 3.14 are for flat surfaces, in other words regular wheels. Difference between these two topographies may not be straightforward; however, one can notice the wider distance between neighbor grits for Alumina case since it has 60 M structure compared to 80 M SiC wheel. In addition, geometrical parameters that are presented in Table 3.1 and Table 3.2 are in grain scale and not noticeable in wheel topography figures.

In order to simulate a single grain, 8 values are selected from the constructed Gaussian distributions which are, rake angle, oblique angle, edge radius, width, height and X, Y, Z coordinates. These parameters are randomly selected from the distributions and same procedure is repeated for each abrasive grain. For example, if there is a 50.000 abrasive grains on a wheel, same procedure should be repeated 50.000 times since each abrasive grain requires 8 parameters which are given above. Therefore, random nature of the abrasive wheel topography can be represented in the simulated surface as well.

Material between peaks and valleys is the bond material and its contribution to the process is ignored in the presented models throughout this study. It requires extensive material science and chemistry knowledge since it is believed that when process temperature reaches up to thousand Celcius degrees, diffusion between bond material and other bodies occur.

In order to predict surface roughness, force and temperatures for grooved wheels, abrasive grains on the groove walls should be considered as well. Dressing conditions for regular and grooved wheels are given in Section 3, Table 4.2. Dresser tool and dressing operation parameters (feed and depth) are crucial for groove geometries. Dresser tool is scanned in order to determine groove ground radius and width. Detailed information about the dressing operation and groove formation can be found in Section 4.

Abrasive wheel topography can be simulated as a whole, however; simulating a small portion of a flat surface or one groove is time efficient and enough to perform roughness and further analysis since it is assumed that entire surface share the same topographical characteristics. Simulation of the whole wheel would require serious amount of time and computational effort considering there can be up to thousands of grits on a single wheel.

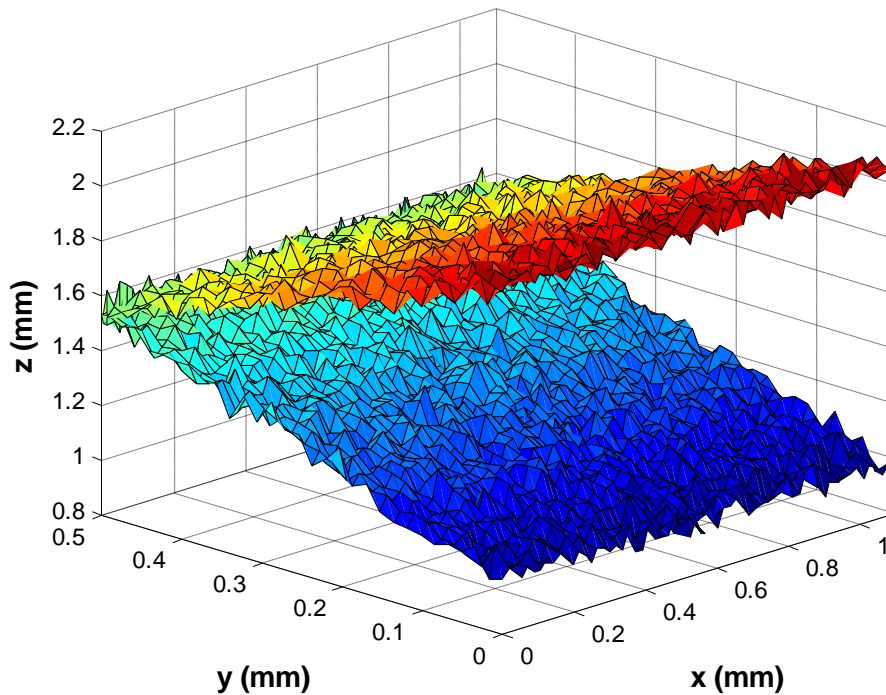


Figure 3.15: Single groove topography (SiC 80 tool)

Abrasive grits on groove walls should be carefully investigated since the surface is not flat and angles (rake and oblique) vary due to the position of the grit. C parameter is assumed to be same with regular sections and active grit number is determined via same peak count method. There are experimental studies related to surface roughness and force analysis for grooved wheels; however, modeling the process enable us to determine optimum groove geometry and depth on the wheel.

It should be noted that each grain has its own rake, oblique angle, edge radius, height and width that are randomly assigned from obtained Gaussian distributions. Grit edge radius can be considered as the hone radius in turning and milling cutter tools. Other parameters are well known angles and dimensional values which are required for modeling the chip formation mechanism. As mentioned earlier, micro milling analogy for abrasive machining is used throughout the Section 4, 5 and 6. Therefore, simulation of the wheel surface and storing all active grains' geometrical data in an array are crucial tasks for this study.

3.3 Abrasive Grain Analysis

Alignment of the wheel on measurement device table is crucial for correct identification of grains' geometrical parameters. Once the alignment is done properly, rake angle, oblique angle, edge radius, height and width of each grain can be determined by μ surf software.

Cutting speed and feed directions should be carefully checked for rake and oblique angle identification step. Reliability of this technique is ensured by a 100 nm sensitive dial indicator that is used to align the wheel, therefore the abrasive grains. Non-uniform grains and intersected neighbors are neglected in this study. Identified geometrical properties should be considered as “average values per grain” which are believed to represent the stochastic nature of the abrasive wheel and grains.

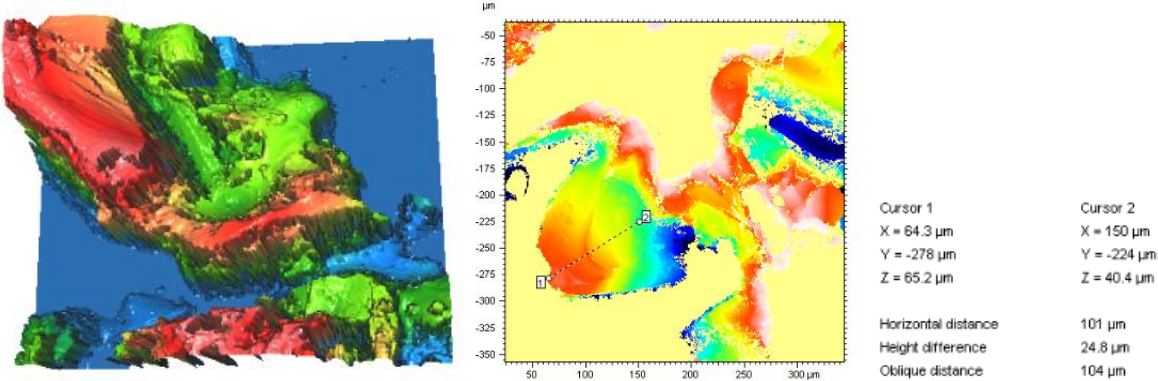


Figure 3.16: Sample rake angle identification

By moving cursors in the correct locations and checking their X, Y and Z coordinates, any geometrical property of the abrasive grain can be measured. If two cursors are not enough, it can be switched up to five cursors, it is required especially for determination of the region that a single grain occupies. Oblique angle can be determined by placing two cursors to both edges of the grit tip. Height is taken from blue sections to the grit tip and width is measured both in X and Y directions. Region that a grain occupies is determined by four or five cursor points by placing them around the abrasive grain visually.

Results are in a good agreement with Equation 3. It can directly be calculated from the equation, however, it is not possible to determine rake, oblique angles and edge radius from the equation. An equation can be derived by curve fit or by calibration of some constants; however, it requires both identification of tens of wheels made by same bond and abrasive material and variation due to dressing conditions. In order to construct an analytical model for determination of the abrasive wheel topography, modeling of the dressing operation is required by considering material properties of both dresser tool and wheel, fracture mechanics of the abrasive grains and behavior of the bond material.

4 Surface Roughness and Uncut Chip Thickness Calculation

In this section, uncut chip thickness for each grain is calculated, positional and maximum chip thicknesses are formulated. Model for final workpiece surface profile prediction is presented and verified by experiments.

Due to stochastic nature of the abrasive tool and in-process vibrations, complete prediction of the final workpiece surface topography is a sophisticated problem. Consequently, the assumptions presented by Warnecke and Zitt [29] are used in this work as well. They are;

- Grinding wheel vibration is neglected.
- The material of the workpiece in contact with the abrasive grits is cut off when the wheel is fed into the workpiece.
- No slide flow, built-up-edge or ploughing phenomena.

4.1 Calculation of Uncut Chip Thickness per Grain

In general, a single average uncut chip thickness is calculated and used for whole active grains [1,2,3,4]. However, each grain has a unique uncut chip thickness due to their different geometrical properties. Being able to calculate uncut chip thickness per each grain enables more accurate predictions for the presented models. Simulated wheel has a wavy surface which is similar to the real wheel topography and all grains should be evaluated individually. Contribution from bond material is neglected since they do not form chips and mostly responsible from friction between wheel and workpiece material.

Calculation of a single abrasive grit's trajectory by equation 4 is possible. In order to simulate final workpiece surface topography, consideration of adjacent grits located in radial and circumferential direction is also required. Average distance between abrasive grits is calculated as 20 μm from equation 2 and 173 μm for active grits from surface topography measurements in Section 3 for a SiC 80 M wheel.

$$\begin{aligned}x &= feed_r \times t + (R + height_{grit}) \times \sin(\theta) \\z &= (R + height_{grit}) \times (1 - \cos(\theta))\end{aligned}\tag{4}$$

Parameters are feed rate per grit ($feed_r$), time (t), radius of the wheel (R), height of the grit ($height_{grit}$), and position (engagement) angle of it (θ). Feed per revolution for grit is calculated by considering the active grit number that lies in contact zone between wheel and workpiece.

It should be noted that feed per revolution for a grain is usually in a few microns scale, therefore correct identification of active grit number is vital.

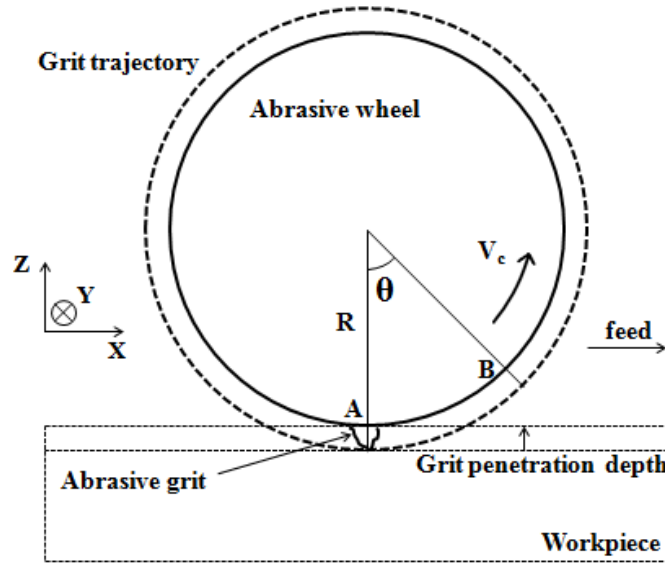


Figure 4.1: Trajectory and penetration depth of a single grit

In Figure 4.1, single abrasive grit's trajectory can be seen. Origin of the wheel is fixed in Z and Y direction during the operation. Rotational movement of the wheel around Y axis combined with translation (feed) in X axis constructs the trochoidal movement of the wheel. Abrasive wheel both rotates and moves along workpiece surface. Rotation introduces us the cutting action and cutting speed can be calculated from well-known $V_c = \pi * D * n$ formula. D is the diameter of the wheel and n is the revolution per minute (rpm). Feed rate is generally defined as millimeter per minute when generating the tool path but it should be converted to millimeter per revolution for each grit, also can be referred to as uncut chip thickness per grit.

Start and exit angles for a grain can be calculated by classical formulation derived for milling operations. They are different for up and down grinding modes. In down grinding, the direction of rotation of the grinding wheel at the point where it contacts the workpiece is identical to the feed direction of the machine table. If the wheel is counter-rotating to the feed movement then the process is referred to as up-cut grinding.

$$\theta_{engagement} = \cos^{-1}\left(1 - \frac{a_{grit}}{R}\right) \quad (5)$$

Angle that is introduced in Equation 5 represents the exit and start angles for up and down grinding respectively. In up grinding, grit starts with a zero chip thickness and reaches to the maximum; whereas in down grinding, grit meets with maximum chip thickness at the very

beginning of its interaction with the workpiece and then goes to zero chip thickness. Hence, start and exit angles are zero for up and down grinding respectively. Behavior of the forces change due to up and down grinding strategies but maximum force, power and torques do not.

The paths of the cutting edges can be assumed as circular arcs which mean workpiece remains stationary during an individual cut of grit. Afterwards, it moves instantaneously by the distance between adjacent sets. Uncut chip thickness per grit is usually calculated by using this assumption in the literature [16].

$$h = 2 \times dset_i \times \left(\frac{feed}{V_c}\right) \times \left(\frac{a_{grit}}{D}\right)^{0.5} \quad (6)$$

$dset_i$ is the set number of an abrasive grain cluster and explained in Section 3.2. Neglecting the trochoidal movement will lead to wrong calculation of uncut chip thickness per grain.

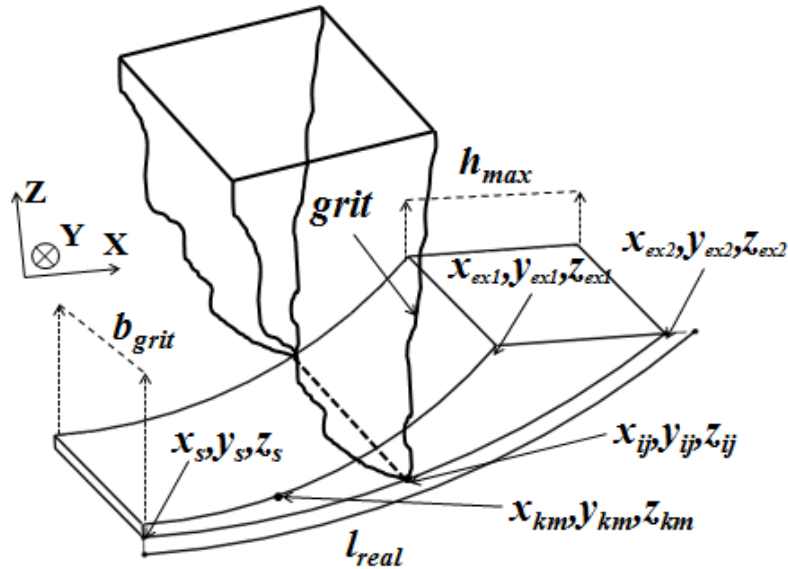


Figure 4.2: Grit trajectory and chip thickness variation due to the trochoidal movement

Equation 6 uses a simplification by ignoring the trochoidal movement of the grits. It can be neglected for the high $feed_r/D$ ratio cases [67] which are also valid for grinding operations; however, for more accurate analysis, trochoidal movement is also considered. Uncut chip thickness differs for each abrasive grain since its geometric properties are assigned from normal distribution of measured parameters in Section 3. Geometric properties of the grits are stored in an array; uncut chip thickness and grit penetration depth calculation are done accordingly. Maximum and instant uncut chip thickness can be calculated via Equation 7 without neglecting the trochoidal movement.

$$\begin{aligned}
h_{\max} &= \sqrt{(x_{ex1} - x_{ex2})^2 + (y_{ex1} - y_{ex2})^2 + (z_{ex1} - z_{ex2})^2} \\
h_{\theta} &= \sqrt{(x_{km} - x_{ij})^2 + (y_{km} - y_{ij})^2 + (z_{km} - z_{ij})^2}
\end{aligned} \tag{7}$$

Coordinate values of exit 1 and 2 points are illustrated in Figure 4.2 and obtained through kinematic trajectories and real contact length identification. It was shown in the literature that the real contact length between abrasive wheel and workpiece is substantially larger than the geometric contact length [2,10,30]. The increased area of contact is mainly due to deflection of the wheel and grits under the action of the normal force [30]. Therefore, active grit number is obtained more accurately which improves both surface roughness and force predictions.

Geometric contact length is easy to derive as $l_c = \sqrt{a * D}$ in where a is the axial depth of cut and D is the diameter of the wheel. Using the geometric contact length is a great simplification since it neglects all the effects mentioned in the previous paragraph. Real contact length between abrasive wheel and work material is identified via temperature measurements and explained in Section 7. It is required for detailed and more realistic analysis. It also changes the maximum chip thickness since the exit and start angles change for up and down grinding, respectively. Volume that a single grain removes from the workpiece changes (usually increases), which will affect forces directly.

Kinematic analysis is fast, detailed information about chip thickness per each grain can be obtained and it gives more insight about the process mechanics. Same procedure is repeated for each active grain and uncut chip thickness values are stored in an array ready to serve for models explained in further sections.

4.2 Workpiece Surface Roughness Model

In this study, surface profile (peaks and inverted valleys) for a specified sample length is simulated and arithmetic average value of the departure from profile from the center line (R_a) is obtained. There are studies in the literature that try to obtain R_a value directly by derived equations [1,2,3,4]. Since the wheel topography varies with dressing conditions, R_a values that are calculated directly from wheel specifications and process parameters are often not well agreed with experiment results.

Abrasive grains on the same radial line (in perpendicular to the circumferential direction) over the wheel are considered as a “set” and an ID number is assigned to each set. Each set has a

circumferential distance in-between ($dset_i$) which was assigned by normal distribution of measured grit distances.

$$\begin{aligned} x(\text{setID}\#) &= feed_r \times t + (R + height_{grit}) \times \sin(\theta) \\ y(\text{setID}\#) &= (R + height_{grit}) \times (1 - \cos(\theta - (\text{setID}\# - 1) \times \theta_{delay})) \end{aligned} \quad (8)$$

Constructing sets and defining clusters of abrasive grains is beneficial for the surface roughness simulation. Rather than just obtaining a single parameter defining the roughness of the final workpiece surface, entire profile is simulated in this study. It is especially required for surface analysis when using grooved wheels.

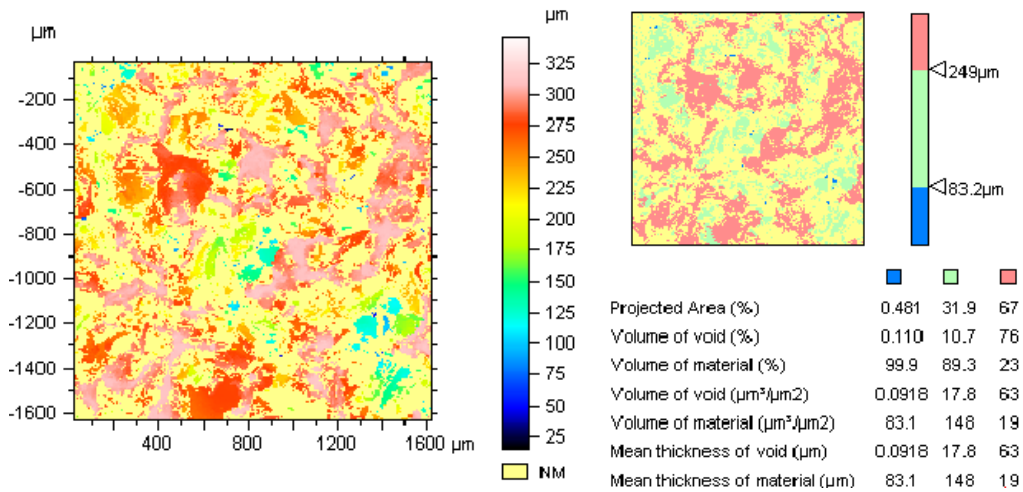


Figure 4.3: Wheel topography for surface roughness analysis

Sets are identified via surface analysis on abrasive wheel as presented in Figure 4.3. Projected area and volume of void can be obtained in the measurement software and a set ID is assigned to the grain clusters that are on the same radial line by $\pm 10 \mu\text{m}$ tolerance. Decreasing the tolerance value will increase the simulation time since there will be more sets to be evaluated. Usage of the sets enables simulation to handle neighbor grains in one loop which shortens the run time seriously.

Angle increment is set to 0.001 degrees and the positional change in both X and Z direction for the time of wheel to travel those 0.001 degrees is calculated. Angle delay between adjacent sets is calculated and the set that follows current one is evaluated in the same loop but as a next step. Number of sets that should be considered is determined by the desired surface profile's length. Since 1,6 mm of a final workpiece surface profile is simulated throughout this study which is enough to obtain the R_a value; typically 1500-2500 sets are evaluated. It also changes with the feed rate and the rotational speed of the abrasive wheel.

Surface roughness in perpendicular to feed direction is considered since it enables us to observe grit scratches and groove prints on the surface. Roughness in feed direction is much smaller due to lack of grit scratches and prints. One may move along a single grit's scratch on the surface and miss the general profile if the roughness in feed direction is measured. However, measurement in the perpendicular to feed direction covers all the groove prints for grooved wheels and scratches for both wheel types.

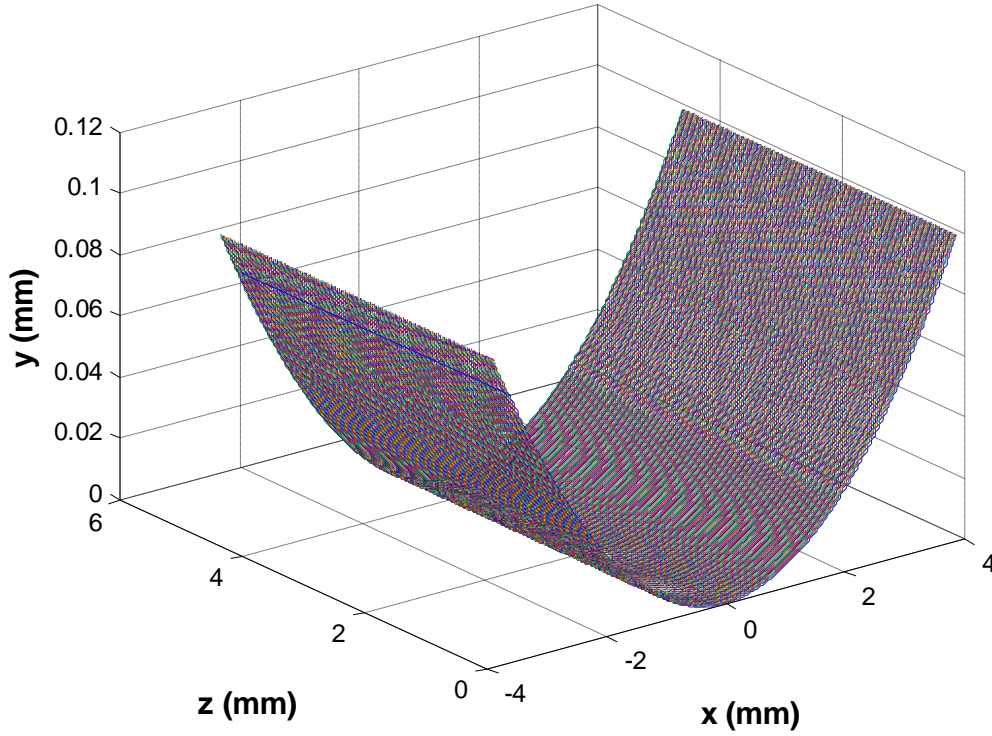


Figure 4.4: Abrasive grain trajectories (2 sets included)

Volume of the material removed from the workpiece by a single grit is calculated by kinematic analysis as well. Surface area of the chip in X-Z plane is calculated and multiplied by b_{grit} to obtain total volume of the chip that is formed by the grit. Trajectory of grit tip is represented by i and j indexes where the intersection of the upper side of chip with grit section is represented by k and m (see Figure 4.2). Some studies multiply the maximum chip thickness, width of the grain and the height of the grit penetration depth and obtain the chip volume. Calculation time can be considerably reduced with that assumption; however accuracy of the predicted values will decrease as well. Volume of the chip that is removed from the workpiece can be calculated as follows:

$$Vol_{chip-grit} = \left(\int_{x_{st}}^{x_{ex}} f(x_{km}, z_{km}) - f(x_{ij}, z_{ij}) \right) \times b_{grit} \quad (9)$$

$$f(x_{km}, z_{km}) = ((feed_r \times t + (R + height_{grit} - a_{grit}) \times \sin(\theta), (R + height_{grit} - a_{grit}) \times (1 - \cos(\theta))) \quad (10)$$

$$f(x_{ij}, z_{ij}) = (feed_r \times t + (R + height_{grit}) \times \sin(\theta), (R + height_{grit}) \times (1 - \cos(\theta))) \quad (11)$$

Equation 9, 10 and 11 are repeated for all active grains in contact region and not applied to the non-active ones that are below the cut-off height. When the volumes of all chips are subtracted from the workpiece by considering their coordinates, final workpiece surface profile can be obtained. A flowchart for a surface roughness model and simulation is presented in Table 4.1.

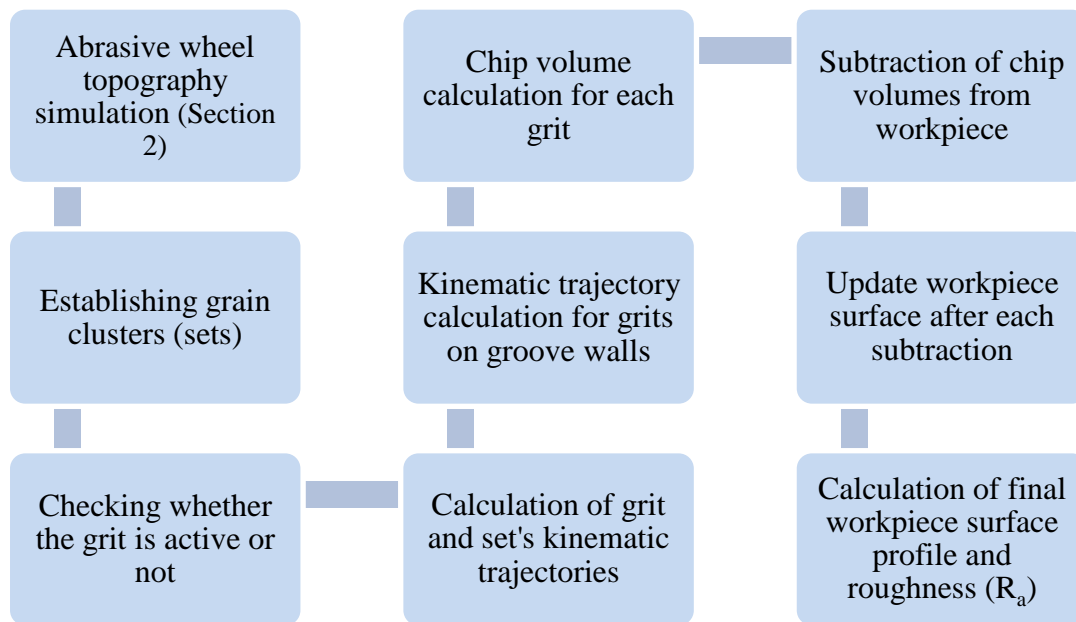


Table 4.1: Flowchart for a surface roughness model

4.3 Measured and Predicted Surface Profile and Roughness

The proposed model is applied to simulate the final surface profile of the workpiece and the results are compared with the experimental data. Experiments have been conducted with different process parameters on a milling machine tool in order to validate the presented model. AISI 1050 steel and 150*25*20 SiC 80 M grinding wheel are used as workpiece and cutting tool respectively. Single point diamond dresser with 2 carat grade is used for dressing the regular and circumferentially grooved wheels. Four different axial depth of cuts at 0.03, 0.05, 0.1 and 0.15 mm and four feed values at 0.075, 0.11, 0.15 and 0.18 mm per revolution with 5 different cutting velocities have been used in the experiments. Finally, surface roughness and texture of the final workpiece are measured using special areal confocal 3D measurement system. Same experimental setup is used to measure process forces as well; however they are presented in Section 4 and 5.



Figure 4.5: (a) Experimental setup (b) Dressing operation

Experimental setup can be seen in Figure 4.5. Dressing conditions for regular and circumferentially grooved wheels are presented in Table 4.2.

Wheel Type / Conditions	Feed (mm/rev)	Depth (mm)	Groove Width (mm)	Helix Angle
Regular (A)	0.04	0.05	NA	NA
Groove 1 (B)	2	0.1	1.1	0.24
Groove 2 (C)	4	0.1	1.1	0.6
Groove 3 (D)	5	0.1	1.1	0.72

Table 4.2: Dressing conditions

Grooved wheels can improve grinding efficiency by lowering the energy required to displace a unit volume of material from the workpiece. Since grooves introduce a helix angle to the

abrasive wheel similar to milling cutter tool, it can be referred as transformation from orthogonal to oblique cutting which is more desirable in the sense of efficiency and lower forces [32,58] . They also cause an increase in workpiece surface roughness compared to a regular (non-grooved) wheel. Their performance on workpiece surface profile is investigated in this section. Force, energy and temperature analysis for grooved wheels can be found in further sections.

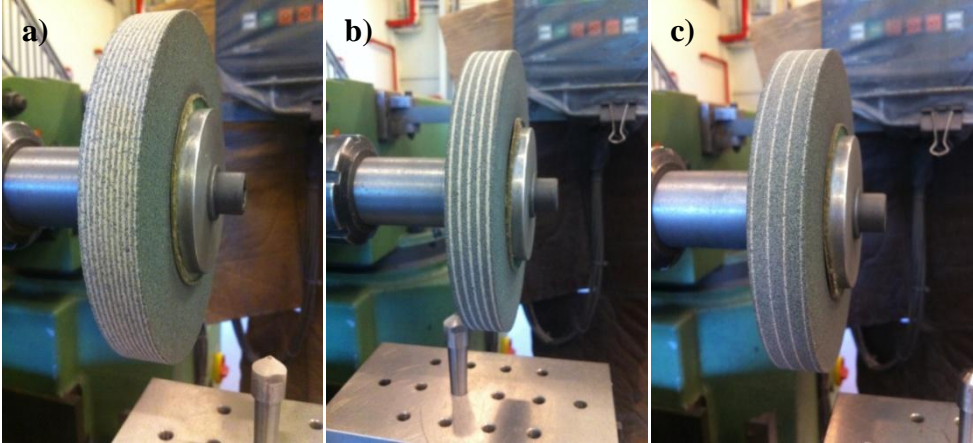


Figure 4.6: (a) Groove1-B (b) Groove2-C (d) Groove 3-D type wheels

Grooved wheels cause an increase in surface roughness compared to a regular wheel as expected. Groove marks on the workpiece surface can be observed by 3D confocal microscope which is the main actors for rougher surface results. Although surface finish is one of the most important reasons for using abrasive machining, as mentioned in the introduction, grinding and SAM operations can be used for difficult-to-cut materials such as nickel and titanium alloys. Grinding is considered a cost effective alternative for roughing operations as abrasive machining technology develops. Hence, grooved wheels can be used for roughing operations; lower forces and process energy are vital to prevent thermal damages on work material.

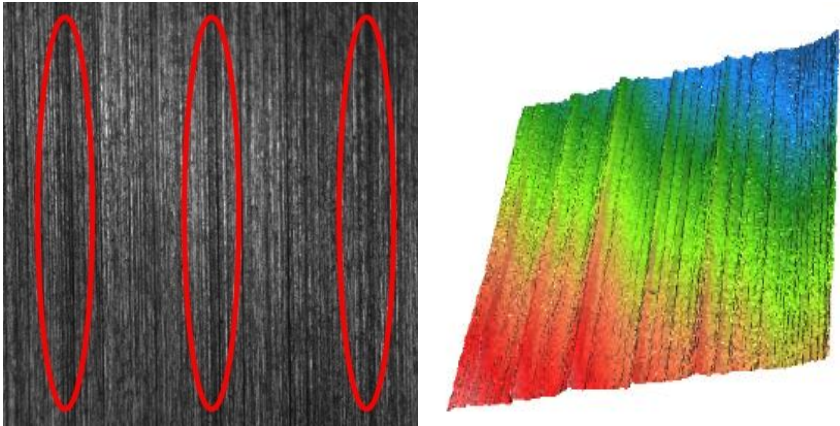


Figure 4.7: Groove marks on final workpiece surface for Wheel b (feed = 0.11 mm/rev & a = 0.1)

Simulated and scanned surface textures agree with 18-20% error. Surface profile (peaks and inverted valleys) for a specified sample length is simulated and arithmetic average value of the departure from the profile center line (R_a) is obtained. Simulation and experiments results are not presented for wheel C (groove 2) since values are considerably close to the regular wheel ($\pm 0.074 \mu\text{m}$ – average).

In general, all of the grains should be evaluated for a 1,6 mm workpiece surface which is around 60,000 for the SiC 80 M and 70,000 for Alumina 60 M wheel. Each of these grains' kinematic trajectories should be calculated by considering their trochoidal movement along the workpiece material. 60,000 trajectories with 0.001 degree angle increments require considerable amount of memory and computational effort. In addition, these trajectories should be updated as wheel moves along the workpiece since a single grain meets with workpiece hundreds of times in a 1,6 mm range.

A simulation code with a several nested loops and arrays that are dynamically updated per each revolution of the wheel is developed. It should be noted that grooves are evaluated separately and combined with the flat surfaces afterwards in order to reduce the nested loop number which increases the computational time seriously. Simulations are done as described in Table 4.1 by a 64-bit, Intel Core i7 CPU (3.40 GHz & 32 GB ram) PC.

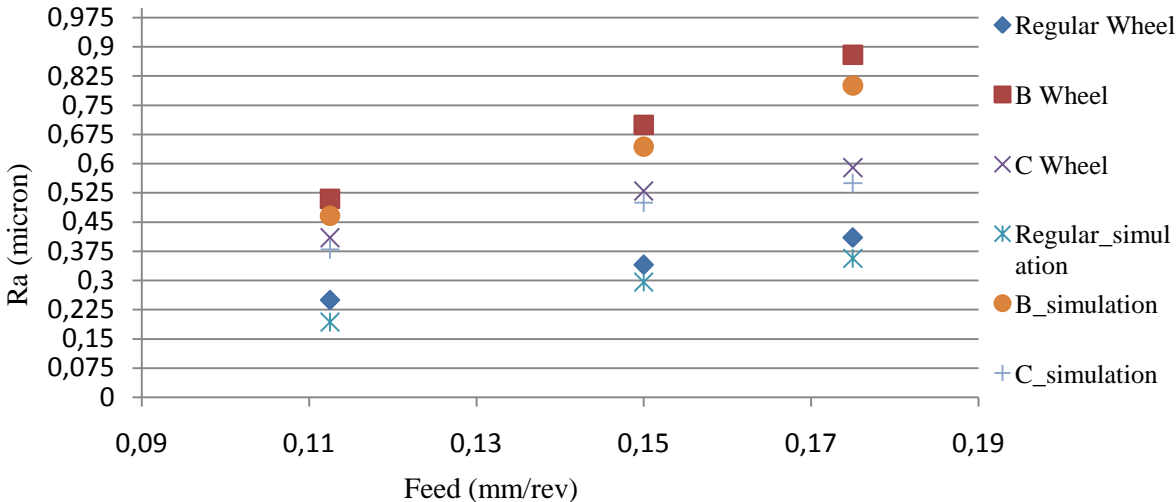


Figure 4.8: Ra for abrasive wheel types (a = 0.1 mm)

Surface roughness increases with the groove number on the wheel. Hence it can be said that there is a trade-off between lower process forces (lower energy) and surface quality. Both of them can be predicted by presented model and optimum wheel type, groove geometry and process parameters can be determined for a desired outcome by utilizing an adequate

optimization algorithm. In this study, roughness values are quite high for a regular grinding operation and reason for that is the usage of SiC 80 M which has a medium-fine grit size. By using fine or very fine grit sizes, surface roughness can be decreased but material removal rate should be lower.

In industry and practical applications, R_a value can be the sole criteria. In technical drawings, surface quality tolerance is usually stated by R_a . One can miss crucial information regarding the surface of the final product by only checking the R_a value. For example, surfaces created by Groove 3 (D) wheels are close to the ones obtained with regular wheels (A) in the sense of arithmetic average value of the departure from profile from the center line. However, since Groove 3 (D) wheel has grooves on it, these grooves will be printed on the final workpiece surface which will cause micro or nano channels on the surface. These printed grooves may cause problems for the final product even the R_a value of it meets the surface quality tolerance for the desired final product. Hence, prediction of the final workpiece surface quality is crucial for abrasive machining, especially for the wheels that is grooved or has unusual geometries.

In addition, there are studies in the literature that claims axial depth of cut directly affects the workpiece surface roughness. They also claim that feed rate and axial depth of cut's contribution to the final surface profile is very close to each other [1,4,22,30]. It has been noted that axial depth of cut is not a direct influence to the workpiece surface roughness as presented in Figure 4.9.

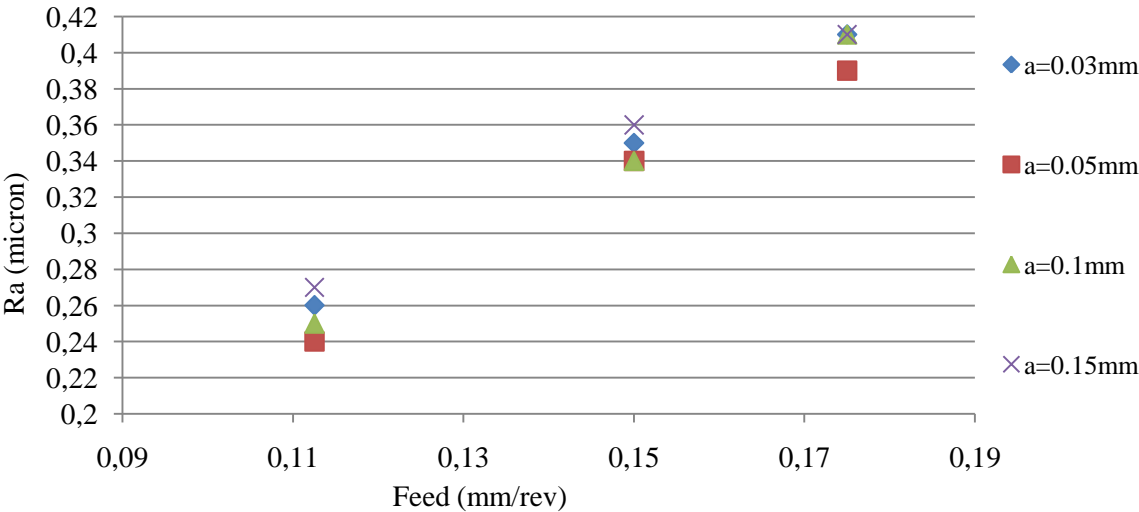


Figure 4.9: R_a values for regular wheel

Deflection of the tool and process vibrations should be the main actors for axial depth of cut's contribution which is hardly observed in the measurements. It is a fact that as axial depth of cut increases, stability limit can be exceeded (see Section 8). It means there will be a chatter vibration which directly causes an inferior surface finish.

Chatter vibration can be directly observed for milling and turning operations since the chatter sound and bad surface finish is obvious. However, for grinding operations, it is hard to hear the chatter sound and chatter marks on final workpiece surface is almost impossible to observe with human eye. It is believed that the studies in the literature which claims that axial depth of cut effects the surface roughness, exceeded the stability limit and the reason for the increase in R_a values due to axial depth of cut is the result of chatter vibrations.

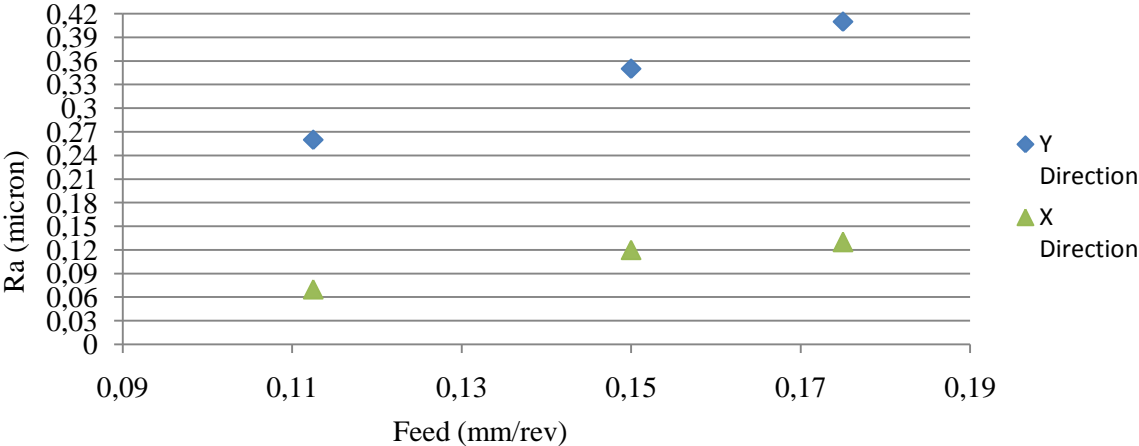


Figure 4.10: R_a values for X and Y direction – Regular Wheel ($a = 0.1$ mm)

In Figure 4.10, surface quality difference between X and Y direction is presented. Surface profile in X direction can also be predicted by dynamically updating the workpiece surface in feed direction which will double the computational effort and time. However, considering that the surface roughness in X direction is substantially smaller than the roughness in Y direction, it is not calculated in the simulation for reducing the run time.

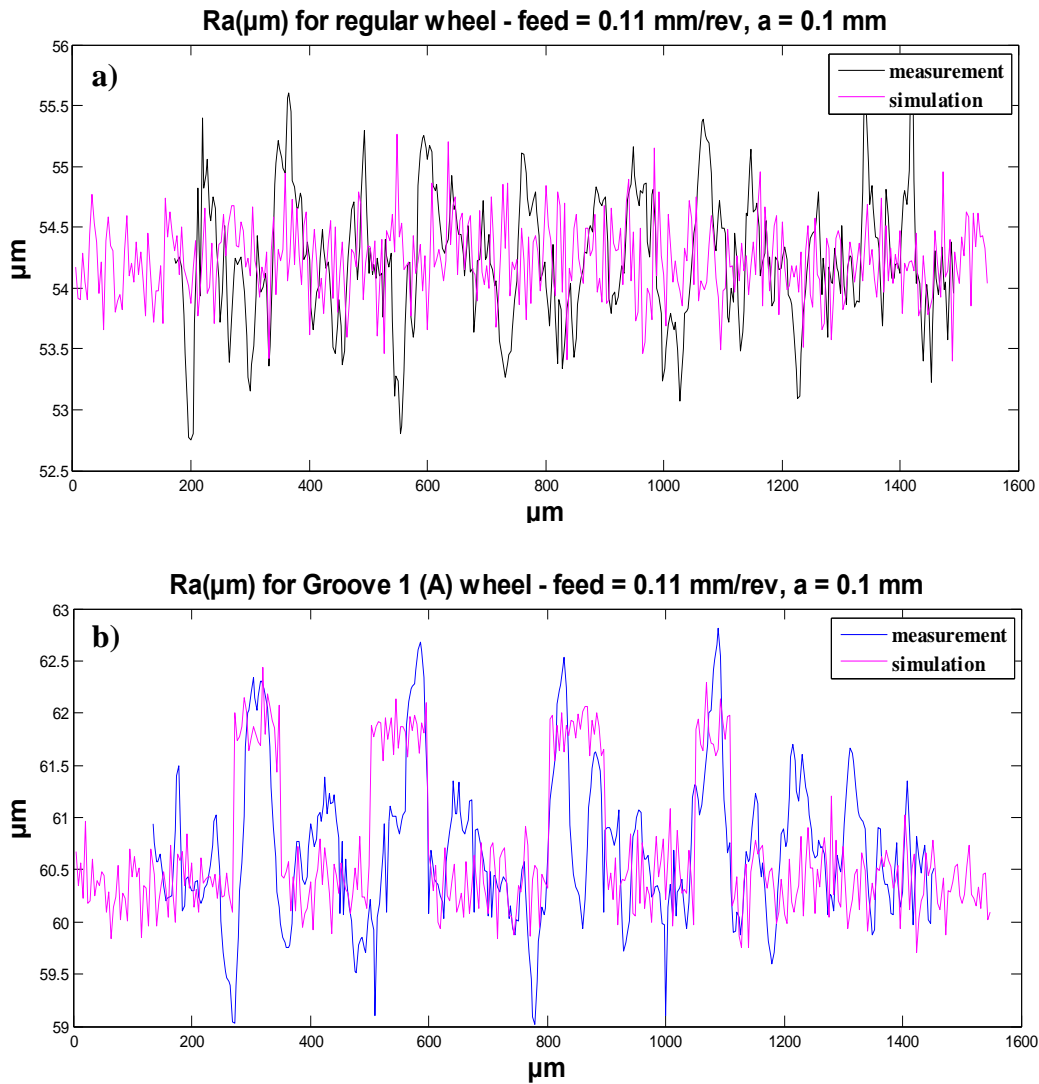


Figure 4.11: Measured and simulated surface profiles for regular and A type wheels

Measured and simulated surface profiles are illustrated in Figure 4.11. It is believed that the differences between measured and simulated surface profiles are due to the assumptions made in surface roughness model. Neglecting the grinding wheel vibration and ploughing phenomena should be the main actors for these discrepancies.

It should be noted that simulation gives lower roughness due to the reasons listed above. There are larger peaks in the measured surface profile in Figure 4.11 (a). Simulation result is smoother since the vibration and run-out of the wheel are neglected. For the grooved wheel, peaks due to grooves on the wheel can be predicted by the model as presented in Figure 4.11 (b). Groove topography is simulated (see Figure 3.15) and kinematic trajectories of the abrasive grains located on groove walls are calculated similar to the flat region analysis. Differences between measured and simulated profiles at the groove tips should be the result of the dresser tool wear since it is not included in the analysis. Groove tips become duller as

dresser tool moves along the abrasive wheel by opening the desired grooves. It can be observed that the first groove in the Figure 4.11 (b) agrees well with the simulated profile, however; as we move closer to the end of the profile, discrepancy between them increases. It is believed that although all grooves on the wheel share very close geometrical properties, there are slight differences among them due to run-out of the wheel and wear of the dresser tool as it moves along the wheel by removing abrasive particles and bond material to form the grooves.

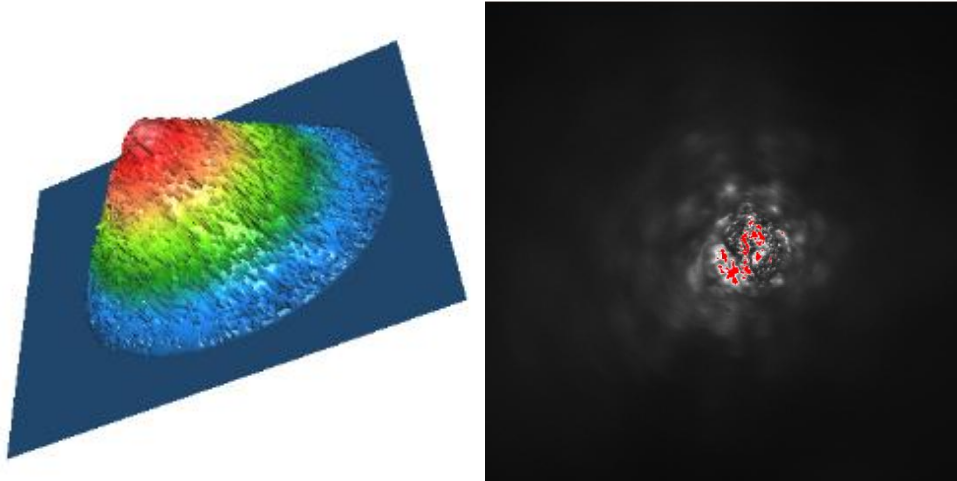


Figure 4.12: Scanned single point diamond dresser tip

Single point diamond dresser is also scanned and tip profile is obtained. It is crucial since dresser tip determines the groove geometry and profile on the grooved abrasive wheel. Dresser tool's tip radius is identified as $93\ \mu\text{m}$.

At each groove formation operation, brand new diamond dresser was used; however, as the dresser tool moves along the wheel surface, dresser tip becomes duller as mentioned earlier. Tip radius of the fresh dresser tools was measured after the formation of groove 1, 2 and 3 wheels and found as 152 , 134 and $116\ \mu\text{m}$ respectively. That means the groove ground radius increases towards the end.

5 Semi-Analytical Force Model

In this section, micro milling analogy for grinding operations is used. Once geometrical properties of grains are identified as presented in Section 3, force analyses are performed by assuming each of the abrasive grain similar to the micro milling tool teeth. Then, fundamental parameters for chip formation are identified. Micro milling analogy and modeling of abrasive grits will also be useful in expanding this force model to thermal and stability analyses.

Due to large number of variables in the milling tool geometry, there are several force models for milling processes. Empirical, semi-analytical and analytical models are the main three categories for these models. In early studies, simplest milling force model is the average rigid force model which assumes that the average power consumed, torque and tangential cutting force are proportional to the material removal rate [31]. It is also valid for grinding operations, there are numerous studies reported earlier which uses material removal rate as the main criteria for determination of the process forces. However there is no direct relationship between the material removal rate and the cutting forces both for milling and grinding operations.

Afterwards, researchers realized that more detailed models which give insight about the process are required for more accurate predictions. As the model represents the cutting mechanism better and covers more variation of the process parameters, number of calibration experiments reduces. Therefore, solid understanding of the process and cutter tool geometry is required. In milling operations, geometrical properties of the cutter teeth are known or measurable since they are defined with tight tolerances. Rake angle, oblique angle, hone radius etc. are all known and can be used in the model directly.

It is not the case for abrasive machining since the complexity of the abrasive wheel which contains various abrasive particles. They are randomly distributed on the wheel surface which makes impossible to know the geometrical properties of each of them. Therefore, geometrical properties should be identified as discussed in Section 3. As the getting an insight or performing actual topography measurements of abrasive wheel surface become possible with technological developments, researchers agree more on that each grain performs cutting action individually similar to the milling process. Once the mechanism of the chip formation is investigated in the milling tooth or abrasive grain scale, it is possible to develop trusty process models which give more accurate predictions.

5.1 Modeling of the Process Forces

In abrasive machining, unlike milling tool, each grain has unique geometric and location properties which mean uncut chip thickness, effective axial and width of cuts per grit should be investigated individually. It can be considered as a cutting model for a single cutter tooth, but applied to every active abrasive grain in the contact zone between abrasive wheel and the workpiece. As a final step, all of the forces are projected into X, Y and Z axes since

tangential, normal and radial force directions are not identical due to the unique geometric properties (ie. rake and oblique angle) of the abrasive grains.

Semi-analytical milling force equations are modified for abrasive machining as follows:

$$\begin{aligned}
 F_{t-grain} &= K_{tc} \times h \times b + K_{tp} \times b \\
 F_{n-grain} &= K_{nc} \times h \times b + K_{np} \times b \\
 F_{r-grain} &= K_{rc} \times h \times b + K_{rp} \times b
 \end{aligned} \tag{12}$$

In these equations K_{tc} , K_{tp} , K_{nc} , K_{np} , K_{rc} and K_{rp} are to be identified empirically but can be used for other cases with the same abrasive wheel and workpiece pair. K_{tc} , K_{nc} and K_{rc} coefficients are for chip formation; K_{tp} , K_{np} and K_{rp} are for ploughing forces. Ploughing forces are obtained by linear regression analysis and subtracted from the total forces in order to identify the average chip formation force per grain. After that step, K coefficients for both chip formation and ploughing components are identified. Expressions for other geometrical parameters, i.e. wheel surface area, total number of abrasive grits, number of active cutting grains and contact area are given below in order.

$$\begin{aligned}
 W_{area} &= 2 \times \pi \times (D/2) \times w \\
 T_{grains} &= W_{area} \times C \\
 A_g &= l_{real-area} \times C \\
 l_{c-area} &= l_c \times b
 \end{aligned} \tag{13}$$

Contact length estimation using thermocouple measurement method is used for better accuracy as stated in previous section. Wheel surface area is straightforward to calculate and since C (active grain number in mm²) value was identified, grain number per millimeter square times wheel area is equal to the total number of abrasive grit on the cutting tool. Active grain number is obtained by multiplying C with contact area; which is contact length times radial depth of cut. Geometrical properties of the abrasive grits were checked in order to determine whether they are active or not in Section 3. Even they are active, that does not mean their properties are identical which means their chip formation mechanism is different. Therefore each of them are investigated separately by considering their height, width, rake angle, oblique angle and edge radius that are assigned through Gaussian distribution.

Simultaneous position of an abrasive grit in the cutting zone and the corresponding chip thickness at each time increment can be calculated as presented in Section 3. Once the chip thickness is known, by using abrasive grit width, it is possible to calculate the forces per that

specific grit. Hence, total process forces can be obtained by integrating them over the active number of grits.

$$\begin{aligned}
 F_{t-total} &= \int_{i=1}^{A_g} F_{t-grit(i)} \\
 F_{n-total} &= \int_{i=1}^{A_g} F_{n-grit(i)} \\
 F_{r-total} &= \int_{i=1}^{A_g} F_{r-grit(i)}
 \end{aligned} \tag{14}$$

Oblique cutting theory is used in this paper [32] by considering normal, tangential and radial directions. Radial direction is usually ignored in the literature for grinding operations, however; it is vital for circumferentially grooved wheels due to the 3D geometry of grooves and abrasive grits on its walls. For the sake of accuracy, single grit's workpiece engagement is divided into small portions and force analysis is done accordingly. As it is illustrated in Figure 5.1[14], grit-workpiece engagement section is divided into sections in order to investigate the local angles such as side edge cutting, effective rake and oblique angles. Afterwards, they are used to calculate forces at that particular section and projected into normal, tangential and radial directions in order to obtain total process forces for that grain. Figure 5.1 is an exaggeration in order to illustrate the methodology properly; section heights should be small enough to be precise in force calculations. It has been noted that by using this local sectioning and projection analysis, more accurate results are obtained for process forces.

In the third deformation zone, grit and workpiece are in contact, however; there is no cutting action. Identified third deformation zone forces (ploughing) are added to the cutting forces as a final step to obtain total process forces. Chip formation force is calculated by using the equations 12 to 14 and fundamental parameters such as shear stress and friction coefficient between the grits and the workpiece can be identified.

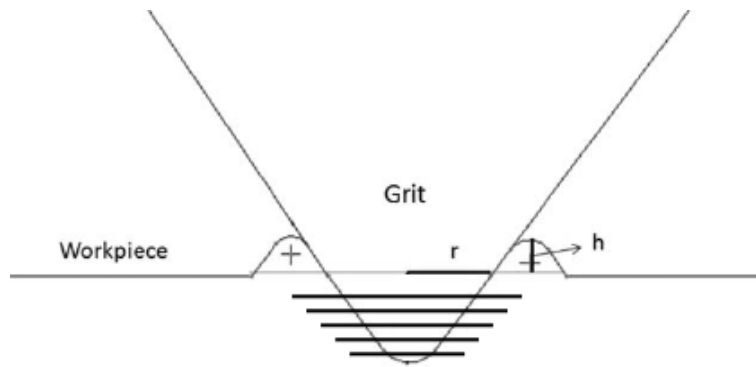


Figure 5.1: Grit engagement section and division into sections

In the case of non-grooved wheels, process forces can be predicted by equations and the methodology presented until now. However, for the circumferentially grooved wheels [10], grooves and grits on the groove walls should be carefully investigated in order to predict the forces.

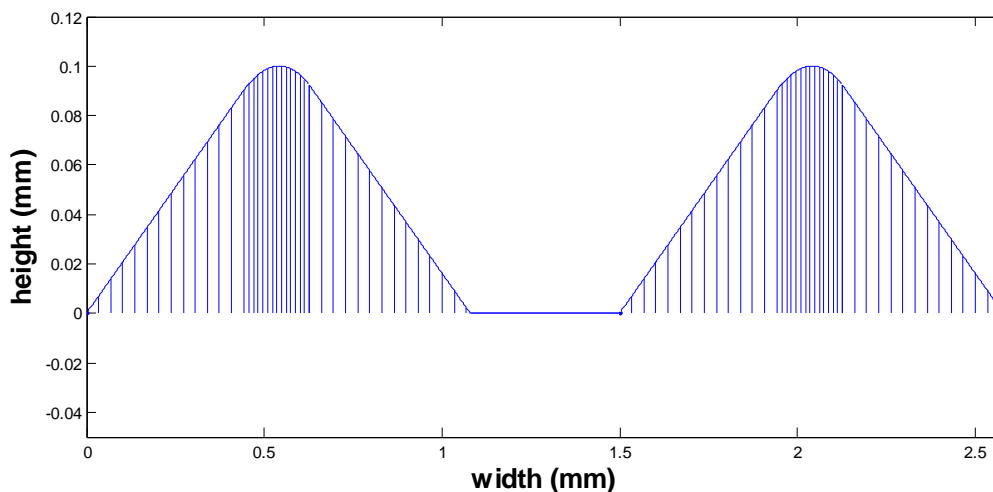


Figure 5.2: Groove profile on the wheel (dressing tool tip)

As it can be seen from Figure 5.2 (2 grooves included), grooves are investigated by sectioning them similar to the grit edge radius analysis. Tangential, feed and radial directions are determined for each element and uncut chip thickness per section is calculated. Black, green and red lines are tangential, feed and radial directions, respectively (Figure 5.3). Sectioning is arranged such that each element has only one abrasive grain. Once the uncut chip thickness per grain is calculated for a grain on the groove wall, by using local direction and angles, forces are calculated and projected into the global X, Y and Z axes as done for the grains on flat regions of the wheel.

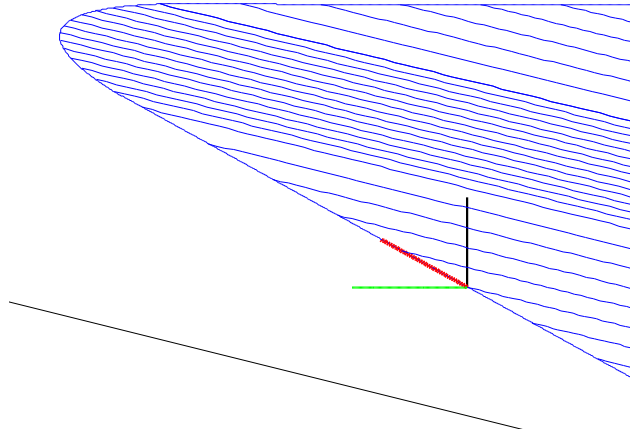


Figure 5.3: Tangential (black), feed (green) and radial (red) directions

Cutting coefficients in the Equation 12 can be calculated as follows:

$$\begin{aligned}
 K_{nc} &= \frac{\tau_1}{\sin \phi_s} \frac{\cos(\beta_n - a_n) + \tan \lambda_s \tan \eta_c \sin \beta_n}{\sqrt{\cos^2(\phi_s + \beta_n - a_n) + \tan^2 \eta_c \sin^2 \beta_n}} \\
 K_{tc} &= \frac{\tau_1}{\sin \phi_s} \frac{\sin(\beta_n - a_n)}{\sqrt{\cos^2(\phi_s + \beta_n - a_n) + \tan^2 \eta_c \sin^2 \beta_n} \cos \lambda_s} \\
 K_{rc} &= \frac{\tau_1}{\sin \phi_s} \frac{\cos(\beta_n - a_n) \tan \lambda_s - \tan \eta_c \sin \beta_n}{\sqrt{\cos^2(\phi_s + \beta_n - a_n) + \tan^2 \eta_c \sin^2 \beta_n}}
 \end{aligned} \tag{15}$$

where η_s is the shear flow angle, η_c is the chip flow angle, a_n is the normal rake angle and β_n is the normal friction angle. Normal friction angle can be calculated as $\beta_n = \tan \lambda_a \cos \eta_c$ where $\mu_{sliding}$ is the sliding friction coefficient and identified from Equation 36. Corresponding angles and the oblique cutting diagram is illustrated in Figure 5.4.

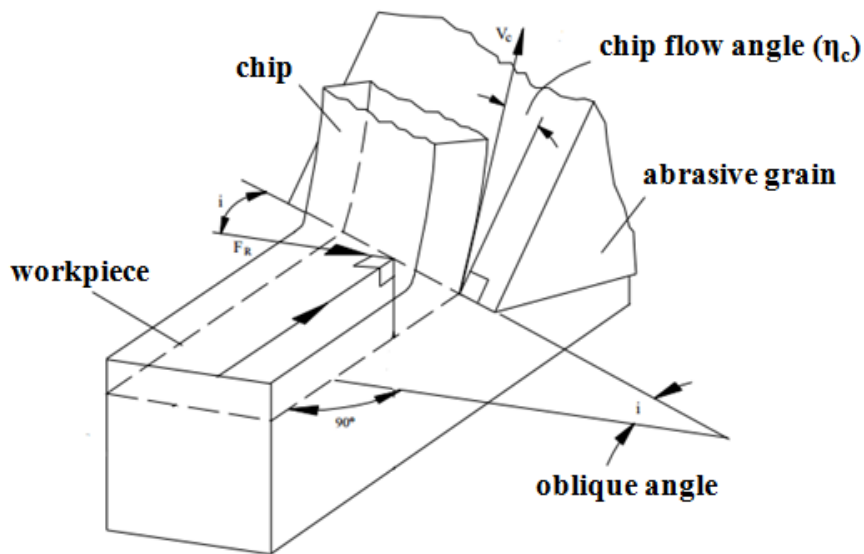


Figure 5.4: Oblique cutting diagram

In oblique cutting, the edge of the abrasive grit is not perpendicular to the cutting velocity which results in a three dimensional cutting geometry and a chip flow direction which is not parallel to the cutting velocity.

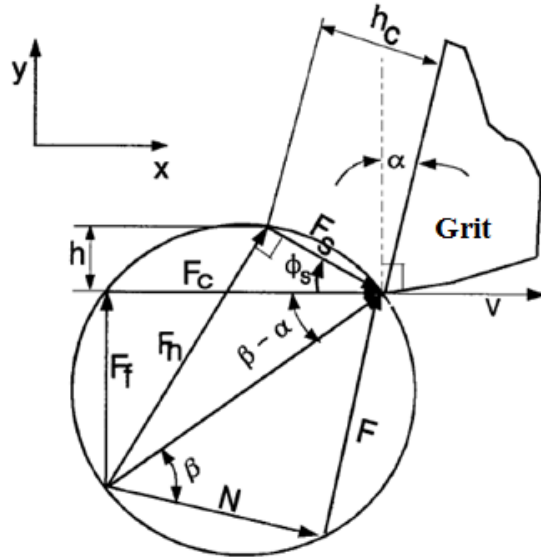


Figure 5.5: Orthogonal cutting force diagram

The shear angle can be identified from the chip ratio r calculated as h/h_c , h being the uncut and h_c cut chip thickness.

$$\phi_s = \tan^{-1}\left(\frac{r \cos \alpha}{1 - r \sin \alpha}\right) \quad (16)$$

Uncut chip thickness was calculated in Section 4. However, in order to calculate the chip ratio, cut chip thickness should be measured by collecting chips after each operation. Considering that the cut chips in abrasive machining have 1-10 μm thickness in general, it is almost an impossible task to collect them with regular tools. A special suction or collection system can be developed to collect and measure cut chip thickness per grit for further analysis. Even so, it will be a hard task to determine which cut chip belongs to which abrasive grit which is required for force per grit calculation.

In this study, shear angle is calculated from Merchant's equation which uses minimum energy principle.

$$\phi_s = \frac{\pi}{2} + \frac{a_n}{2} - \frac{\beta_n}{2} \quad (17)$$

Equation 17 uses great simplifications by assuming that the primary shear zone has a constant thickness throughout the width of cut. Detailed shear angle calculation is presented in the next section by more detailed analysis.

The apparent friction ratio and friction angle should also be identified from the measured data.

$$\mu_a = \tan \beta_n = \frac{F}{N} = \frac{F_f + F_c \tan \alpha}{F_c - F_f \tan \alpha} \quad (18)$$

Shear stress for orthogonal case is identified by Equation 19 which is required for cutting coefficient calculations.

$$\tau = \frac{F_c \cos \phi_s - F_f \sin \phi_s}{b_{grit} h} \sin \phi_s \quad (19)$$

5.2 Prediction of Chip Flow Angle

Chip flow angle for the inclined grits can be assumed as equal to the oblique angle by following the Stabler's chip flow assumption [50]. The rule assumes that the chip moves parallel to the cutting velocity vector, without bending after it is cut [38]. Shaw et al. [39] claimed that the chip flow angle varies with the normal rake angle and friction by experimental analysis. In order to overcome these issues and calculate chip flow angle accurately, Russel and Brown [33], Zorev [34], Oxley [35] and Whitfield [36] proposed equations, discussed the chip flow mechanism and examined the effects of cutting conditions and tool geometry on the chip flow angle experimentally.

It has been noted that it is reasonable to assume that the shear force and shear velocity directions are equal. Experiments show that the chip ratio and chip flow angle are independent of both the width of cut and the chip thickness. Armarego and Brown [37] derived the following expression from the previous studies:

$$\tan(\phi_{sn} + \beta_n) = \frac{\cos \alpha_n \tan i}{\tan \eta_c - \sin \alpha_n \tan i} \quad (20)$$

ϕ_{ns} is the normal shear, β_n is the normal friction and α_n is the normal rake angle. Derivation and calculation of these angles can be found in [38]. The following expression for the chip flow angle η_c is obtained as [37]:

$$A \sin \eta_c - B \cos \eta_c - C \sin \eta_c \cos \eta_c + D \cos^2 \eta_c = E \quad (21)$$

where;

$$\begin{aligned}
 A &= r \cos \alpha_n + \cos i \tan \beta \\
 B &= \tan \beta \sin \alpha_n \sin i \\
 C &= r \sin \alpha_n \tan \beta \\
 D &= r \tan \beta \tan i \\
 E &= \sin i \cos \alpha_n
 \end{aligned}
 \tag{22}$$

Chip ratio r , which is required for the equations listed above, is calculated from Equation 16 and 17. Measurement of the cut chip thickness is a difficult task in abrasive machining as mentioned previously. Equation 21 is solved numerically for each operation by Newton-Raphson Method.

5.3 Identification of the Ploughing Forces

Apart from cutting forces, contribution from the third zone to the process forces should also be considered as mentioned earlier. Due to the plastic deformation, as abrasive grain meets with workpiece and exceeding yield stress of the material, rubbing forces occur. Next; the grit starts to penetrate into the workpiece, displaces it and ploughing forces come into the scene. These two phases are taken as one and identified by linear regression analysis in this study (Figure 5.6). They are considered as rubbing and ploughing forces at the third zone. By excluding the 3rd zone effect, it is assumed that the chip formation mechanism is similar to the milling operation which is the main idea of the developed model.

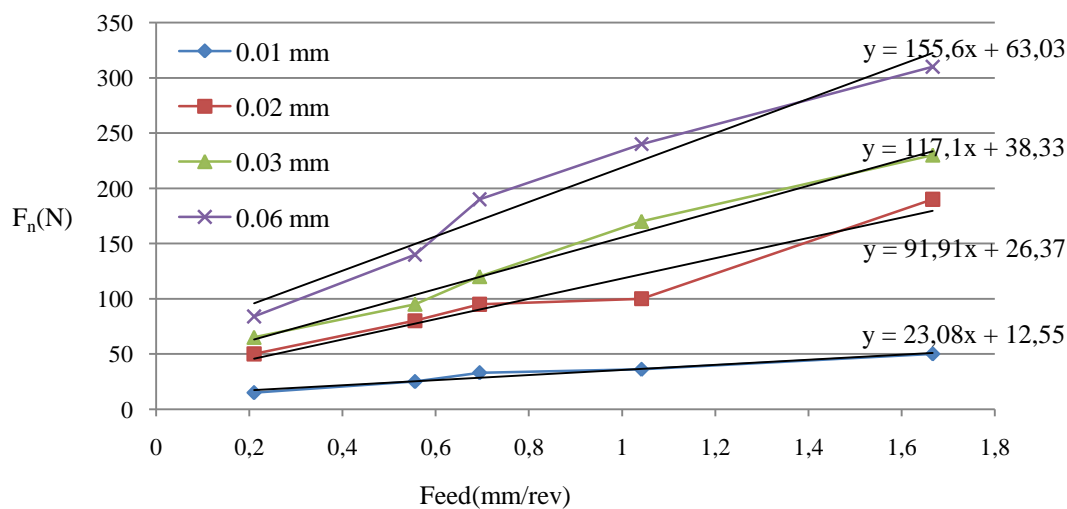


Figure 5.6: Ploughing force identification

A sample linear regression analysis is shown in Figure 5.6. Ploughing forces in the normal direction are identified via first degree curve fit and the equations are presented on the figure. According to the fitted regression equation, there should be a force even the feed rate is zero. It is believed that this portion of the equation is the ploughing force which is the results of the third deformation zone. Ploughing forces are 12, 26, 38 and 63 N for 0.01, 0.02, 0.03 and 0.06 mm axial depth of cuts, respectively. They are identified per grit as: 0.009, 0.012, 0.017 and 0.023 N for 0.01, 0.02, 0.03 and 0.06 mm axial depth of cuts as well.

The linear edge force model was used by Armarego and Epp [40] in formulating the milling forces for zero helix cutters and by Yellowley [41] for analytical mean force and torque formulations in peripheral milling operations. The linear edge force model represents a better physical interpretation of the cutting process than other models (ie. exponential force model) due to the advantage of having linear force coefficients. However, there is no accurate model in the literature for the prediction of the edge-ploughing forces, so they have to be determined experimentally as done in this study. Linear regression analysis is fast, easy to implement and gives judicious results.

There are semi-analytical or analytical studies that focus on calculation of the third zone forces by calculating a stagnation point at the tool tip and dividing tool into regions [42]. Yet their accuracy and ability to model both tool and material behavior in the third deformation zone is not proved.

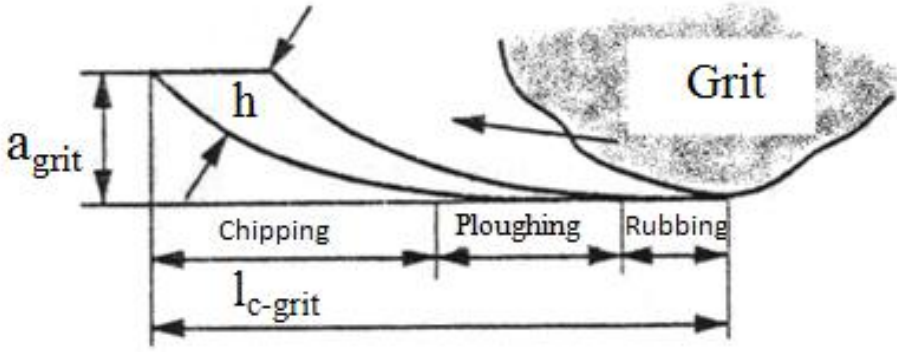


Figure 5.7: Three phases for grit-workpiece interaction

As the number of measured forces with different feed rates increases, fitted regression equation becomes more reliable. Especially for the measured forces at low feed rates, even slight changes in the measured forces can cause significant changes in the identified ploughing forces. Therefore, in order to identify the ploughing forces, at least five feed rates with two of them being considerably low are used. It should be noted that the both calibrated cutting and

ploughing force coefficients cover a single cutting speed. If the cutting speed changes, all of the coefficients should be re-calculated in order to predict the process outcomes.

Need of calibration experiments for each cutting velocity is the drawback of the presented model similar to the case with most of the semi-analytical force models for turning, milling, grinding and other machining processes. In the next section, a solution for that issue is presented by also modeling the material behavior of the workpiece by thermomechanical approach.

5.4 Measured and Predicted Process Forces

In this section, the same equipment is used for the experiments as in Section 3 in order to validate predicted forces by the presented semi-analytical model. A milling machine tool is used with an adequate setup to measure the forces as shown in Figure 5.8. AISI 1050 steel and 150x25x20 SiC 80 M vitrified grinding wheel are used as workpiece and tool respectively. Single point diamond dresser with 2 carat grade is used for dressing the wheel. Four different axial depth of cuts at 0.01, 0.02, 0.03 and 0.06 mm and at four feeds; 0.56, 0.69, 1.04 and 1.67 mm per revolution with 30.16 meter per second cutting speed are used as process parameters.

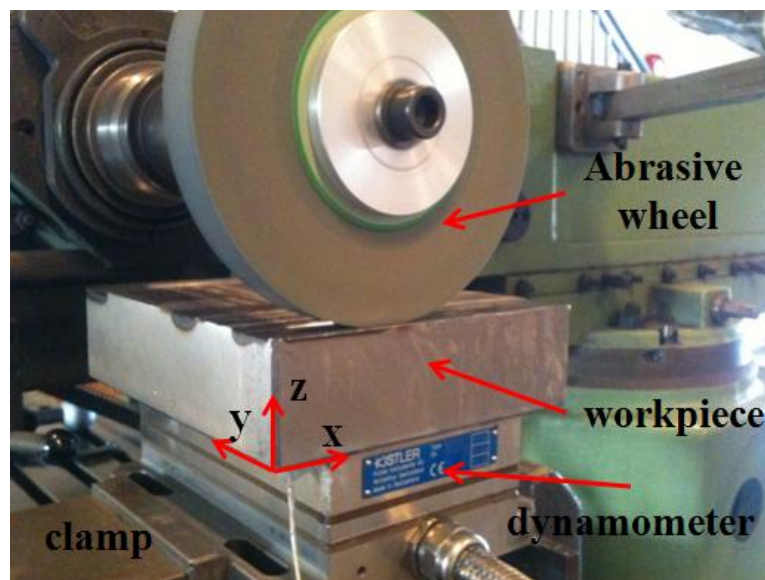


Figure 5.8: Setup for force experiments

A control unit and a BNC board which converts analog data to digital are used with NI Labview software to collect force data during the process. The wheel is dressed after each set of experiments, one set includes four experiments which are the four axial depth of cut values with single feed. Devices and the software with the dressing tool can be seen in Figure 5.9.

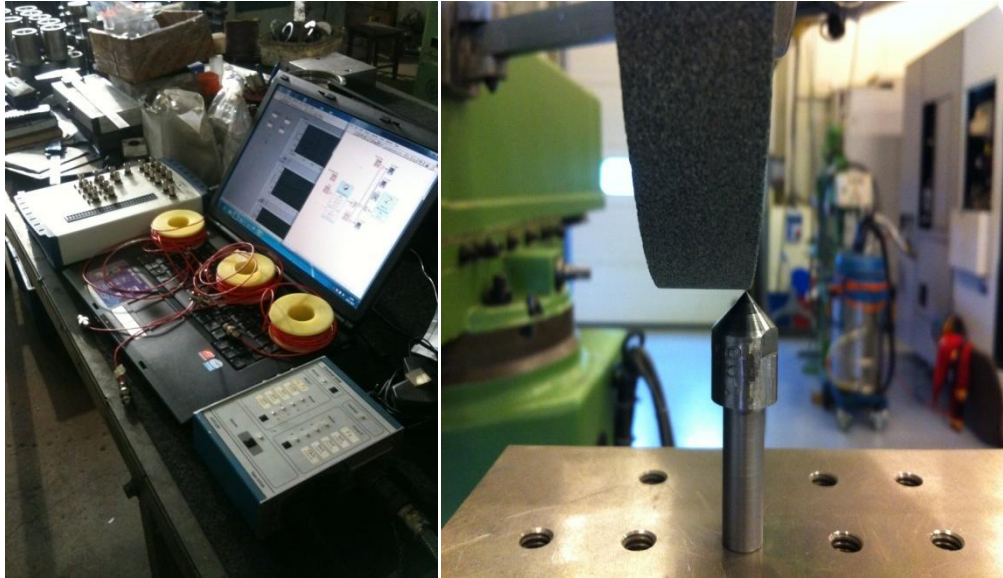


Figure 5.9: (a) Force measurement devices (b) Dressing tool

Dressing conditions are determined from catalogue for single point diamond dresser as 0.2 mm depth to the wheel and 152 mm/sec feed rate. No coolant is used in these experiments in order to avoid miscalculations due to lack of convection heat transfer model when measuring process temperatures in Section 6. K_{tc} , K_{nc} and K_{rc} are identified by the first four experiments conducted at 0.01 mm axial depth of cut and at four feeds (Table 5.1).

Cutting coeff. / feed	0.56 (mm/rev)	0.69 (mm/rev)	1.04 (mm/rev)	1.67 (mm/rev)
K_{tc} (MPa)	2301	2521	2800	2401
K_{nc} (MPa)	4501	6202	5701	4201
K_{rc} (MPa)	820	990	1200	1450

Table 5.1: Identified cutting coefficients

After the force coefficients are determined, the forces for the remaining 12 experiments can be calculated with the presented semi-analytical model. The experiments are repeated twice for both SiC and Alumina wheels for reliability. It is shown that if the abrasive wheel topography, C and the force coefficients are identified correctly, process forces can be predicted accurately. C was identified as 5 in Section 3 for the SiC 80 M wheel that is used in these experiments. Ploughing force components are subtracted from the measured forces in order to obtain the chip formation portion which was compared with the predicted cutting

forces. But the comparison with measured and simulated values that is presented in this section are for the total process forces which were obtained by adding identified ploughing forces to the calculated cutting forces.

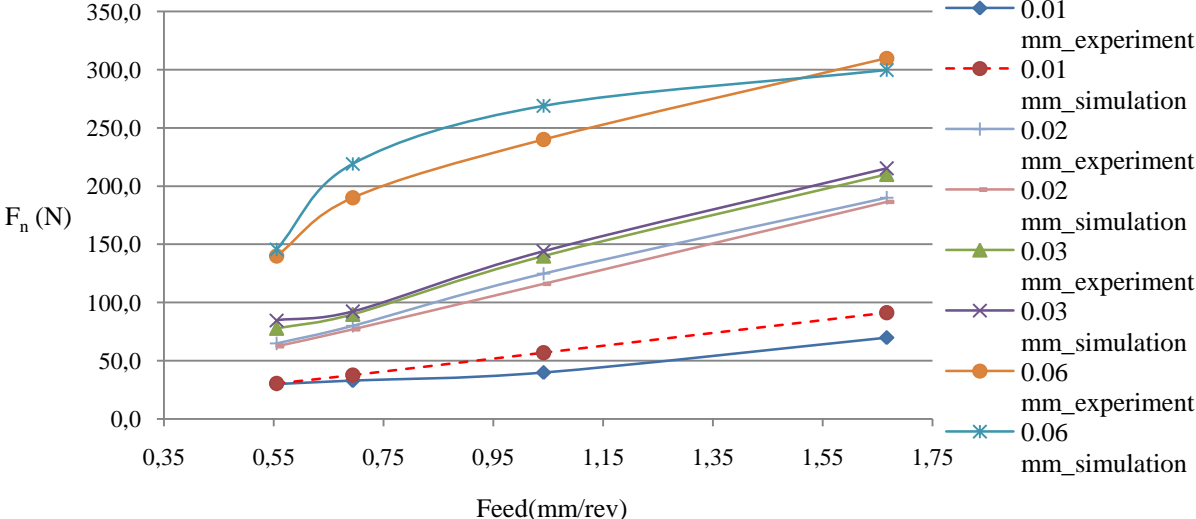


Figure 5.10: Experimental & Model Results (Total Forces)

Predicted and measured forces per grit are given in Figure 5.11. Forces per grit did not measured directly since it would require a single grit wheel and adequate equipment. It is derived backwards from the measured total force since the number of active grains is known. Therefore it can be referred as an average force per grit rather than a unique value for a particular grit. In reality, since grit has unique geometrical properties, corresponding forces should be different for each of them.

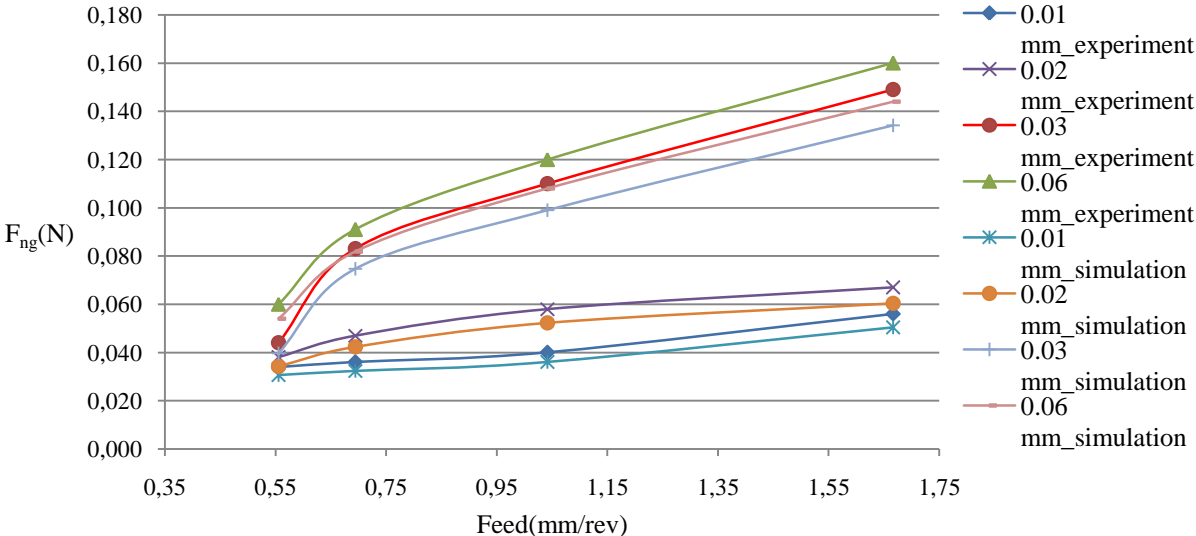


Figure 5.11: Experimental & Model Results (Average forces per grit)

Identified ploughing forces are given in Table 5.2 which was presented in previous section Figure 5.6.

Ploughing coeff. / feed	0.01 (mm)	0.02 (mm)	0.03 (mm)	0.06 (mm)
F_{tp}	8,22	14,50	21,64	32,21
F_{np}	12,55	26,37	38,33	63,03
F_{rp}	0,22	0,47	0,71	0,88

Table 5.2: Ploughing forces for 3 directions

Ploughing coefficients are calculated as 720, 1255 and 367 N/mm for tangential, normal and radial directions, respectively. Ploughing forces can be calculated by these coefficients and then added to the predicted cutting forces.

By using Merchant's Circle and his theory for chip formation mechanism, shear and friction angles can be calculated (Equation 17 and 18). Geometric properties are known by topography investigations and friction coefficient can be calculated from experimental data. Shear angle and friction coefficient (μ) values are given in Table 5.3. Shear angle is identified by using Merchant's Circle and shear stress can be predicted. Uncut chip thickness per grain and width of grain are known from Section 3 and 4.

#	a (mm)	feed_r (mm/rev)	ϕ_s (degrees)	μ_a	Shear Stress (MPa)
1	0.01	0.56	29.52	0.70	452
2	0.02	0.56	35.35	0.66	1284
3	0.03	0.56	36.24	0.64	1286
4	0.06	0.56	30.13	0.68	1061
5	0.01	0.69	32.78	0.66	544
6	0.02	0.69	32.33	0.64	1088
7	0.03	0.69	28.15	0.72	949
8	0.06	0.69	26.81	0.73	1003
9	0.01	1.04	30.47	0.68	361
10	0.02	1.04	31.72	0.65	745
11	0.03	1.04	29.15	0.70	933
12	0.06	1.04	26.57	0.75	835
13	0.01	1.67	30.82	0.67	318
14	0.02	1.67	31.12	0.66	864
15	0.03	1.67	31.22	0.66	858
16	0.06	1.67	29.93	0.69	776

Table 5.3: Process Parameters and Shear Angle-Stress Results

The simulated forces are in a good agreement with experiments considering the %10.6 average error value for SiC and %13.7 for Alumina wheel.

6 Thermo-mechanical Force & Dual-Zone Contact Model

In this section, a thermo-mechanical model at primary shear zone with dual-zones (sticking and sliding) on the rake face of the abrasive grit is presented for regular (non-grooved) and circumferentially grooved abrasive wheels. The detailed formulation is also presented along with simulation procedure and results. Micro milling analogy for abrasive grits is also used for the thermomechanical model. Rather than using geometrical contact length, more accurate contact length is obtained by measuring grinding temperature during the process. Majority of the semi-analytical force models presented in the literature require calibration of certain coefficients for each cutting velocity and a particular wheel-workpiece pair. By utilizing thermo-mechanical analyses and Johnson-Cook material model, a few calibration tests for an abrasive type-workpiece pair is sufficient to predict process forces for different cases involving the same workpiece and the abrasive material however with different arrangements and process parameters. Micro milling analogy and modeling of the material behavior will also be useful in expanding this model to thermal and stability analyses.

Primary aim of the presented model is on the mechanics of primary and secondary shear zones; therefore ploughing forces from the third deformation zone are determined via linear regression analysis and subtracted from the corresponding grinding forces in this section. They are considered separately and added to the cutting forces as a final step to predict total process forces. The primary shear zone model that was developed by Molinari and Dudzinski [43] and Dudzinski and Molinari [44] is used in this study. They assumed that the primary shear zone has a constant thickness, and no plastic deformation occurs before and after the primary shear zone up to the sticking region on the rake face. Johnson-Cook material model is used to represent the workpiece material behavior [45].

$$\tau = \frac{1}{\sqrt{3}} \left[A + B \left(\frac{\gamma}{\sqrt{3}} \right)^n \right] \left[1 + \ln \left(\frac{\dot{\gamma}}{\dot{\gamma}_0} \right)^m \right] \left[1 - (\bar{T})^v \right] \quad (23)$$

In Equation 23, γ , $\dot{\gamma}$ and $\dot{\gamma}_0$ are shear strain, shear strain rate and reference shear strain rate respectively. A, B, n, m and v are material constants. The actual temperature divided by its critical temperature which is defined as the reduced temperature is defined by Equation 24. T is the absolute temperature, T_r is the reference temperature and T_m is the melting temperature.

$$\bar{T} = \frac{(T - T_r)}{(T_m - T_r)} \quad (24)$$

Shear stress of the material entering to the primary shear zone is denoted by τ_0 and considering the inertia effects; τ_1 , the shear stress at the exit of the shear plane, is not same with τ_0 . τ_0 can be calculated by assuming a uniform pressure distribution along the shear plane [45]. Shear stress at the exit of the shear zone can be calculated via Equation 25 considering the equations of motion for a steady state solution [45].

$$\tau_1 = \rho(V \sin \phi_n \cos i)^2 \gamma_1 + \tau_0 \quad (25)$$

6.1 Dual-Zone Contact Theory and Grinding Approach

Ozlu, Molinari and Budak [45] presented a dual zone contact model for orthogonal cutting where forces in the secondary deformation zone, ie. on the rake face, are calculated by using the predicted sticking and sliding contact lengths between the chip and tool. In this study, process forces are calculated by both sticking-sliding contact analysis and assumption of an average friction coefficient on the rake face of the grit in order to compare their performances. Chip formation mechanism for abrasive machining is usually considered to be orthogonal [1,2,3,4] ; however, it has been noted that consideration of the obliquity improves the accuracy of the thermo-mechanical model [58]. Oblique angle distribution of the grits is obtained as presented in Section 3 and a random oblique angle from that distribution is assigned to each grain for simulations.

As second law of thermodynamics indicates, for a closed system with fixed entropy, the total energy is minimized at equilibrium. A physical situation that increases the shear energy required in the secondary zone will also increase the total shear energy. Afterwards, the shear plane angle tries to reduce the increased total energy. Therefore, the principle of minimum energy states that the stress arrangement that requires minimum total energy is the most probable for generation of the chip during a material removal process. That principle has been commonly used for prediction of shear angle in cutting since Merchant [46], and it is applied in this study as well.

Workpiece material that leaves the shear plane is exerted with a high normal pressure on the rake contact which yields sticking starting from the abrasive grit tip. As material continues to move on the rake face, the normal pressure decreases and the contact condition turns into sliding [45]. This phenomenon can be observed by scanning abrasive grits after an operation. Material stuck on to the abrasive grit's tip towards the rake face is visible; however, it is not

straightforward to verify the predicted sticking and sliding contact lengths considering the stochastic nature of the process. According to the plastic flow criteria, the shear stress cannot exceed the flow stress (τ_1) of the workpiece material on the rake face. Therefore, stress conditions for the sticking and sliding regions can be defined as follows:

$$\begin{aligned} \tau &= \tau_1 & x &\leq l_p \\ \tau &= \mu P & l_p &\leq x \leq l_c \end{aligned} \quad (26)$$

where l_{cr} is the contact length and x is the distance on the rake face from the grit tip (Figure 6.1). In oblique cutting, the third direction and the chip flow angle should also be taken into account for the dual-zone analysis [45]. Pressure and shear stress distribution is selected parallel to the chip flow direction. $P(x)$ is the normal pressure distribution, P_0 is the normal stress on the rake face at the grit tip and ζ is the distribution exponent. Normal force (N) acting on the rake face can be calculated from P_0 as follows [45] (Figure 6.1):

$$N = \int_0^{l_{cr}} P_0 \left(1 - \frac{x}{l_{cr}}\right)^\zeta w_c dx = P_0 \frac{a_{grit} l_{cr}}{\zeta + 1} \frac{\cos \eta_c}{\cos i} \quad (27)$$

The normal force can also be defined in terms of the shear force on the shear plane as [45]:

$$N = F_s \cos \eta'_s \frac{\cos \beta_n}{\cos(\phi_n + \beta_n - \alpha_n)} \quad (28)$$

where the shear force is;

$$F_s = \tau_1 A_s = \tau_1 \frac{a_{grit} h}{\sin \phi_n \cos i} \quad (29)$$

By equating equation 27 and 28, P_0 can be written as:

$$P_0 = \tau_1 \frac{h}{l_{cr}} \frac{\cos \eta_s \cos \beta_n}{\sin \phi_n \cos \eta_c \cos(\phi_n + \beta_n - \alpha_n)} \quad (30)$$

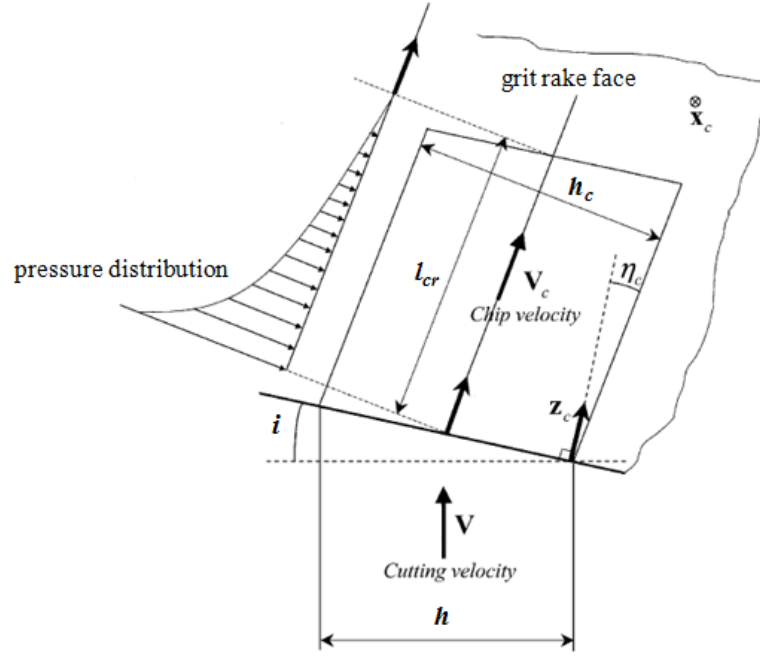


Figure 6.1: Chip flow and the pressure distribution on the grit rake face

6.2 Sticking and Sliding Contact Length Identification

Contact length identification from normal stress distribution on the rake face was studied before by equating the tangential stress to the shear yield stress of the workpiece material at the end of the sticking zone [45]. Once the pressure distribution is identified, sticking contact length on the grit rake face can be calculated as follows [45]:

$$l_p = l_{cr} - l_{cr} \left(\frac{\tau_1}{P_0 \mu} \right)^{\frac{1}{\zeta}} \quad (31)$$

Moment due to normal shear force (M_{sf}) acting on the shear plane at the abrasive grit tip can be calculated by Equation 32 using the assumption of uniformly distributed normal stress on the shear plane. Also moment at the grit (M_{gr}) tip due to the normal pressure on the rake face is calculated. Equating these two moments to each other lead us to the total contact length between chip and abrasive grit.

$$M_{sf} = \tau_1 \frac{a_{grit} h \cos \eta_s \tan(\phi_n + \beta_n - \alpha_n)}{2 \sin^2 \phi_n \cos i} \quad (32)$$

$$M_{gr} = \int_0^{l_{cr}} x P_0 \left(1 - \frac{x}{l_{cr}} \right)^{\zeta} \cos \eta_c a_{grit} dx \quad (33)$$

By plugging Equation 30 into 32 M_{gr} can be extended and the total contact length can be calculated from the moment equilibrium as follows:

$$l_{cr} = \frac{h \sin(\phi_n + \beta_n - \alpha_n)}{2 \sin \phi_n \cos \beta_n \cos \eta_c} \quad (34)$$

Shear and chip flow angles can be calculated as proposed earlier in Section 5.2.

6.3 Sliding and Apparent Friction Coefficients and Forces

Two friction coefficients can be used to define the contact on the rake face: apparent and sliding friction coefficients. Ratio between the total friction and normal forces acting on the rake face is the apparent friction coefficient ($\mu_a = F_{friction} / N$) where total friction force on the rake face can be identified from contact lengths as follows [45]:

$$F_{friction} = \int_0^{l_p} \tau_1 b_{grit} dx + \int_{l_p}^{l_{cr}} \tau_1 \left(1 - \frac{x-l_p}{l_e}\right)^\zeta b dx = \tau_1 b_{grit} \left(l_p + \frac{l_e}{\zeta + 1}\right) \quad (35)$$

where l_e is the sliding contact length on the grit rake face. The normal force on the rake face which was represented by Equation 27 and the relationship between the apparent and sliding friction coefficient is [45]:

$$\mu_a = \frac{\tau_1}{P_0} \left[1 + \zeta \left(1 - \left(\frac{\tau_1}{P_0 \mu} \right)^{1/\zeta} \right) \right] \quad (36)$$

If one of the friction coefficients is known, the other can be calculated using Equation 36. Sliding friction coefficient equation is obtained for an abrasive type-workpiece material pair from calibration tests. Apparent friction coefficient can be detected by this equation and used in the contact length and force calculations.

Once the friction coefficients and corresponding contact lengths are identified, shear angle is calculated by (\emptyset) minimization of the cutting energy as described earlier. A simulation code which uses the proposed thermomechanical model scans a given range of shear angles, and the one that produces the minimum cutting power is selected. Grinding forces per abrasive grit in three directions (tangential, feed and radial, respectively) are obtained by the identified angles and the shear stresses as follows [45]:

$$F_{nc-g} = \tau_1 b_{grit} h \frac{\cos(\beta_n - a_n) + \tan \lambda_s \tan \eta_c \sin \beta_n}{\sin \phi_n \sqrt{\cos^2(\phi_n + \beta_n - a_n) + \tan^2 \eta_c \sin^2 \beta_n}} \quad (37)$$

$$F_{tc-g} = \tau_1 b_{grit} h \frac{\sin(\beta_n - a_n)}{\sin \phi_n \sqrt{\cos^2(\phi_n + \beta_n - a_n) + \tan^2 \eta_c \sin^2 \beta_n} \cos \lambda_s} \quad (38)$$

$$F_{rc-g} = \tau_1 b_{grit} h \frac{\cos(\beta_n - a_n) \tan \lambda_s - \tan \eta_c \sin \beta_n}{\sin \phi_n \sqrt{\cos^2(\phi_n + \beta_n - a_n) + \tan^2 \eta_c \sin^2 \beta_n}} \quad (39)$$

As presented in Section 3, abrasive grits have different uncut chip thicknesses based on their locations and geometric properties. Hence, forces are calculated for each abrasive grain and integrated over number of active grits to obtain the total grinding forces. Ploughing forces are identified through linear regression analysis and can be added to the grinding forces to obtain total process forces as described in previous section.

6.4 Sliding Friction Coefficient Identification and Ploughing Forces

Sliding friction coefficient as a function of cutting speed is obtained through calibration experiments which are conducted at cutting speeds of 7.8 m/s, 12.5 m/s, 15.7 m/s, 19.6 m/s, 24.7 m/s and 31.4 m/s and at feed rates of 0.075 mm/rev, 0.11 mm/rev, 0.15 mm/rev and 0.18 mm/rev. Axial depth of cuts were selected as 0.03, 0.05, 0.1 and 0.15 mm, but it should be noted that the sliding friction coefficient does not change directly with axial depth of cut.

The variation of the sliding friction coefficient with the cutting speed is represented by the following function:

$$\mu = -0.0009V_c^2 + 0.0566V_c - 0.1671 \quad (40)$$

Once the sliding friction coefficient function for a particular abrasive type and workpiece material is identified, it is possible to calculate corresponding friction coefficients for any cutting speed in that region. It means presented model does not require several calibration tests with various cutting speeds which is a major advantage over the semi-analytical force models.

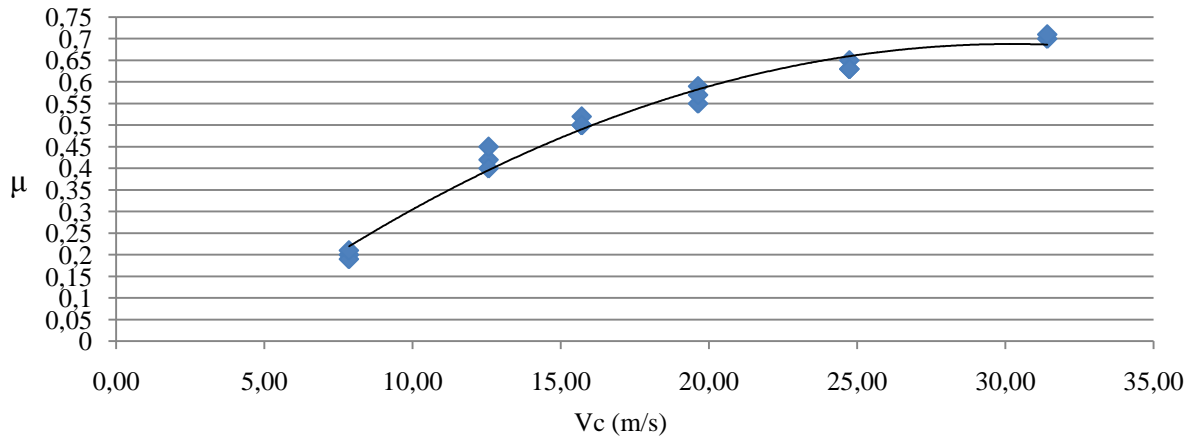


Figure 6.2: Sliding friction coefficient for AISI 1050 steel and SiC abrasive material

As it can be seen from Figure 6.2, identified friction coefficients for a constant cutting speed with different feed rate or axial depth of cuts are considerably close to each other. Sliding friction increases with the cutting speed since the increase of friction with sliding velocity is in general observed for the regime of small velocities as noted in Philippon et al. [68]. For small velocities, the sliding friction increases with V_c , with large values of V_c , the opposite trend is observed and the trend for small velocities might be attributed to local inertia effects at the level of contact asperities.

Linear regression analysis was used to determine ploughing forces and corresponding coefficients as presented in Section 5.3, Figure 5.6. Ploughing forces were obtained as 11, 36, 54 and 63 N for 0.03, 0.05, 0.1 and 0.15 mm axial depth of cuts and 7.85 m/s cutting speed. Identification of ploughing force coefficients and real contact lengths were performed by using regular wheel and used for grooved ones as well. B, C and D wheels that were produced by a single point diamond dresser.

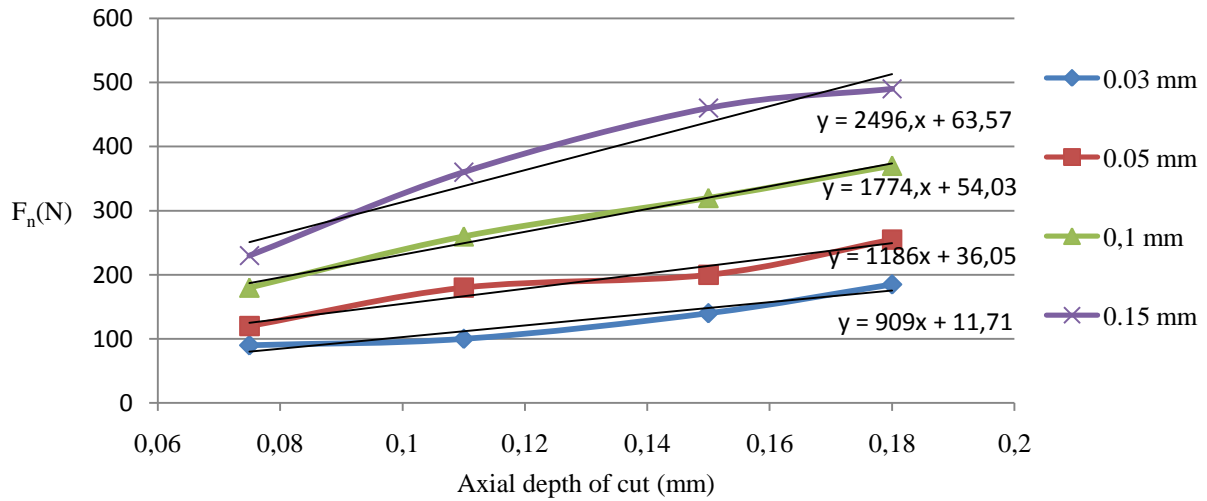


Figure 6.3: Ploughing force identification for $V_c = 7.85$ m/s

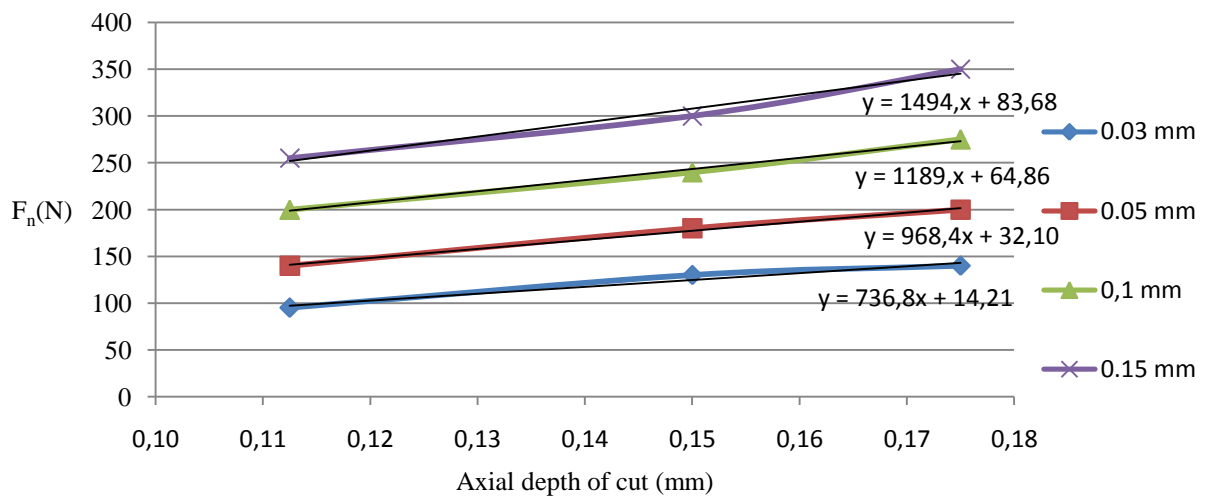


Figure 6.4: Ploughing force identification for $V_c = 12.57$ m/s

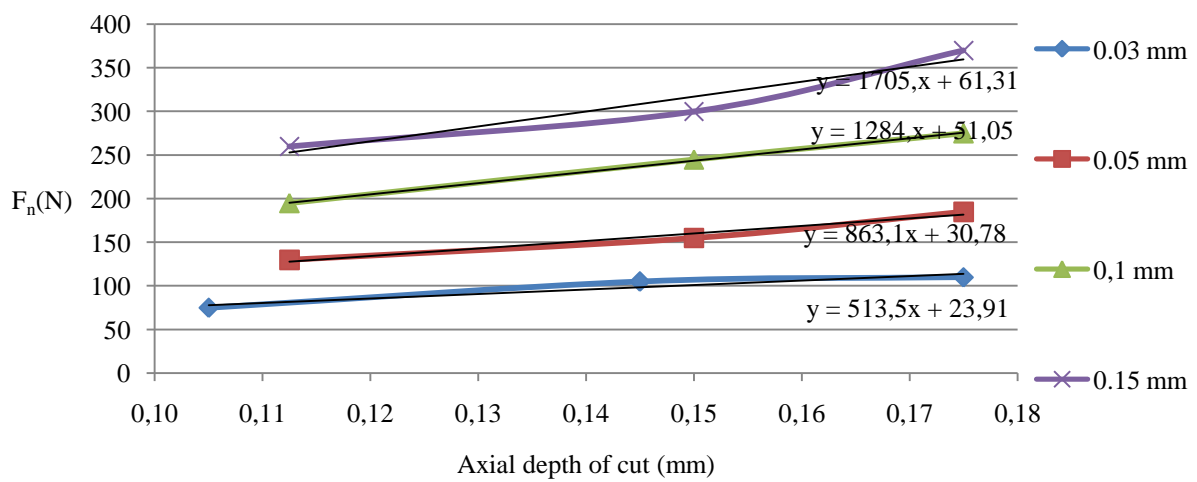


Figure 6.5: Ploughing force identification for $V_c = 15.71$ m/s

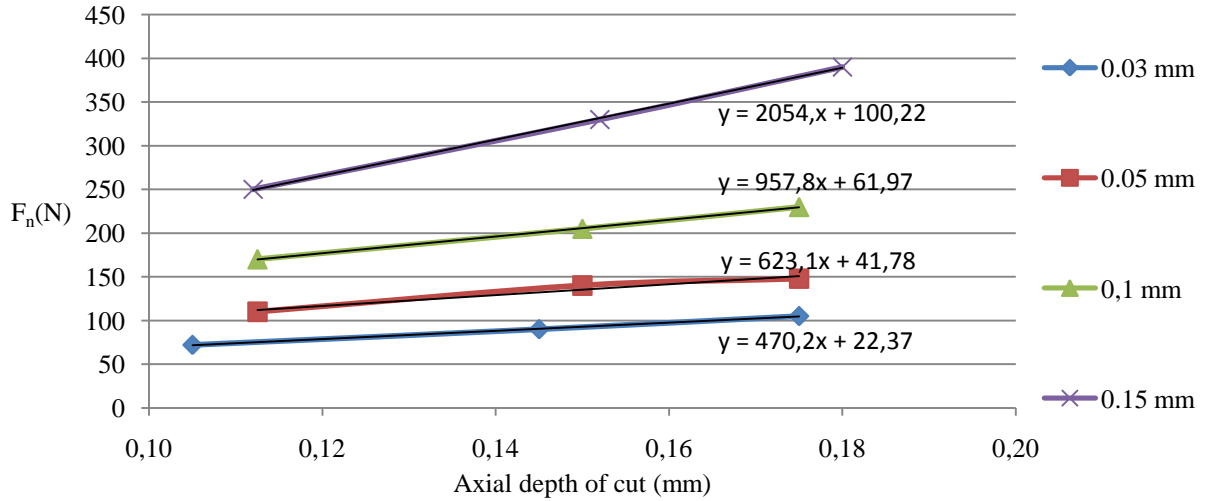


Figure 6.6: Ploughing force identification for Vc = 19.63 m/s

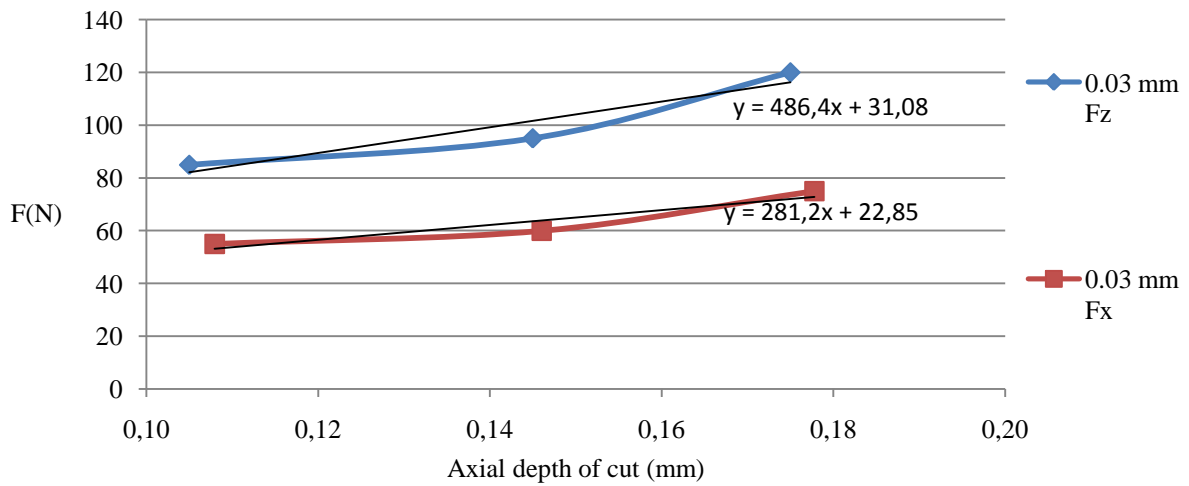


Figure 6.7: Ploughing force identification for Vc = 24.74 m/s

6.5 Johnson-Cook Material Model Parameters

The Johnson-Cook parameters for AISI 1050 steel are obtained from Ozlu, Molinari and Budak [45] as presented in Table 6.1.

A (Mpa)	B (Mpa)	n	m	v
880	500	0.234	0.0134	1

Table 6.1: Johnson-Cook Parameters for AISI 1050 Steel [22]

Ozlu, Molinari and Budak [22] calibrated these values with the experimental values of the shear stress in the shear plane obtained from the measurements of the cutting forces and the shear angle. They used initial values of the parameters from Jaspers and Dautzenberg [47] and updated them via non-linear regression analysis by modifying the strain hardening part of the equation (A and B). The parameters m and v which are rate and the thermal sensitivities are

taken directly from Jaspers and Dautzenberg. Thickness of the shear planes is taken as 0.025 mm, which is a typical value for steels as Dudzinski and Molinari reported [44]. This value may be quite large for abrasive machining especially in the sense of grit chip formation mechanism; however, it has been observed that the thickness of the shear zone does not affect the results significantly. Therefore, same value is used in this study as well. Reason for that is the weak rate sensitivity of the workpiece material (AISI 1050 Steel).

6.6 Shear Angle Predictions

The principle of minimum energy is used to determine the shear angle for each process as mentioned earlier. Chip formation energy and the energy spent on the grit rake face between chip and grit are added and total process energy is calculated. Afterwards, a range for shear angles is determined and model is run with 0.01 degree increments in that range. Once the scan is over, the shear angle which gives the minimum cutting energy is selected. The shear angle is also identified experimentally from Merchant’s formulation and the two shear angles compared. The average difference between the model prediction and the experimental results is 15%. The discrepancy could be attributed to the assumptions in Merchant’s shear angle formula or measurement errors in wheel topography identification step. As Ozlu, Molinari and Budak [45] indicate, minimum energy approach combined with the stability analysis of the chip formation and simple minimum energy approach may yield different shear angle values.

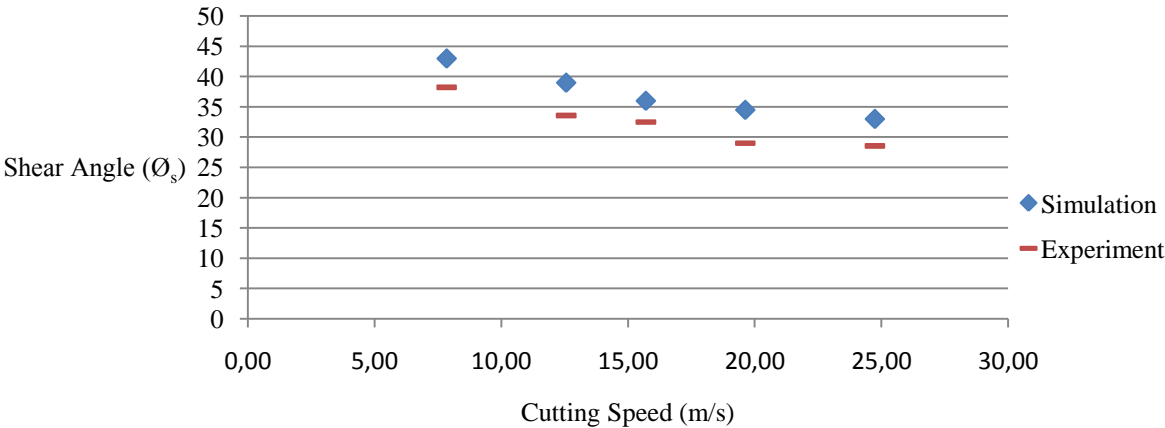


Figure 6.8: Measured and predicted shear angle comparison (feed_r= 0.11 mm/rev, a = 0.03 mm)

6.7 Identification of Contact Length between Grit and Chip

Thermomechanical force model solution procedure was applied to each abrasive grain which means sticking and sliding contact lengths are identified for every one of them. Material that

is stuck on the rake face close to the grit tip can be observed; however, it is almost impossible to identify sticking and sliding contact lengths precisely since determination of the transition point from sticking to sliding is not that straightforward with the confocal 3D measurement system.

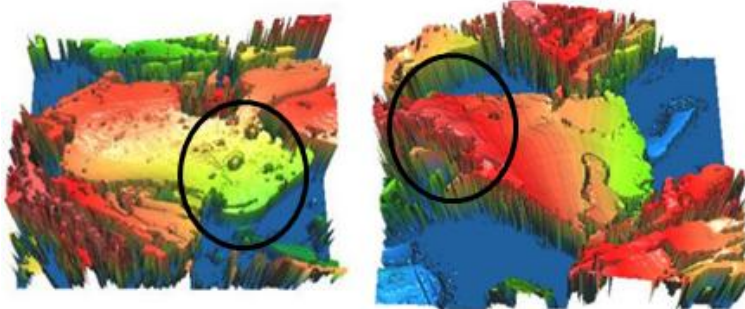


Figure 6.9: Stuck material on scanned grains



Figure 6.10: Regions where stuck material is observed

Therefore, dual zone (sticking + sliding), full sliding and full sticking cases are considered and it has been noted that the dual zone model gives the best results. Sticking and sliding lengths are calculated by equations 31 and 34 as presented in Figure 6.11 for the conditions given in Table 6.2.

Test #	1	2	3	4	5	6	7	8	9	10	11	12
V_c (m/s)	12.5	12.5	12.5	12.5	12.5	12.5	19.6	19.6	19.6	19.6	19.6	19.6
feed _r	0.11	0.15	0.18	0.11	0.15	0.18	0.11	0.15	0.18	0.11	0.15	0.18
a	0.03	0.03	0.03	0.1	0.1	0.1	0.03	0.03	0.03	0.1	0.1	0.1

Test #	13	14	15	16	17	18	19	20	21	22	23	24
V_c (m/s)	12.5	12.5	12.5	12.5	15.7	15.7	15.7	15.7	19.6	19.6	19.6	19.6
feed _r	0.11	0.11	0.11	0.11	0.11	0.11	0.11	0.11	0.11	0.11	0.11	0.11
a	0.03	0.05	0.1	0.15	0.03	0.05	0.1	0.15	0.03	0.05	0.1	0.15

Table 6.2: Selected experiments to present dual zone model results

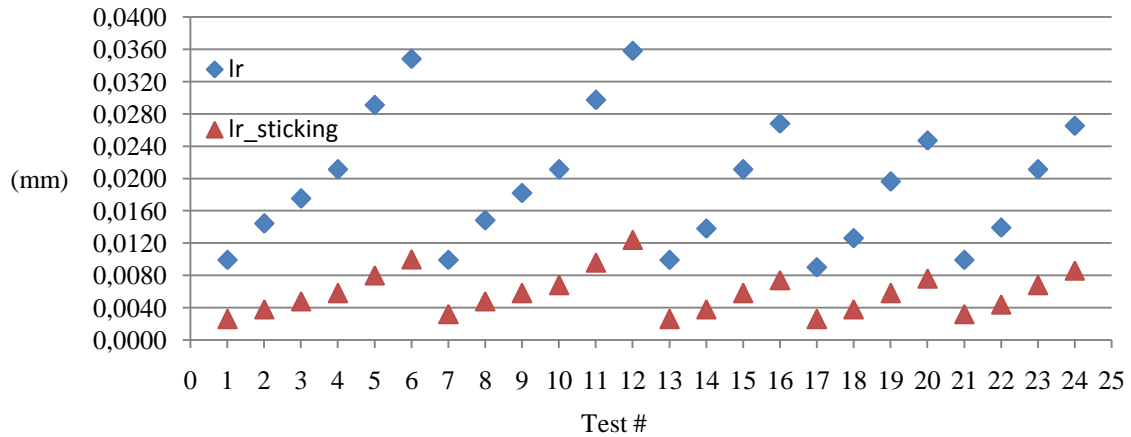


Figure 6.11: Total and sticking contact lengths on the rake face of the grit

6.8 Measured and Predicted Cutting Forces

Experiments have been conducted on a milling machine tool with AISI 1050 steel and 150*25*20 SiC 80 M grinding wheel which are used as workpiece and cutting tool respectively for these tests. Equipment is same with previous tests but process parameters are different, especially the cutting speed. Four different axial depth of cuts at 0.03, 0.05, 0.1 and 0.15 mm and four feed values at 0.075, 0.11, 0.15 and 0.18 mm per revolution with 5 different cutting velocities (7.85, 12.57, 15.71, 19.63, 24,74 m/s) were used in the experiments. Experiment setup can be seen in Figure 5.8 and Figure 5.9. All of the results presented in Section 6 (esp. 6.4, 6.6, 6.7, 6.8) are outcomes of these experiments.

In order to show the necessity and accuracy of the dual zone contact model presented in this study; fully sliding, fully sticking and dual zone approaches are compared with the experimental forces. The comparisons for two different cutting speeds can be seen in Figure 6.12 and Figure 6.13.

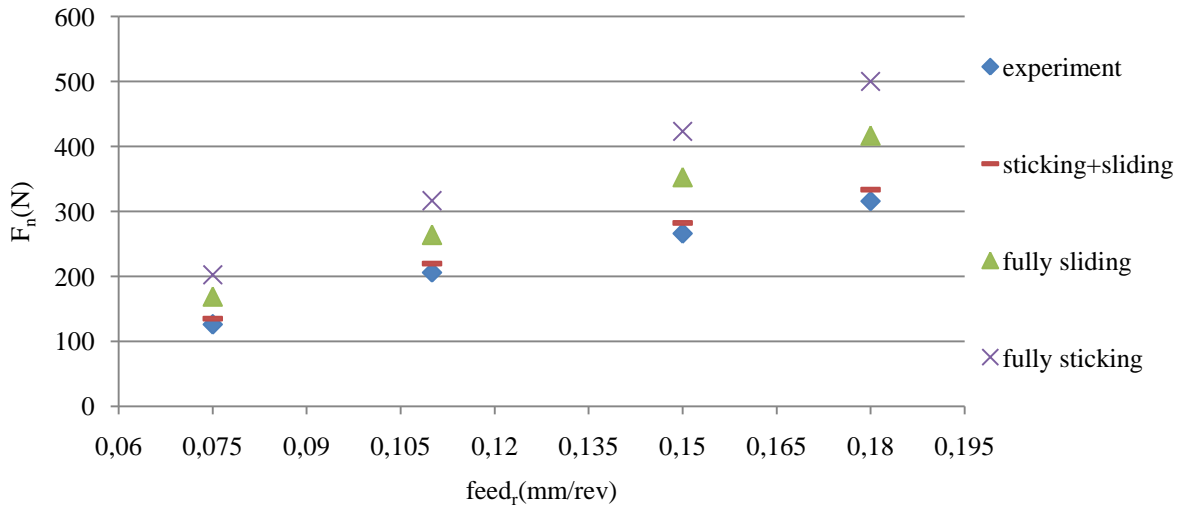


Figure 6.12: Comparison of experimental and predicted results for 7.85(m/s) cutting speed ($a = 0.1$ mm)

As it can be seen from Figure 6.11, sticking contact length is much shorter than sliding length; therefore it was expected to have larger error with fully sticking condition. Fully sliding case is close to the dual zone model due to the fact that in most cases it is the 75-80% of the total contact length between chip and grit rake face.

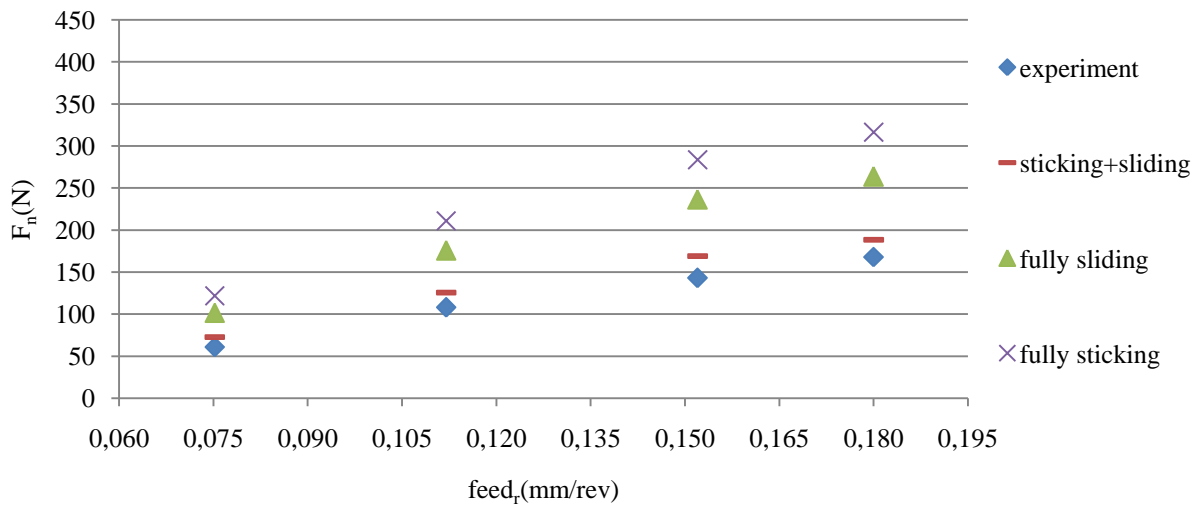


Figure 6.13: Comparison of experimental and predicted results for 19.63(m/s) cutting speed ($a = 0.1$ mm)

For lower feed rates, discrepancy between simulated and measured forces is lower for each case. Due to low contact length between chip and grit, sticking and sliding lengths are close to each other, therefore dual zone, fully sliding or fully sticking conditions gave similar results. Discrepancy between these approaches increases with the feed rate. In addition, it was expected that the fully sliding condition would give lower forces than the dual zone case and the opposite results are observed for the simulation results. It is believed that the reason for that is the increase in the contact length between chip and abrasive grit for the fully sliding condition.

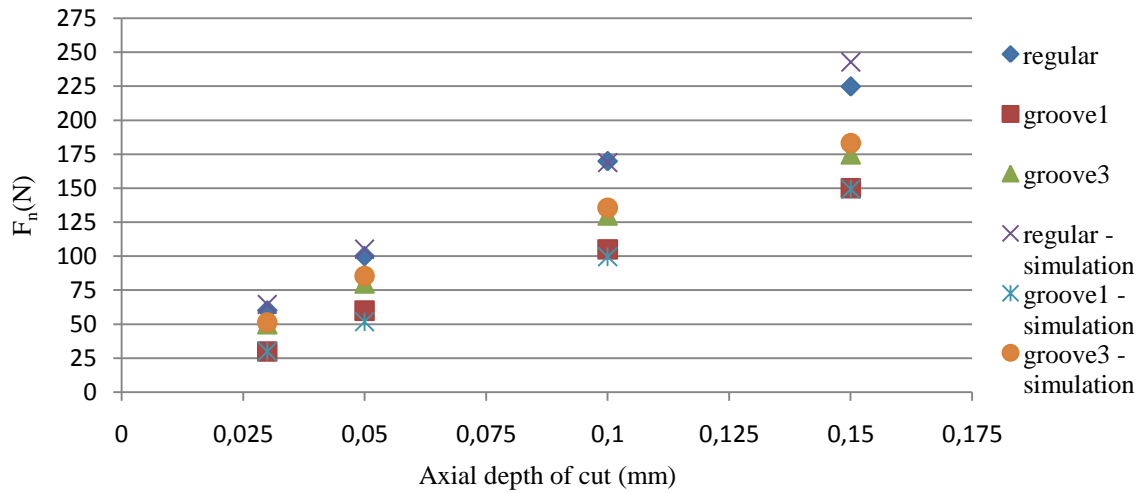


Figure 6.14: Comparison of wheel types (0.11 mm/rev feed)

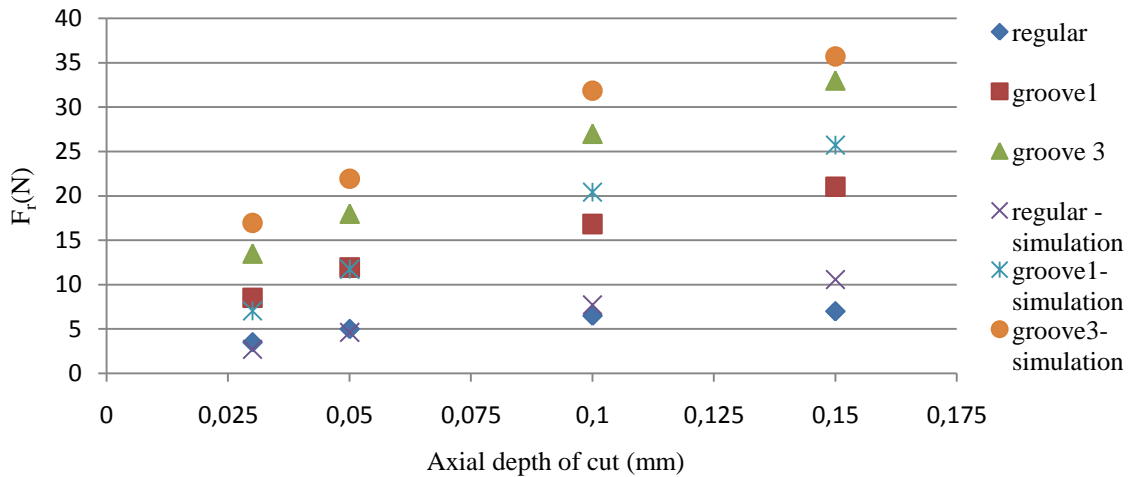


Figure 6.15: Radial forces (feed_r= 0.11 mm/rev)

As it can be seen in Figure 6.12 and Figure 6.13, grinding force predictions obtained by the proposed dual zone model are well correlated with experimental results. Thus, it is obvious from these results that neglecting either sticking or sliding contact lead to significant errors. The dual zone model provides the best prediction capability, therefore even without contact length verification by optical measurements, it can be said that dual zone theory can be applied to abrasive machining processes.

On the other hand, since the presented model works in an abrasive grit scale, by correct calculation of uncut chip thickness (h) and local angles (rake, oblique, chip flow, shear angle etc.), it can be used for various wheel geometries. Figure 6.14 illustrates results for regular, groove 1 (B) and groove 3 (C) type wheels. Process forces can be reduced up to 45% by increasing the number of grooves on the wheel. It has been noted that increasing the groove number is more important than increasing the helix angle of the grooves for obtaining lower

forces. Specific energy was reduced 50% with B wheel which is a measure of the amount of energy required to displace a unit volume material [1].

Radial forces for each wheel are presented in Figure 6.15. It is believed that the assumptions made in the wheel surface topography and grit property identification steps as well as neglecting the single point diamond dresser wear are the main reasons behind the discrepancies between the measured and simulated forces (details can be found in Section 4.3).

Forces in all directions tend to decrease as cutting speed increases. However, high cutting speeds increases the workpiece surface burn risk which will be explained in the next section.

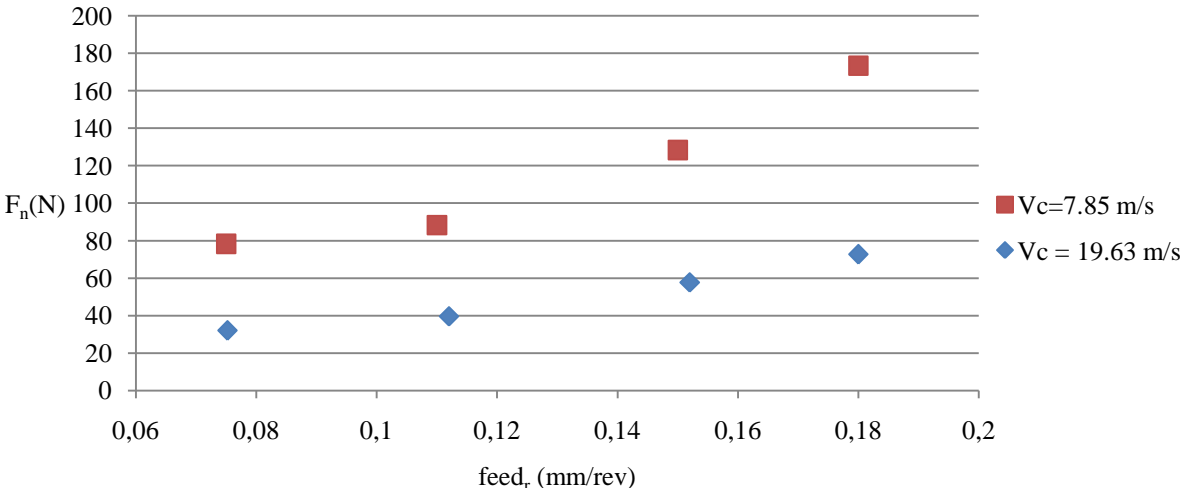


Figure 6.16: Comparison of cutting forces with different cutting speeds (feed_r= 0.11 mm/rev, a = 0.03 mm)

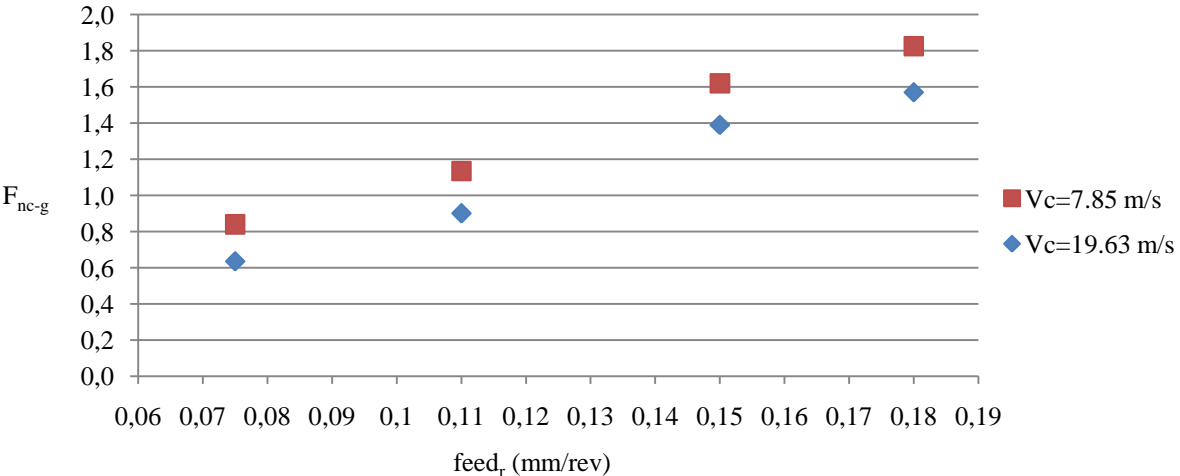


Figure 6.17: Comparison of cutting forces per grit with different cutting speeds (feed_r= 0.11 mm/rev, a = 0.03 mm)

As it can be seen from Figure 6.17, force per grit also decreases with the increasing cutting speed as expected.

7 Temperature Model

This section presents a methodology to detect whether grinding temperatures will cause a surface burn over workpiece material or not by process modeling. Based on the triangular heat flux model, grinding wheel is represented as a 2D moving heat source along the surface where the heat distribution over workpiece is investigated. Predicted temperatures are experimentally validated by using the measurements from the embedded thermocouples in the workpiece. In addition, using the previously developed semi-analytical and thermomechanical force models, the calculated shear stress and shear angle per abrasive grits are used in the primary and secondary zone energy equations in order to determine the chip temperatures. When the burning of the workpiece is initiated, there is a trend of growth of metallic particle adhesion in the abrasive grains of the wheel, having as consequence the increase of the grinding forces which agrees with the visible burn threshold as well. In this study, both force monitoring and visual inspection are used to detect surface burn and burn threshold results agree with the literature. Predicted and measured temperatures agree within approximately 11-14%, hence surface burn occurrence can be predicted by the presented model with an acceptable level of confidence.

Instead of investigating grinding wheel in a macro scale as often done in the literature [11,12,13], abrasive grains are examined individually and energy generated per grain on primary and secondary shear zones as well as third deformation zone are identified. Hence, heat flux into the workpiece and energy that is thrown out by chip can be predicted more accurately. For the model, the first step is to measure and obtain adequate data on abrasive wheel topography and average grit properties such as rake angle, height, width and edge radius (Section 3). Afterwards, cutting forces, shear stress and friction coefficients are calculated for each operation by previously developed semi analytical or thermomechanical force models (Section 5 & 6). Forces are needed for the calculation of the process energy, thus temperature in the cutting zone. Last step is to calculate total energy that is produced during the operation and use it for the semi-analytical temperature model. Following this procedure, it is possible to predict surface burn occurrence before the operation.

Surface burn and metallurgical damages on workpiece material due to high temperatures can be considered as a major drawback for abrasive machining. However; rather than using experimental or trial and error methods, by developing process models and obtaining optimum process parameters, it may be possible to avoid such undesirable outcomes.

7.1 Total Heat Generated in Cutting Process

Surface burn and metallurgical damages on workpiece material due to high temperatures can be considered as a major drawback for abrasive machining. However; by using process models and obtaining optimum process parameters, it may be possible to avoid such undesirable outcomes. In this study, triangular heat flux model is used where abrasive wheel is represented as a 2D moving heat source along the surface and used to determine heat distribution over the workpiece as mentioned earlier.

The total heat generated during the operation is calculated as follows:

$$q_{total} = Q_{primary} + Q_{secondary} + Q_{workpiece-rubbing} \quad (41)$$

where $Q_{primary}$ and $Q_{secondary}$ are heat generated per unit depth in the primary and secondary shear zones, respectively. $Q_{workpiece-rubbing}$ is the contribution of the third deformation zone and investigated separately. The total heat generated during the operation is evacuated in four ways: through the chip (q_{ch}), grinding fluid (q_f), grinding wheel (q_{gw}) and the workpiece (q_w) as follows:

$$q_{total} = q_{ch} + q_f + q_{tool} + q_w \quad (42)$$

Since hundreds of interactions between abrasive grains and workpiece occur simultaneously along the contact length, some assumptions should be made in order to investigate the process better. As the geometrical properties of abrasive grains on the wheel differ, their chip formation mechanism, hence energy generation is not identical, either. Therefore, average geometrical properties that are obtained through optical measurements as presented in Section 3 are used. The total heat generated during the process can be calculated by Equation 42, however; q_w should be determined in order to investigate the surface burn or other metallurgical damages on the workpiece. Energy partition is a crucial factor for calculating process temperatures and can be defined as the fraction of the total energy transported as heat to the workpiece at the grinding zone. There are estimations for determining heat partition ratio into the workpiece [19], in this study; heat partition is calibrated through some initial experiments. Once it is identified; it can then be used for different cases involving the same workpiece and abrasive type however with different arrangements. Heat flux into the workpiece is q_{total} times the heat partition ratio (\mathcal{E}) [19].

$$q_w = q_{total} \mathcal{E} = q_{total} - q_{ch} - q_f - q_{tool} = \frac{F_t V_c}{l_c b} \mathcal{E} \quad (43)$$

7.2 Heat Generated in the Primary and Secondary Shear Zones

Heat generated in the primary shear zone is mainly due to plastic deformation. In the classical machining theory, the rate of heat generated is the product of the shear plane component, F_s , of the resultant force and shear velocity, V_s . The shear energy is almost completely converted into heat. Due to the complexity of the plastic deformation, contribution from the secondary shear zone to the heat generation is often ignored in the literature [48]. In this study, it is assumed that the process has orthogonal geometry and there is no inclination angle for the abrasive grains. Heat generated per unit depth in the primary and secondary zones are given as follows in the order [49];

$$Q_{primary} = F_s V_s = \frac{\tau h V_w \cos \alpha_n}{\sin \phi_n \cos(\phi_n - \alpha_n)} \quad (44)$$

$$Q_{secondary} = F_f V_c = \frac{\tau h V_w \sin \beta_n}{\cos(\phi_n + \beta_n - \alpha_n) \sin(\phi_n - \alpha_n)} \quad (45)$$

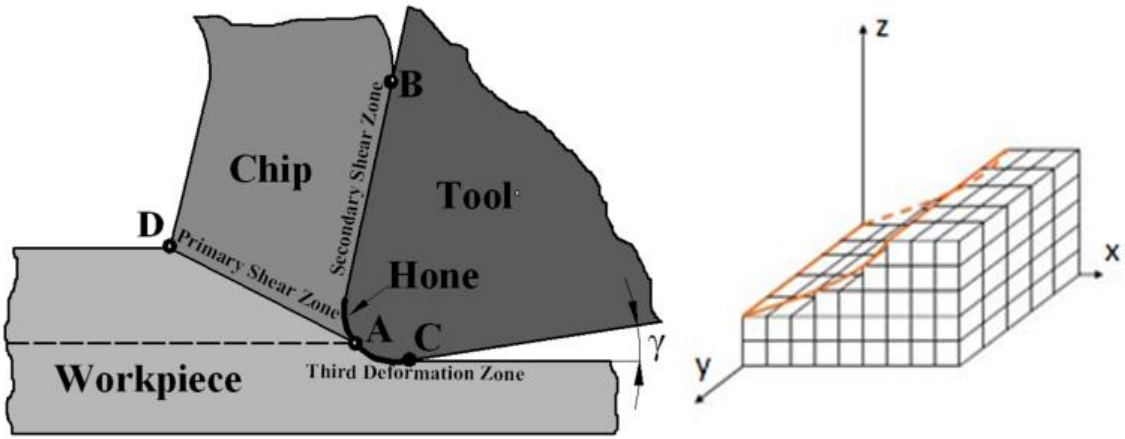


Figure 7.1: Orthogonal cutting schematic and Scanning the contact zone between wheel and workpiece

As it can be seen in Figure 7.1, the contact length is scanned and each abrasive grain's position, corresponding chip thickness and width of cut is calculated. Chip is investigated per unit depth of cut and the average temperature for each element due to shearing is obtained by Oxley's energy partition function [49].

$$\bar{\Delta T} = Q'_{primary} \frac{1 - \chi}{\rho c_c h V_w} \quad (46)$$

In this equation, ρ and c_c are the mass density and specific heat capacity of the chip, respectively. χ is the proportion of the shearing flux that goes into the workpiece material. It is defined by [49];

$$\begin{aligned} \chi &= 0.5 - 0.35 \log(R_t \tan \phi_n) & \text{for } 0.004 \leq R_t \tan \phi_n \leq 10 \\ \chi &= 0.3 - 0.15 \log(R_t \tan \phi_n) & \text{for } R_t \tan \phi_n \geq 10 \end{aligned} \quad (47)$$

R_t is the thermal number and defined as:

$$R_t = \frac{hV_w}{a_{diff}} \quad (48)$$

where:

$$a_{diff} = \frac{k_c}{\rho c_c} \quad (49)$$

Shear plane is assumed to have a zero thickness in this section and the average temperature rise on the shear plane is used as a boundary condition for the start point of the contact length (l_c). Primary and secondary zones are used as heat sources in solving the temperature distribution. They are calculated for all active abrasive grains and then integrated in order to obtain the total heat generation. Q_{chip} and q_{tool} are calculated via presented primary and secondary zone investigations and subtracted from q_{total} in order to determine q_w for dry grinding condition. If it is wet or MQL grinding conditions, q_f should be taken into account as well. q_f is estimated via calibration tests as explained in results and discussions section.

7.3 Heat Transferred into the Workpiece Material

Heat generated in the third deformation zone is due to the frictional rubbing phenomena between tool and workpiece. In Figure 7.1, between A and C points, tool and workpiece are in contact, however; there is no cutting action. As it is stated earlier, the third deformation zone forces (ploughing forces) are identified via linear regression analysis and subtracted from the total measured process forces in order to obtain the chip formation portion of them [50].

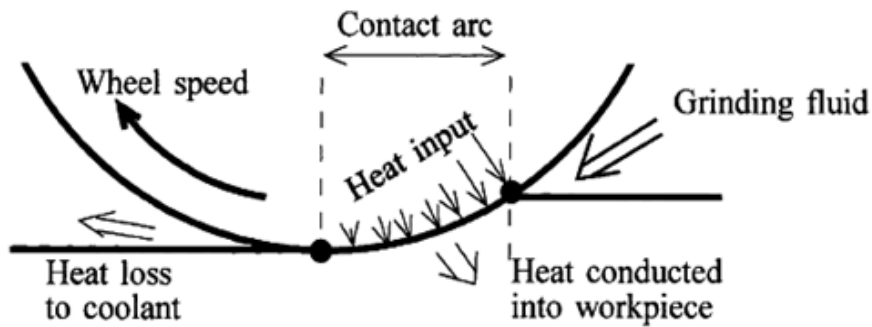


Figure 7.2: Contact length heat input to the workpiece material

Abrasive wheel is modeled as a moving heat source on workpiece which has a triangular shape. The 2D heat transfer governing equation is [49]:

$$\frac{\partial^2 T}{\partial x^2} + \frac{\partial^2 T}{\partial z^2} = \frac{1}{a_{diff}} \frac{\partial T}{\partial t} \quad (50)$$

In Figure 7.3, l_{chip} is the maximum chip thickness and θ_n is the nominal shear angle. φ is the angle between the triangular heat source's line of motion and the plane of the band source, as shown in Figure 7.3 [51]:

$$\varphi = \sin^{-1} \sqrt{\frac{a}{d}} \quad (51)$$

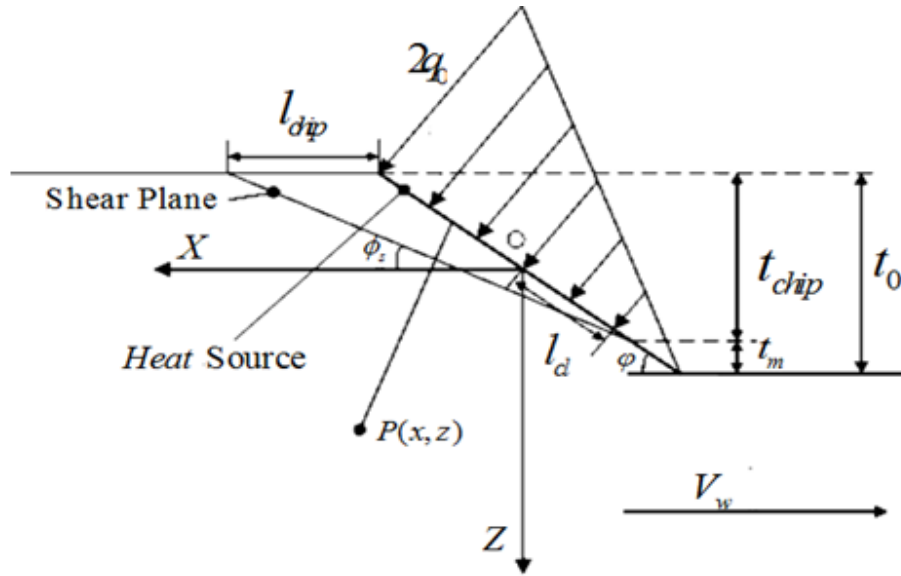


Figure 7.3: Contact zone between wheel and workpiece [51]

By considering Jaeger's moving heat source model, equation for the moving triangular band heat source is derived as [51]:

$$T(x, z) = \frac{R_w}{\pi k} \int_{-l_c/2}^{l_c/2} q_{lc} e^{-\frac{v_w(x+a \cos \varphi)}{2a_{diff}}} K_0 \left\{ \frac{v_w \left[(x+a \cos \varphi)^2 + (z-a \sin \varphi)^2 \right]^{1/2}}{2a_{diff}} \right\} da \quad (52)$$

where K_0 is the second kind modified Bessel function and R_w is the heat partition ratio to the workpiece.

7.4 Finite Difference Model for Temperature Distribution on Workpiece

In order to investigate the temperature distribution on workpiece, a finite difference model is implemented to the previously developed moving heat source model.

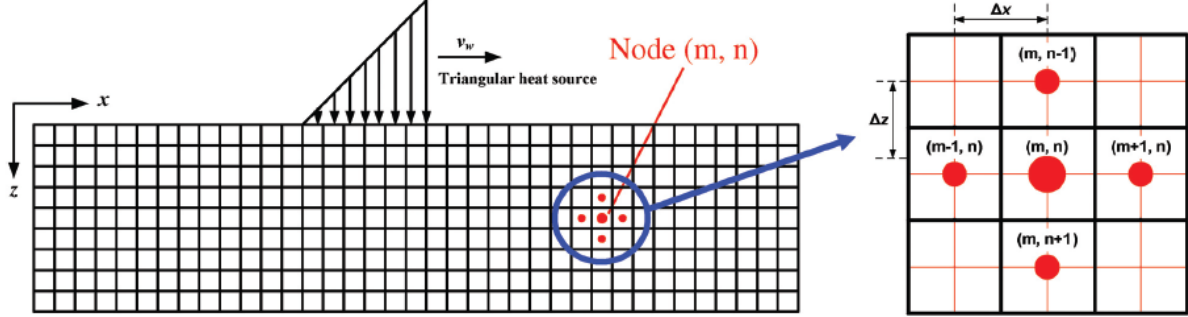


Figure 7.4: Triangular heat source and meshes on the workpiece [24]

Workpiece material is subdivided into small regions and each region is investigated in order. A uniform grid size is used and moving heat source is assumed to be triangular as in Section 6.3.

The corresponding equation is derived from 2D heat transfer equation (Eq. 50) as [24]:

$$\frac{T_{m+1,n}(t) + T_{m-1,n}(t) - 2T_{m,n}(t)}{(\Delta x)^2} + \frac{T_{m,n+1}(t) + T_{m,n-1}(t) - 2T_{m,n}(t)}{(\Delta z)^2} = \frac{1}{a} \frac{T_{m,n}(t + \Delta t) - T_{m,n}(t)}{\Delta t} \quad (53)$$

By using uniform mesh ($\Delta x = \Delta z$) assumption, Equation 53 can be rearranged as [24]:

$$T_{m,n}(t + \Delta t) = \frac{a\Delta t}{(\Delta x)^2} \left[T_{m-1,n}(t) + T_{m+1,n}(t) + T_{m,n-1}(t) + T_{m,n+1}(t) \right] + \left[1 - 4 \frac{a\Delta t}{(\Delta x)^2} \right] T_{m,n}(t) \quad (54)$$

Finite difference model is crucial in order to investigate the temperature distribution in Z direction since high temperature values cause thermal damages to the workpiece. Surface burn, metallurgical phase transformations and undesired residual tensile stresses are the major issues for abrasive machining.

These high temperature values cause thermal damages to the workpiece, such as surface burn, metallurgical phase transformations and undesired residual tensile stresses. Lack of convection heat transfer model is the major drawback of the presented temperature models in this study. There are studies that estimate the energy partition and the coefficient of convection heat transfer and multiply the heat transferred into the workpiece by that coefficient. This methodology may give correct temperature results; however, it does not provide insight about the convection phenomena.

7.5 Simulation of Grinding Temperature

Grinding temperatures are predicted via presented semi-analytical model and flowchart for the simulation procedure can be seen in Table 7.1.

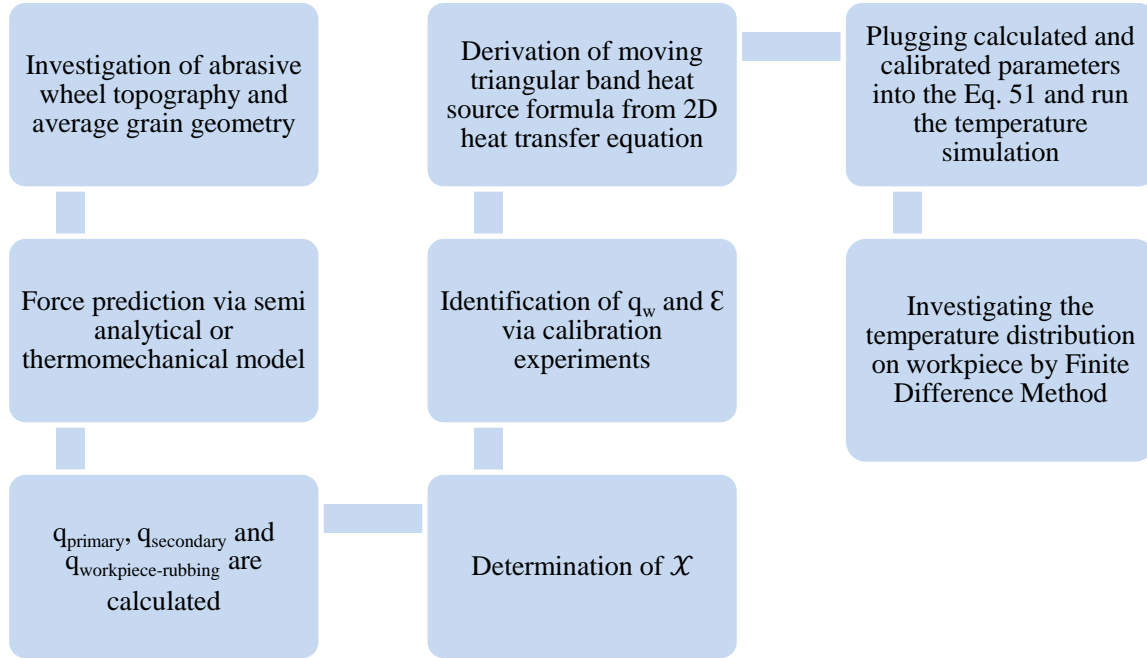


Table 7.1: Temperature simulation methodology

It is crucial to predict process forces correctly in order to be able to calculate the heat flux into the workpiece accurately. Once F_{tc} , F_{nc} and F_{rc} are calculated by force models, heat generated in the primary and secondary shear zones can be calculated by Equation 44 and 45. Proportion of the shearing flux (\mathcal{X}) that goes into the workpiece material is identified via Equation 47 and plugged into the Equation 46 to determine the heat generated due to shearing. Heat partition ratio (\mathcal{E}) that is identified via calibration tests are used to calculate the total heat flux into the workpiece. Equation for the moving triangular band heat source is derived from the classical 2D heat transfer equation and simulated via MATLAB in time domain.

Total power used for the primary shear zone and the third deformation zone are calculated by Eq. 43-44 and 51 and subtracted from total power to find secondary shear zone's power. Once the power for secondary shear zone is known, F_f , which is the frictional force between tool rake face and the chip contact zone, can be calculated. F_f values are presented in Table 7.2 and can be used to calculate temperature on the abrasive wheel in the future studies. Chip temperature is calculated via Eq. 45 which gives the average temperature rise of the chip due to shearing [Table 7.2]. In addition, contribution from secondary shear zone is considered as well by evaluating the energy input from frictional force between tool rake face and the chip

contact zone. Note that chip temperature rises with the axial depth of cut, which means more heat is removed from the contact zone by chips. That phenomenon is the main reason behind non-linear temperature behavior with the cutting parameters, increasing the feed rate and axial depth of cut does not make sure that the temperature on workpiece surface will be higher. It depends on the chip temperature which is going out from the contact zone and increasing l_c area (thus lower energy input per unit area) due to higher axial depth of cut or feed rate values.

7.6 Temperature Experiment Setup

It is a difficult task to measure process temperatures at the contact zone between abrasive wheel and the workpiece. Temperature experiments are conducted simultaneously with the force measurement experiments. In each operation, dynamometer is used to measure forces and a thermocouple embedded into the workpiece material is utilized to measure the temperature in the contact zone. K type thermocouple with a 0.8 mm diameter is used in the experiments. It is embedded into the workpiece with epoxy in a 1 mm diameter blind hole opened by EDM Drilling. The hole is blind because when the grinding wheel reaches the thermocouple, thermocouple smears with the workpiece which ensures full contact between them [25]. Temperature measurements are done via taking continuous data from the contact zone. For being able to measure or collect the data correctly, the data acquisition device should have sufficient sampling rate and measurement capability. As it is stated earlier, each active abrasive grain cluster is modeled as a milling tool tooth; therefore minimum time that takes one tooth to engage with workpiece and then leave is 0.17 seconds in our experiment set, maximum time is 0.38 seconds for 0.03 and 0.15 mm axial depth of cut, respectively. Hence, a data logging device which can take measurements with 0.1 second intervals is used.



Figure 7.5: Experiment setup during operation and the thermocouple junction with the w.p

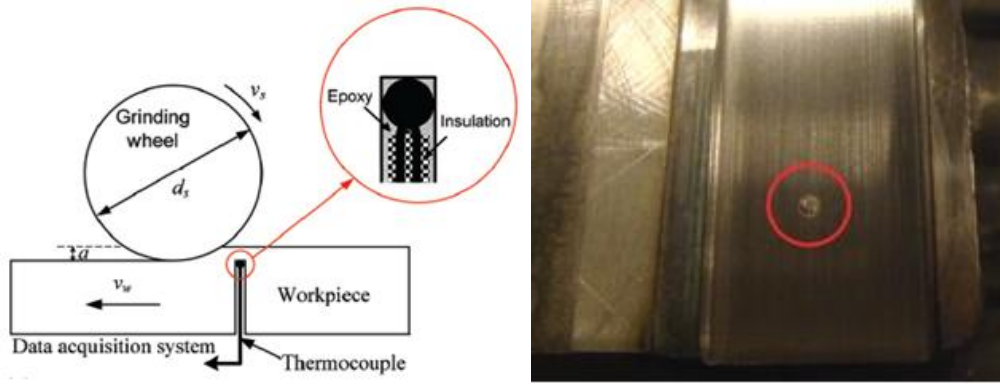


Figure 7.6: Thermocouple fixation diagram and exposed thermocouple junction after an operation

7.7 Contact Length Identification

No coolant is used in the experiments in order to avoid miscalculations when measuring process temperatures for real contact length. In order to obtain the real contact length between the abrasive wheel and workpiece, temperature at the cutting zone is measured by embedding a K type thermocouple into the workpiece as illustrated in Figure 7.6. Power (P), total heat transferred into the workpiece material through contact length (q_w) and total width of cut (b) can be calculated from process parameters and measured force and temperatures. Once they are calculated, real contact length is obtained as follows:

$$q_w = \frac{P}{l_{real} \times b} \quad (55)$$

Comparison between contact lengths calculated by thermocouple method and geometrical formulation are presented in Figure 7.7. It can be seen that the real contact length is considerably larger than the geometrical contact length due to the deflection of the wheel and grits under the action of the normal force. By this method, active grit number can be obtained more accurately which improves roughness, force and temperature predictions. Similar to the sliding coefficient analysis, a function for abrasive type and workpiece material is identified for real contact length parameter as well. This function is identified with same experiments for sliding friction investigation; hence no additional calibration experiments are necessary.

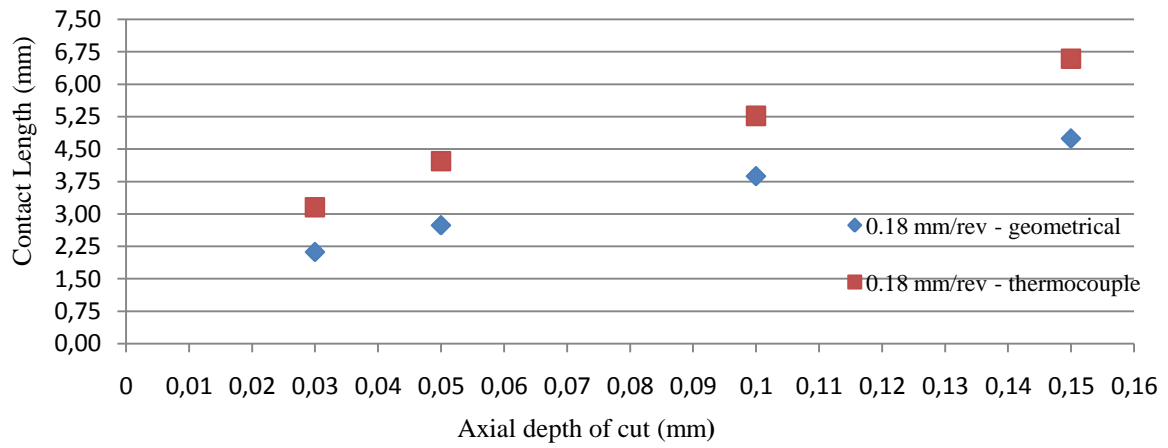


Figure 7.7: Comparison of contact lengths identified by geometrical formulation and thermocouple measurement ($feed_r = 0.18$ mm/rev)

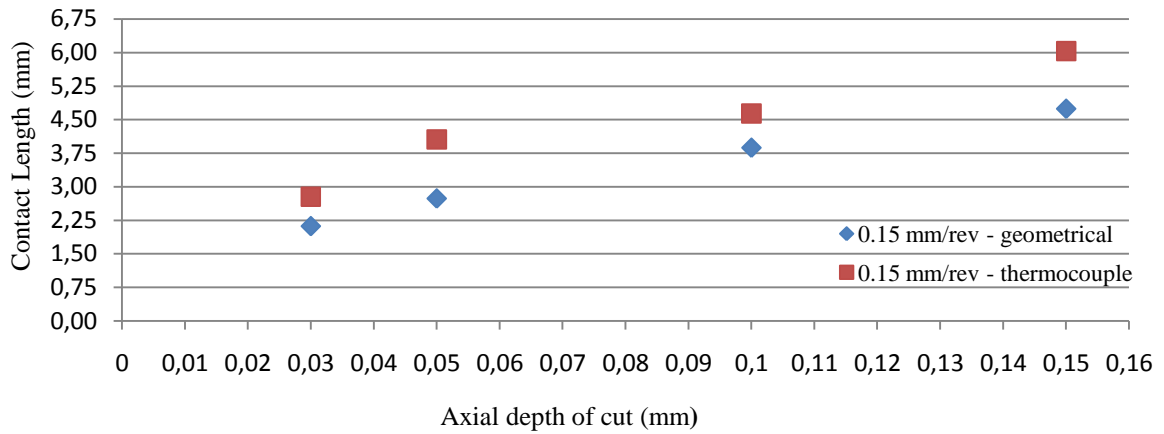


Figure 7.8: Comparison of contact lengths identified by geometrical formulation and thermocouple measurement ($feed_r = 0.15$ mm/rev)

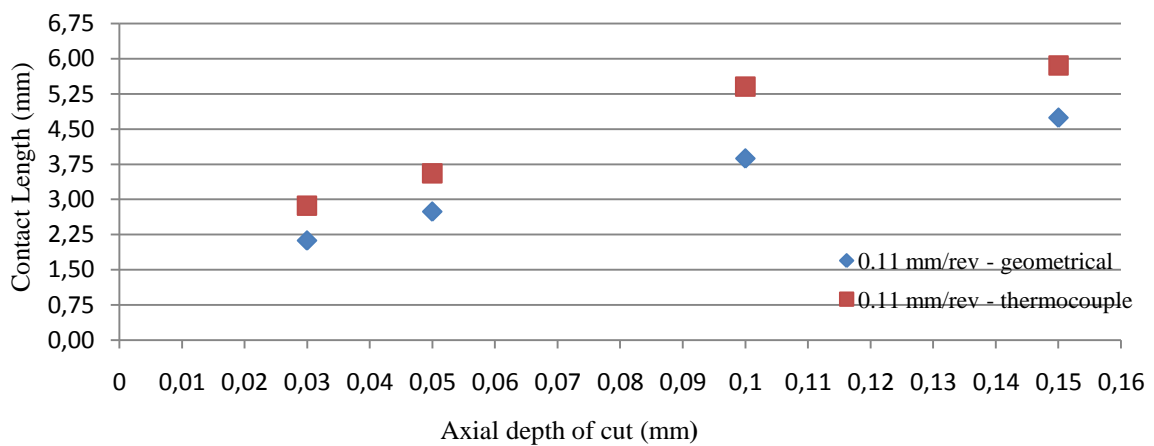


Figure 7.9: Comparison of contact lengths identified by geometrical formulation and thermocouple measurement ($feed_r = 0.11$ mm/rev)

7.8 Results for Measured and Calculated Temperatures

Measured and simulated maximum (peak) temperatures for dry, wet and MQL cases are presented in Table 7.2. Friction coefficient (μ) is identified via Merchant's theory [46] for each operation. Note that μ is smallest in MQL cases which is the main advantage of using minimum quantity lubrication. Average μ values are 0.62, 0.55, 0.45 and heat partition values are 72.27%, 25.11% and 61.52% for dry, wet and MQL cases, respectively. In Figure 7.13 and Figure 7.14; 0.18 mm/rev feed and 0.15 mm axial depth of cut case results for dry and wet conditions are presented respectively. Since temperatures for MQL case are quite similar to those in dry operations, they are not illustrated.

Test No.	feed (mm/rev)	a (mm)	Temperature (°C) Dry			Temperature (°C) Wet			Temperature (°C) MQL		
			Experiment	Simulation	μ	Experiment	Simulation	μ	Experiment	Simulation	μ
1	0,06	0,03	610,5	671,40	0,62	197,5	217,20	0,52	481,51	573,67	0,43
2	0,06	0,06	693,70	743,00	0,60	256,25	240,36	0,55	547,13	634,85	0,45
3	0,06	0,1	785,16	874,10	0,69	309,30	282,78	0,53	619,27	746,87	0,43
4	0,06	0,15	1051,92	1159,00	0,66	322	374,94	0,53	829,67	990,30	0,44
5	0,11	0,03	510,15	571,50	0,57	147,60	184,88	0,60	402,36	488,32	0,48
6	0,11	0,06	623,16	706,40	0,62	227,70	228,52	0,58	491,50	603,58	0,47
7	0,11	0,1	897,20	1009,00	0,67	289,98	364,42	0,58	707,64	862,13	0,47
8	0,11	0,15	964,88	1058,00	0,70	281,60	342,27	0,59	761,02	904,00	0,48
9	0,18	0,03	495,50	586,60	0,53	160,80	189,77	0,51	390,81	501,22	0,42
10	0,18	0,06	605,20	690,40	0,58	270,60	223,35	0,51	477,33	589,91	0,43
11	0,18	0,1	732,20	820,40	0,59	292,50	265,40	0,55	577,50	700,99	0,45
12	0,18	0,15	854,80	921,00	0,58	360,40	330,30	0,56	674,20	872,39	0,46

Table 7.2: Temperature and μ results

For wet grinding, the water based Boron Oil coolant at 4 vol. % with flow rate 2000 ml/min, for the MQL grinding, MQL is used with 5 ml/min flow rate. Surface burn is detected in 3, 4, 7, 8 and 12th operations given in Table 7.2. When process temperature exceeds the burn threshold and burning of the workpiece is initiated, metallic particle adhesion in the abrasive grains of the wheel increases, having as consequence the increase of the grinding forces. In this study, both force monitoring and visual inspection are used to detect surface burn and burn threshold results agree with the literature. Wojtas et al. [52] claimed that burn threshold for AISI 1050 steel is identified as 750°C by using the Magnetic Barkhausen Method. Experiments show that temperature and force measurements fairly agree with the 750°C threshold value. Forces increase as burning of the workpiece is initiated which corresponds to temperatures above 720-750°C. In Figure 7.10, measured forces are illustrated for 12th (burn) and 5th (burn-free) operations [see Table 7.2] respectively.

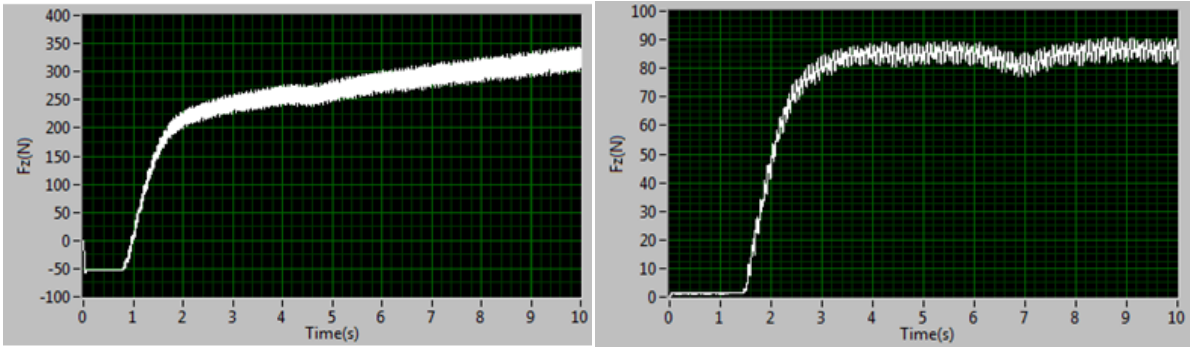


Figure 7.10: Forces for 12th and 5th operations

As it can be seen from the Figure 7.10, forces have increasing trend in burn-observed operations whereas they are almost constant for burn-free cases. This behavior is always observed for burn and burn-free operations throughout the experiments. Visual inspection of the final workpiece surface also agrees with the force measurements and determined burn threshold.



Figure 7.11: Workpiece surface inspection



Figure 7.12: Surface 3(Figure 7.11) observed operation

In Figure 7.11, 2nd and 1st surfaces are results for coolant used cut with 0.1 mm axial depth of cut & 0.11 mm/rev feed parameters and dry case with same parameters, respectively. 3rd surface is the result of 0.15 mm axial depth of cut with 0.11 mm/rev feed without coolant and 4th surface is for coolant used case with same parameters.

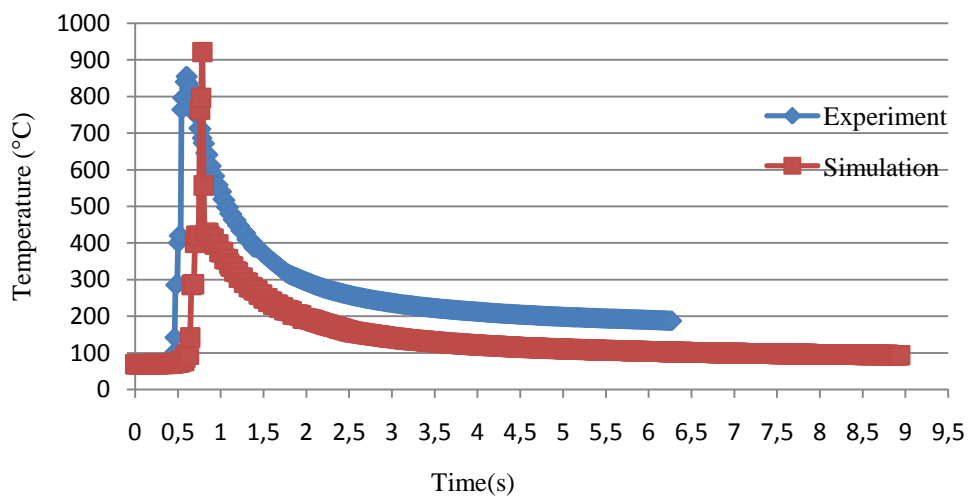


Figure 7.13: Experiment and simulation result for test 12 (dry)

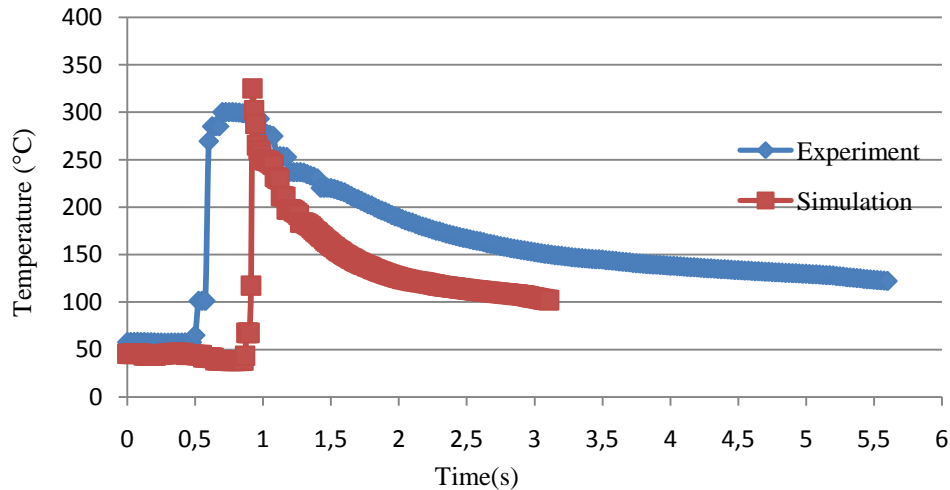


Figure 7.14: Experiment and simulation result for test 12 (wet)

Test No.	feed (mm/rev)	Axial depth(mm)	Q_primary (W)	Q_secondary (W)	Total Power (W)	F _f (N)	Chip Temperature (°C)
1	0,06	0,03	674,64	330,67	1005,31	26,31	164,15
2	0,06	0,06	626,36	630,28	1256,64	50,16	206,13
3	0,06	0,1	579,57	928,39	1507,96	73,88	241,96
4	0,06	0,15	692,69	1443,60	2136,28	114,88	347,41
5	0,11	0,03	792,14	276,00	1068,14	21,96	105,49
6	0,11	0,06	889,79	681,00	1570,80	54,19	153,60
7	0,11	0,1	798,69	960,60	1759,29	76,44	170,20
8	0,11	0,15	757,43	1504,52	2261,95	119,73	218,35
9	0,18	0,03	1912,74	223,54	2136,28	17,79	143,89
10	0,18	0,06	1706,28	681,33	2387,61	54,22	159,51
11	0,18	0,1	1824,03	940,57	2764,60	74,85	184,33
12	0,18	0,15	1908,43	1484,49	3392,92	118,13	226,62

Table 7.3: Chip temperature and Frictional force calculation between tool & chip

Chip temperatures are not validated by measuring chip temperatures. It is impossible to measure removed chip temperature by thermocouples. A thermal camera can be utilized for this task and for the verification of the calculated chip temperatures. Calculated values show that chip temperature increases with the uncut chip thickness which means temperature that is removed from the contact zone by chips increases.

It has been observed that there is a non-linear temperature behavior with the cutting parameters, increasing the feed rate and axial depth of cut does not make sure that the temperature on workpiece surface will be higher. One would expect a direct increase in temperature with axial depth of cut; however, as depth of cut increases, both the portion that is removed by chips and contact area between workpiece and the wheel increases which lowers the process temperature. Forces and power increases with axial depth of cut, therefore temperature increases.

Same logic is valid for feed rate, since uncut chip thickness increase with the feed rate for a constant cutting speed, a linear relationship between process temperature and feed rate can be expected. However, similar to axial depth of cut, temperature does not directly increase with feed rate. As feed rate increases, triangular shaped moving heat source travels faster along the workpiece surface and spends less time on each point, but with more heat energy. Both of these relationships should be considered for temperature predictions.

For radial depth of cut case; in abrasive machining, it is usually selected as the width of the grinding wheel. As radial depth of cut increases, forces and process power will increase, and also the contact zone between abrasive wheel and workpiece material.

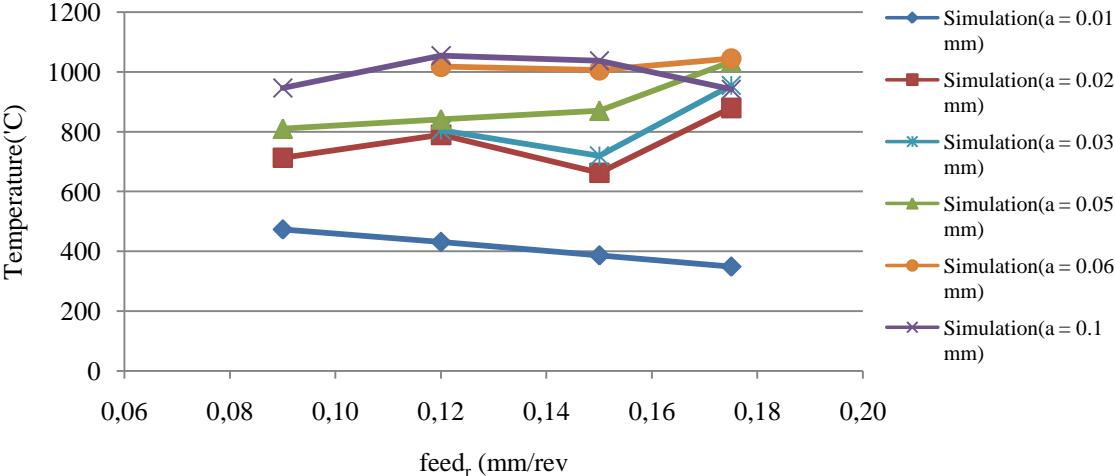


Figure 7.15: Simulation results for different process parameters

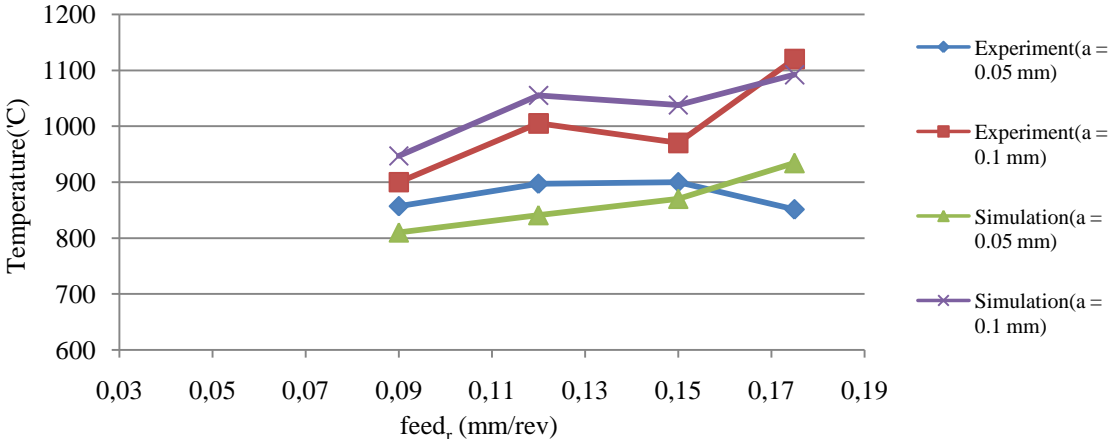


Figure 7.16: Measured and predicted temperatures

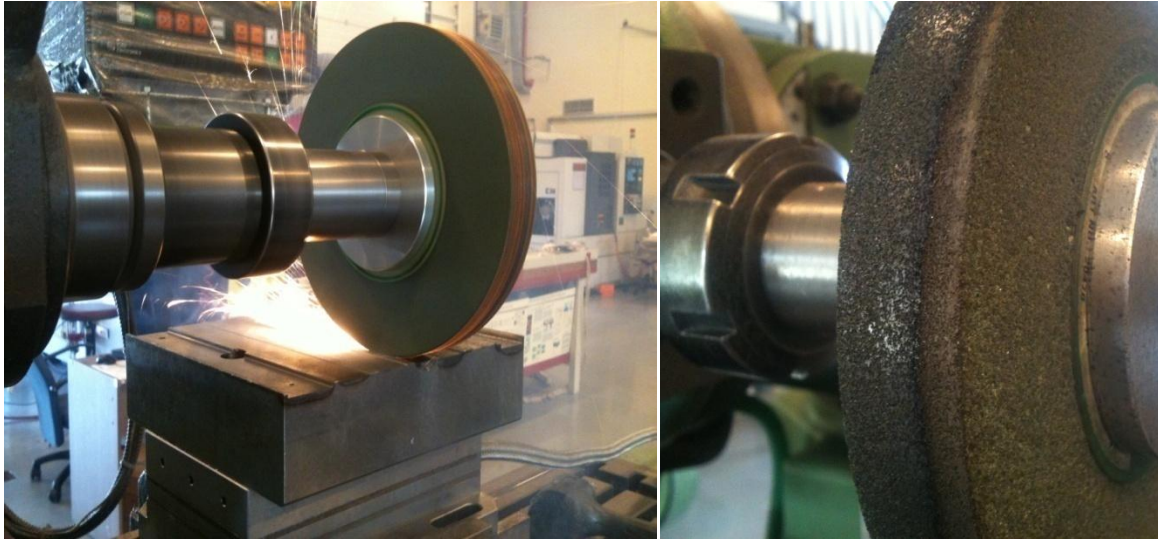


Figure 7.17: Surface burn observed operation and wheel condition afterwards

In Figure 7.17, material that is stuck to the abrasive wheel due to the high temperatures can be seen. In this study, wheel is dressed with same parameters after each operation. Workpiece temperature is checked before each operation in order to monitor whether it cooled down to the room temperature or not. Since temperature may reach up to 1000 celcius degrees, it took almost one hour for some cases. It was checked that the workpiece temperature is equal to the room temperature and the wheel is dressed properly with the same conditions before each operation. In addition, since K type thermocouple is grinded for temperature measurements, embedding another thermocouple in a blind hole and constantly opening new blind holes by EDM requires a serious effort. These are the reasons behind low number of temperature experiments. By optimizing these conditions and developing smart solutions to the thermocouple fixation, EDM, dressing or waiting time issues, required time for the temperature measurements can be reduced.

8 An Initial Approach to the Dynamic Modeling of the Grinding Processes

In this section, an initial approach is proposed in order to model and investigate dynamics of the grinding process. An analogy between grinding and milling processes is introduced in the sense of cutting grit or teeth number for stability analysis. Simulations are in a good agreement with experimental results. There are few studies in the literature related to dynamic properties of the grinding processes. Due to non-linear and stochastic nature of the process, being able to model the dynamic behavior of the abrasive wheel is a difficult task.

Grinding chatter is usually ignored in the industry since it is generally used for finishing operations where axial depths are selected below 40-50 μm . However, abrasive machining is

started to be used widely for machining of the difficult-to-cut materials and not only for finishing purposes, but also for roughing and slotting operations. It may seem that observing chatter marks on a grinded surface is an unlikely event. On the contrary, especially for roughing operations chatter vibrations may occur and even there are chatter marks on the surface, but they are often not visible to a human eye. These marks decrease the performance of the final product considering that they increase the surface roughness.

Throughout the entire study, micro-milling analogy for the grinding operations is used by assuming that each abrasive grain acts like a milling cutter tooth. In order to model the dynamic behavior of these grains, force coefficients, the relationship between the forces and the uncut chip thickness, must be known as will be discussed. Dynamic chip thickness and cutting forces should be modeled as a first step. An eigenvalue problem consisted of multi-dimensional dynamic equations should be solved to obtain the stability limits.

Since micro-milling analogy is used to model the dynamic behavior of the grinding process, a comprehensive literature review has been done. The mechanics of instability in machining processes was first studied by Tlustý [53] and Tobias [54]. They claimed that the modulated chip thickness due to the process vibrations increases the vibration amplitudes which cause a process called regenerative chatter. They also observed that the axial depth of cut was the key process parameter for this event. Tlustý [53] showed that if the axial depth of cut exceeds the stability limit, an unstable cutting process will occur. He used an approximate 1D solution for analytical modeling of the dynamic behavior of the process which is not enough to handle milling process where 2D or multi-D solutions should be utilized. Later, Budak and Altintas [55] analyzed the milling stability by calculating the dynamic chip area with a cross coupling term including the effect of vibrations in one direction on the chip area in the other direction. Models that come after generally use Budak and Altintas's [55] approach by some modifications to apply the theory to different machining processes. Same procedure is followed in this study as well. Model proposed in Budak and Altintas is applied to each abrasive grain; however, due to the stochastic nature of the abrasive wheel and random distribution of grains, it is almost impossible to define the delay between adjacent grains exactly. Some assumptions can be used which is not adequate for such a sensitive analysis. That is the reason for calling this section as an initial approach to the dynamic modeling of the grinding processes. It should be considerably improved to model the process dynamics properly.

8.1 Single Tooth Approach for Abrasive Wheel

Abrasive wheel can be modeled as a milling tool with a one cutter tooth. Chatter mark on the workpiece surface remained from the previous revolution of the abrasive wheel will be met by the wheel in the upcoming revolution.

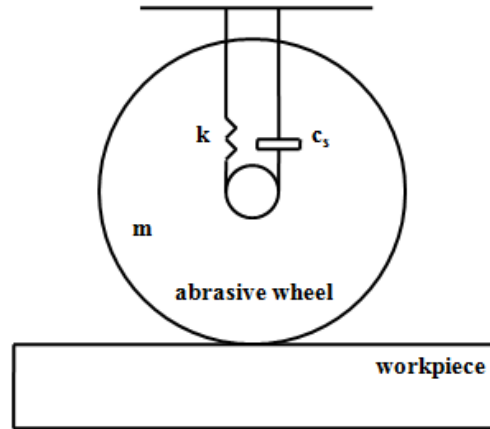


Figure 8.1: Abrasive wheel 1DOF

Theory and approach in this part is retrieved from Yang, Lin and Xu [56]. The equation of the motion for single tooth grinding wheel is:

$$my''(t) + cy'(t) + ky(t) = F(t) \quad (56)$$

where m is the mass (Kg), c is the damping ratio (Ns/mm) and k is the stiffness (N/mm) of the machine vibration system. Dynamic grinding force due to dynamic chip thickness for a single tooth can be written as:

$$F(t) = k_m ba(S_0 - [\mu y(x-T) - y(t)]) \quad (57)$$

K_m is the coefficient of force defined as N/mm^3 , b is the radial depth of cut, a is the axial depth of cut and $S(t)$ is the surface chatter mark of the workpiece. $Y(x-T)$ refers to grinding vibration displacement of the last time and $y(t)$ is the displacement of the current time. Natural frequency (w_n) and the damping ratio of the system (c_s) is:

$$w_n = \sqrt{\frac{k}{m}} \quad (58)$$

$$c_s = \frac{c}{2mw_n} \quad (59)$$

Plugging these into Equation 57:

$$y''(t) + 2c_s w_n y'(t) + w_n^2 y(t) = \frac{F(t)}{m} \quad (60)$$

By applying Laplace transformation to the Equation 60 and rewrite the equation in the transfer function form:

$$G(s) = \frac{y(s)}{F(s)} = \frac{1}{k} \frac{1}{k\left(\frac{s}{w_n}\right)^2 + 2c_s \frac{s}{w_n} + 1} \quad (61)$$

If the root “s” in the transfer function is defined as $s = \delta + i\omega$, system is critically stable if the $\delta = 0$. If it is larger than zero, system is unstable and if it is lower, system is stable. In order to determine the threshold between stable and unstable regions, δ is set to zero and plugged into the equations.

$$G(i\omega) = \frac{y(i\omega)}{F(i\omega)} = \frac{1}{k} \frac{1}{k\left(\frac{i\omega}{w_n}\right)^2 + 2c_s \frac{i\omega}{w_n} + 1} \quad (62)$$

$$F(t) = \Delta F e^{i\omega t} \quad (63)$$

$$y(t) = G(i\omega) \Delta F e^{i\omega t} \quad (64)$$

$$y(t-T) = e^{-i\omega T} G(i\omega) \Delta F e^{i\omega t}$$

By mathematical manipulations, both N (rpm) and a_{lim} which are spindle speed and critical axial depth of cut respectively can be derived from these equations. By [55] and scanning the $1.05w_n - 1.5w_n$ frequency range for each lobe, stability diagram can be obtained.

8.2 Multi Teeth Approach for Abrasive Wheel

For the multi teeth approach, abrasive wheel is modeled as a milling tool with multiple teeth and the theory of Budak and Altintas [55] is used with slight modifications. Budak and Altintas modeled the milling cutter as a multi degree-of-freedom structure and considered the dynamic interaction along the axial depth of cut in the formulation. They used a stability analysis which is based on the physics of the dynamic milling and predict the stability limit by deriving a relationship between the chatter frequency and the spindle speed for the first time.

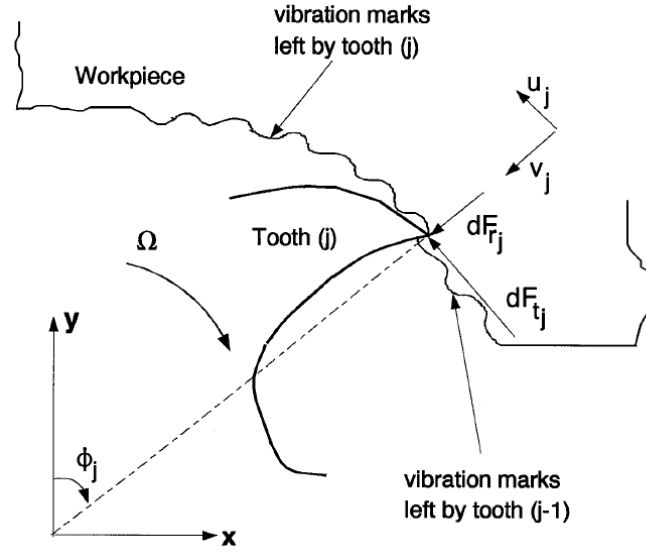


Figure 8.2: Dynamic milling process

In Figure 8.2, tooth is the cluster of abrasive grains that form a single tooth on abrasive wheel. Dynamic regenerative chip thickness and differential-total dynamic milling forces can be found in Budak and Altintas [55] and Budak's PhD thesis [38]. Workpiece is assumed as a rigid body and dynamical properties of the work material are neglected. Zero order approximation is used and cutter displacement is determined by considering only vibrations at the chatter frequency (w_c). Budak [38] derived the limiting axial depth of cut formula as:

$$a_{lim} = -\frac{2\pi \wedge_R}{NK_t} (1 + \kappa^2) \quad (65)$$

where:

$$\kappa = \frac{\wedge_{Im}}{\wedge_{Re}} = \frac{\sin w_c T}{1 - \cos w_c T} \quad (66)$$

$$T = \frac{1}{\omega_c} (\varepsilon + 2k\pi) \quad (67)$$

T is the tooth passing period and K is the ratio of imaginary and real parts of the transfer function. N is the teeth number and K_r is the previously identified cutting coefficient. Corresponding spindle (n) speed for a limiting axial depth of cut is:

$$n = \frac{60}{NT} \quad (68)$$

$$\begin{aligned} \varepsilon &= \pi - 2\psi \\ \psi &= \tan^{-1} \kappa \end{aligned} \quad (69)$$

In Equation 67, k is the lobe number and the stability lobes are calculated as follows [38]:

- select a chatter frequency from transfer functions around a dominant mode
- calculate the critical depth of cut and corresponding spindle speed for each stability lobe ($k = 0, 1, 2, 3, \dots$)
- scanning the $1.05w_n - 1.5w_n$ frequency range for each lobe and draw the stability diagram

8.3 Abrasive Wheel - Milling Cutter Tool Analogy

Wheel topography is scanned as described in Section 3 and distance between adjacent grains is carefully investigated. If the distance between grains are below $500 \mu\text{m}$ [57], these grains are assigned to the same cluster, ie. same tooth. If a cluster of grains do not have any neighbor closer from $500 \mu\text{m}$, a new cluster-tooth is defined. A sample from consecutive grain scans are given in Figure 8.3.

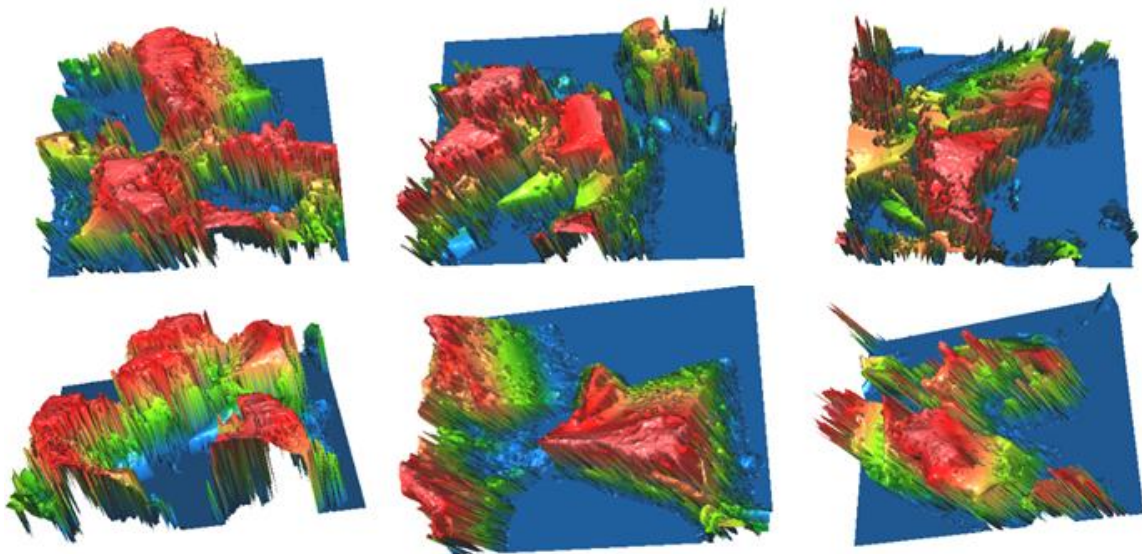


Figure 8.3: Scanned grains for cluster (tooth) identification

The cutter tooth identification on abrasive wheel is a time consuming task. Half of the abrasive wheel is investigated in this study. 17 abrasive grain clusters are identified for a half wheel which results for a 34 cutting teeth in total. Theory and formulation are applied for a milling cutter tool with 34 teeth which represents the SiC 80 M abrasive wheel with the dressing conditions given in Table 4.2 (pg. 34). Alumina 60 M wheel scans resulted with 43 cutter teeth. Since 500 μm is used as a cut-off distance for introducing a new tooth, 34 teeth are placed with 10.5 degree increments in circumferential direction of the wheel. Therefore it can be considered as a milling tool with 34 teeth which has a 10.5 degree pitch angle between them and stability diagram is obtained for identified milling tool which represents the abrasive wheel. A true representation of the abrasive wheel should include exact positions of grains and delay among them. Dynamic chip thickness per each grain can be determined by that approach and used in the stability diagram calculations which will represent the true nature of regenerative chatter vibrations.

8.4 Identification of the Abrasive Wheel Modal Parameters

Impact test is used to identify the modal parameters of the abrasive wheel which are required to construct stability diagram.

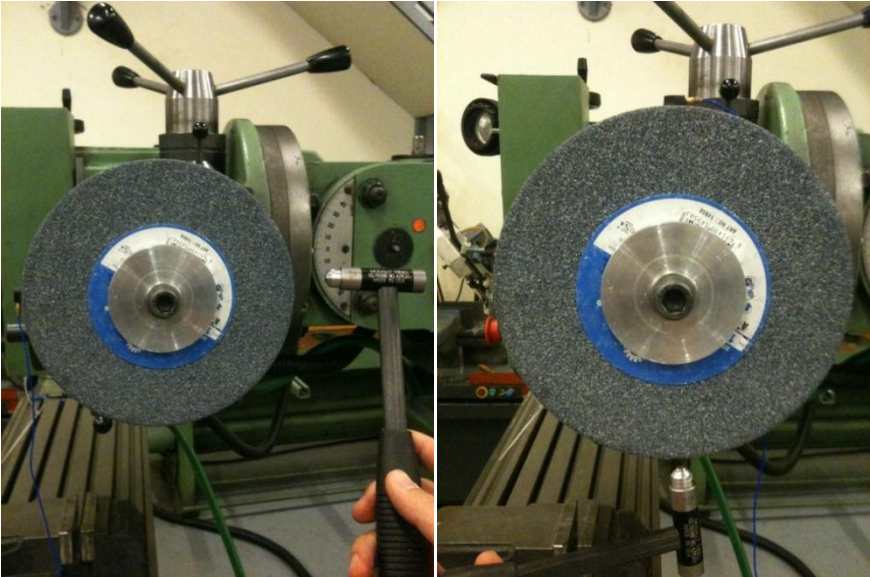


Figure 8.4: FRF measurement of the abrasive wheel (X and Z directions, respectively)

Identified modal parameters are:

Mode	Frequency(Hz)	Damping Ratio(%)	Modal Stiffness (N/mm)
X	309,17	3.9	6334287
Y	298,3	5.2	7552955

Figure 8.5: Modal parameters for the wheel illustrated in (Figure 8.4)



Figure 8.6: Modal parameters of the spindle and tool holder

Once the modal parameters of the abrasive wheel in X and Z direction are identified, corresponding stability diagram is plotted via simulation code.

8.5 Stability Diagram and Experiment Results

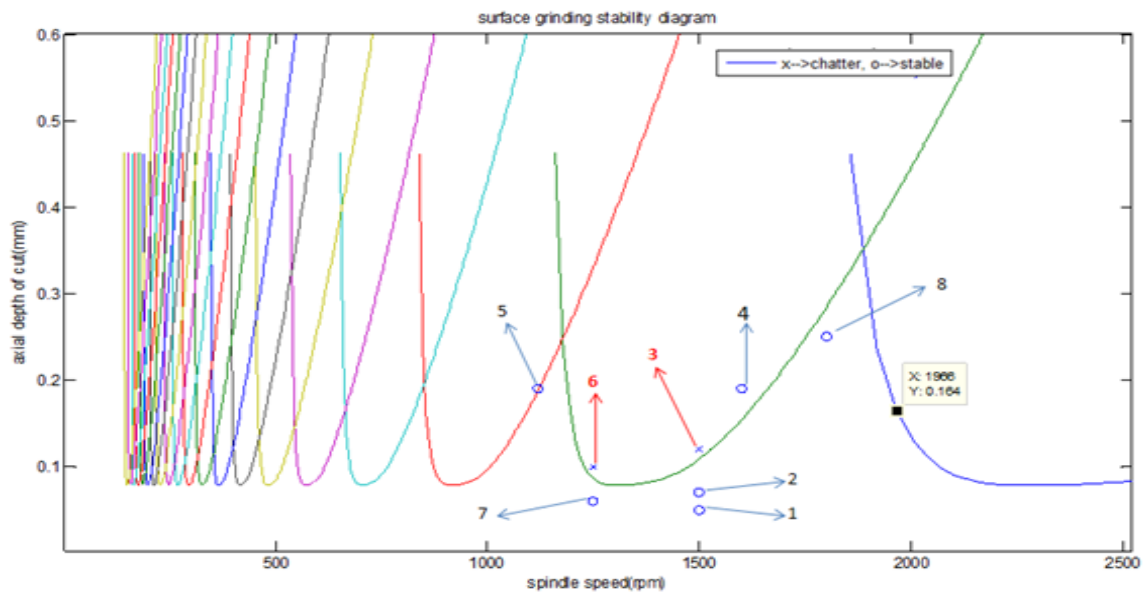


Figure 8.7: Stability diagram and sample experiments

#	b(mm)	a(mm)	feed _r (mm/rev)	rpm	Experiment(N) - max		Surface Roughness (R _a)	
					Fx	Fz	X direction	Y direction
1	23,5	0,05	0,08	1500	50	85	0,32	0,22
2	23,5	0,07	0,08	1500	40	80	0,35	0,2
3	23,5	0,12	0,08	1500	140	230	0,41	0,91
4	23,5	0,19	0,08	1600	125	250	0,10	0,41
5	23,5	0,19	0,08	1120	270	650	0,34	0,42
6	23,5	0,1	0,08	1250	80	170	0,10	0,8
7	23,5	0,06	0,08	1250	65	140	0,09	0,3

8	23,5	0,25	0,08	1800	240	720	0,18	0,26
---	------	------	------	------	-----	-----	------	------

Figure 8.8: Experiments for stability diagram validation

Chatter vibrations are observed for operations 3 and 6. They lie in the unstable region as it can be seen from the stability diagram, Figure 8.8.

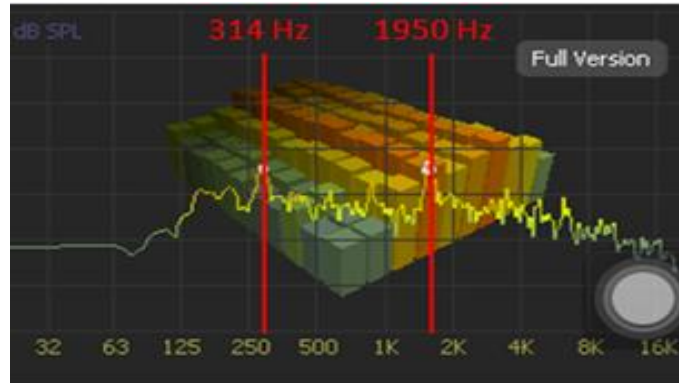


Figure 8.9: Sound measurement from operation 6

While in condition of stable cut, dominant frequencies are spindle speed and tooth passing frequencies. When instability is reached, some other frequencies appear. The detection of peak at frequency different from tooth passing or spindle speed frequency is a way to detect chatter. There will be peak in the sound pressure at a frequency close to the abrasive wheel's natural frequency. Sound is recorded for each operation and for the chatter vibration observed operations, a peak value close to the abrasive wheel's natural frequency is observed as presented in Figure 8.9.

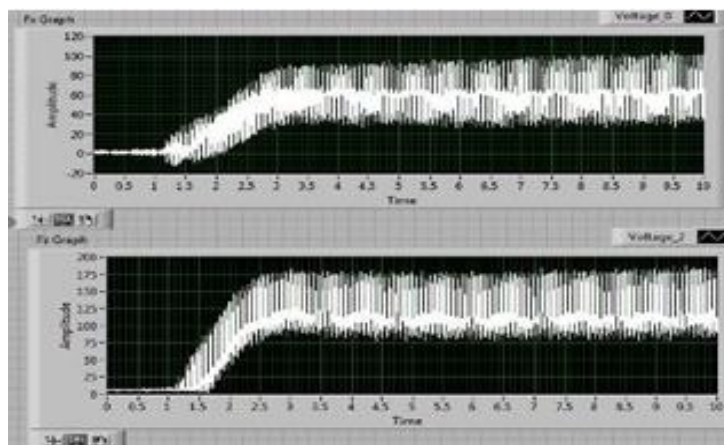


Figure 8.10: Measured force for operation 6

9 Suggestions for Further Research

Following are the recommended studies for extending the capabilities of the models presented in this study:

- A comprehensive formulation for determination of the abrasive wheel topography and geometric properties of the abrasive grains can be developed. That would reduce the amount of time and effort to identify these parameters for each wheel.
- For surface roughness analysis, abrasive wheel vibration and the third deformation zone effect can be modeled for more accurate and realistic predictions.
- Modeling the dressing operation or prediction of the dresser tool wear is necessary for better simulation of the groove geometry on the circumferentially grooved wheels.
- An analytical investigation for ploughing forces can be developed as a future work for presented force models.
- A special lens can be utilized to observe stick-slide regions on abrasive grain rake face. It is believed that a 100x lens would be appropriate for this task.
- A semi-analytical or analytical model for real contact length identification between abrasive wheel and workpiece material would be more practical and reliable.
- Thermal damages on the workpiece, especially in Z direction (residual stresses, thermal cracks) should be further investigated by considering material properties of the workpiece.
- Chemical reactions between abrasive wheel and workpiece material due to high process temperatures can be investigated. Diffusion between two bodies and amount workpiece material that is stuck to the abrasive wheel can be predicted. Determination of the time when abrasive wheel needs to be dressed would be possible by such analyses.

- Dynamic model should be further developed by considering the non-linear behavior of the process and determination of the abrasive grain location and distribution on the wheel. That is necessary to define a certain time delay between adjacent abrasive grains which is crucial for dynamic investigations.

10 Discussions and Conclusions

In this thesis, semi-analytical and thermomechanical models that represent the mechanical, thermal and dynamical behavior of grinding processes are presented. The proposed models are verified through experiments. Identification of force and thermal coefficients, modal parameters through calibration experiments or impact tests are proposed. Procedure for abrasive wheel topography simulation is carried out by introducing the abrasive grain scanning method. Uncut chip thickness is calculated for each grain and used for force, thermal and dynamic models. It is shown that the presented models can be used to simulate the grinding operations with accurate predictions. Presented semi-analytical and analytical models provide faster solution times compared to the finite element methods presented in the literature [27,30,51]. Specific contributions of the presented study are listed as follows:

- Micro-milling analogy for grinding operations is developed by defining geometrical properties of each abrasive grain. Rake angle, width, height and edge radius are identified by optical scanning method. Oblique angle for grain is also defined which provide an improvement with respect to previous grinding models.
- It is demonstrated that the Gaussian distribution for grain geometrical properties is an adequate approach for wheel topography simulation. Rather than using a single average value for these geometrical parameters, a Gaussian distribution is constructed by identifying the mean and standard deviation. Random values from these distributions are assigned to abrasive grains which are rake, oblique angle, edge radius, width and height. Presented approach gives better prediction ability than assigning a single average value for each of these parameters.
- The wheel topography is simulated by using identified Gaussian distributions for the grain geometrical parameters. Simulation of flat regions of the wheel was reported before in the previous studies [6,16,51]. However, groove topography simulation is performed in this study as an expansion in order to model the operations that are performed with grooved wheels.
- Chip thickness calculation method is compared with the average thickness formulations presented in the literature and it is noted that the uncut chip thickness

calculation for each active abrasive grain provides more accurate surface profile, force and temperature predictions.

- Once these topographical analyses are done carefully for a regular wheel with a certain abrasive type, it is possible to predict process outcomes for all variations of wheel geometries (ie. radial or circumferentially grooved, segmental etc.) which is a noteworthy contribution as it reduces the number of required calibration experiments.
- Forces per grit are identified by both semi-analytical and thermomechanical force models which provides more insight about the chip formation mechanism considering the ability to calculate fundamental parameters such as shear stress, shear angle and friction coefficient in the grain scale. In addition, dual-zone contact analyses in secondary shear zone and calculation of chip temperature are results of grit based analyses.
- Easy implementation of the semi-analytical force model can be considered as a major advantage. Considering grinding as a milling operation with multiple cutting teeth is not commonly used in the literature. Using milling force equations with some modifications and obtaining reasonable results showed that this model can be expanded by using similar chip formation mechanism for abrasive machining operations.
- The material behavior and friction behavior during grinding process is quantified and thermomechanical approach with dual-zone contact analysis for grinding operations is utilized for the first time in the literature. A novel thermo-mechanical model at primary shear zone with sticking and sliding contact zones on the rake face of the abrasive grit was established. By utilizing thermo-mechanical analyses and Johnson-Cook material model, a few calibration tests for an abrasive type-workpiece pair is sufficient to predict process forces for different cases involving the same workpiece and the abrasive material however with different arrangements and process parameters.
- Thermomechanical model of oblique cutting presented by Ozlu et al. [45] is modified for grinding operations which accounts for the chip formation in the primary shear zone and includes dual-zone model of Zorev [34] to represent the contact at the grit-

chip interface. As chip meets with the grit, shear stress is identical to the shear flow stress of the work material and starts sticking on the grit's rake face. Further away from the grit tip, the chip starts to slide along the rake face as the stress reduces where contact is governed by a Coulomb friction law.

- The sliding friction coefficients for SiC 80 M and Alumina 60 M wheels with AISI 1050 steel are identified which can be used for further studies. These coefficients can be used for SiC and Alumina abrasive materials with AISI 1050 steel. The main parameter affects the sliding friction coefficient is observed to be the friction speed.
- Force in the third direction (radial) can be predicted by oblique angle and grain location (especially on groove walls) analyses which is neglected in the literature. For the circumferentially grooved wheels, radial force becomes more crucial since grooves introduce a helix angle for the abrasive wheel.
- Surface roughness and profile can be predicted for regular and circumferentially grooved wheels via kinematic analysis. Surface profile simulation for grooved wheels is believed to provide an improvement with respect to previous surface roughness models which investigated grooved wheels experimentally.
- Since oblique cutting theory is used for abrasive grains, grain tip is divided into regions in order to investigate the local angles. If there is a radius at the tool or grit tip, feed, tangential and radial force directions change along the radius and should be investigated locally. It is believed that this approach improves the accuracy of the presented models.
- Triangular moving heat source theory is used to predict the process temperatures for grinding operations. Energy transferred into the workpiece material per grit is calculated and integrated over total number of active grains in the contact region which is believed to increase the accuracy of previous thermal models. Heat partitioning ratio is identified via calibration experiments for dry, MQL and wet grinding cases with SiC M 80 and Alumina 60 M wheels (workpiece material: AISI 1050 steel).

- By using the developed temperature model, a methodology to predict workpiece surface burn is utilized. Calculated shear stress and shear angle per abrasive grit are used in the primary and secondary shear zone energy equations in order to determine the chip temperature which is thrown out from the cutting zone. As burning of the workpiece is initiated, grinding forces increase with metallic particle adhesion to the abrasive wheel. Force monitoring method is developed to detect the burn initiation.
- An initial approach for dynamics of the grinding process is presented. Both single tooth and multiple teeth for abrasive wheel are presented and compared. It is believed that the idea of modeling the abrasive wheel as a milling cutter tool with multiple teeth is an adequate approach to handle the non-linear and stochastic nature of the grinding processes.

REFERENCES

- [1] Malkin, S., 1989, Grinding Technology: Theory and Applications Machining with Abrasives, West Sussex. Ellis Horwood Limited.
- [2] Tönshoff H., Peters J., 1992, Modelling and Simulation of Grinding Processes. CIRP Annals – Manufacturing Technology. Vol.41/pg 677-688.
- [3] Brinksmeier, E., Aurich J., 2006, Advances in Modelling and Simulation of Grinding Processes. Vol.55/pg 667-696.
- [4] Lal, G.K., Shaw, M. C., 1975, The Role of Grain Tip Radius in Fine Grinding. Journal of Manufacturing Science and Engineering. Vol.97(3)/pg. 1119-1125.
- [5] X. Zhou, F. Xi., 2002, Modeling and predicting surface roughness of the grinding process, International Journal of Machine Tools & Manufacture. Vol.42/pg. 969-977.
- [6] R. Hecker, I. Ramoneda, S. Liang., 2003, Analysis of wheel topography and grit force for grinding process modelling, Journal of Manufacturing Processes. Vol.5/pg. 13-23.
- [7] S. Agarwal, P.V. Rao., 2010, Modeling and prediction of surface roughness in ceramic grinding, International Journal of Machine Tools & Manufacture Vol.50/pg. 1065-1076.
- [8] X. Zhou, F. Xi., 2002, Modeling and predicting surface roughness of the grinding process, International Journal of Machine Tools & Manufacture Vol.42/pg. 969-977.
- [9] Y.D. Gong, B. Wang, W.S. Wang., 2002, The simulation of grinding wheels and ground surface roughness based on virtual reality technology, Journal of Materials Processing Technology Vol.129/pg. 123-126.
- [10] A.O. Mohamed, R. Bauer, A. Warkentin., 2013, Application of shallow circumferential grooved wheels to creep-feed grinding, Journal of Materials Processing Technology. Vol.213/pg. 700-706.
- [11] Y. Liu, A. Warkentin, R. Bauer, Y. Gong., 2013, Investigation of different grain shapes and dressing to predict surface roughness in grinding using kinematic simulations. Journal of the International Societies for Precision Engineering and Nanotechnology. Vol.37/pg. 758-764.
- [12] Fan X, Miller M., 2006, Force analysis for grinding with segmental wheels. Machining Science and Technology: An International Journal. Vol.10/pg 435-455.
- [13] Johnson E, Li R, Shih A., 2008, Design of experiments based force modeling of the face grinding process. Transactions of NAMRI/SME. Vol.36/pg 241-248.

- [14]Durgumahanti U, Singh V, Rao P., 2010, A new model for grinding force prediction and analysis. *Int. Journal of Machine Tools & Manufacture*. Vol.50/No.3
- [15]Chang H, Wang J., 2008, A stochastic grinding force model considering random grit distribution. *Int. Journal of Machine Tools & Manufacture*. Vol.48/No.12&13
- [16]Hecker R, Liang S, Wu X., 2007, Grinding force and power modeling based on chip thickness analysis. *Int. Journal of Advanced Manuf. Tech*. Vol.33/pg449,459
- [17]Rausch S, Odendahl S, Kersting P, Biermann D., Zabel A., 2012, Simulation-based Prediction of Process Forces for Grinding Free-formed Surfaces on Machining Centers. 3rd PMI. *Procedia CIRP*. Vol.4/pg 161-165.
- [18]Koshy P., Iwasaki A., 2003, Surface Generation with Engineered Diamond Grinding Wheels: Insights from simulation. *CIRP Annals – Manufacturing Technology*. Vol.52/pg 271-274.
- [19]Malkin, S., and Guo, C., 2007, Thermal Analysis of Grinding, *CIRP Ann*. Vol.56/pg. 760-782.
- [20]Jaeger, J.C., 1942, Moving Sources of Heat and the Temperature at Sliding Contacts, *Journal and Proceedings of the Royal Society of New South Wales*, Vol.76/pg. 203-224.
- [21]Outwater, J. O., and Shaw, M. C., 1952, Surface Temperatures in Grinding, *Transactions of ASME*. Vol.74/pg. 73–86.
- [22]S C., Salmon., 1992, *Modern Grinding Process Technology*. New York. McGraw-Hill.
- [23]Mohamed, O., Warkentin, A., Bauer, R., 2012. Variable heat flux in numerical simulation of grinding temperatures, *International Journal of Advanced Manufacturing Technology*, Vol.63/pg. 549-554.
- [24]Shen, B., Xiao, G., 2011, A Heat Transfer Model Based on Finite Difference Method for Grinding, *Journal of Manufacturing Science and Engineering*. Vol.133/ pg. 1-10.
- [25]Shen, B., Xiao, G., 2008, Thermocouple Fixation Method for Grinding Temperature Measurement, *Journal of Manufacturing Science and Engineering*. Vol.130/pg. 1-8.
- [26]Lavine, A.S. 2000, An Exact Solution for Surface Temperature in Down Grinding. *Int. Journal of Heat Mass Transfer*. Vo.43/pg. 4447-4456.
- [27]Tahlivian, A.M., Champlaud, H., Liu, Z., Hazel, B., 2013, Study of Workpiece Temperature Distribution in the Contact Zone During Robotic Grinding Process Using Finite Element Analysis, 8th CIRP Conference on Intelligent Computation in Manufacturing Engineering, *Procedia CIRP*. Vol.12/pg. 205-210.

- [28]J. Jiang, Q. Ge, 2008, 2D/3D ground surface topography modeling considering dressing and wear effects in grinding process, *International Journal of Machine Tools & Manufacture*. Vol.74/pg. 29-40.
- [29]G. Warnecke, U. Zitt., 1998, Kinematic simulation for analyzing and predicting high-performance grinding processes, *Annals of the CIRP*. Vol.47(1)/pg. 265-270.
- [30]Pombo I., Sanchez J., 2012, Contact Length Estimation in Grinding Using Thermocouple Measurement and Numerical Simulation. *Int. Journal of Advanced Manuf. Tech*. Vol.59/pg. 83-91.
- [31]Wang, W.P., 1988. Solid Modeling for Optimizing Metal Removal of Three-dimensional NC End Milling. *Journal of Manufacturing Systems*. Vol.7(1)/pg. 57-65.
- [32]Lin, G.C.I, Oxley, P.L.B, 1972, Mechanics of Oblique Machining: Predicting Chip Geometry and Cutting Forces from Work Material Properties and Cutting Conditions. *Proceedings of the Institution of Mechanical Engineers*, Vol.186/pg. 813-820.
- [33]Russel, J.K., Brown, R.H., 1966, The Measurement of Chip Flow Direction. *International Journal of Machine Tool Design and Research*. Vol.6/pg. 129-138.
- [34]Zorev, N.N, 1966, *Metal Cutting Mechanics*. Pergamon Press.
- [35]Oxley, P.L.B, 1989, *The Mechanics of Machining*, Ellis Horwood Limited.
- [36]Whitfeld, R.C., 1986, *A Mechanics of Cutting Approach for the Prediction of Forces and Power in Some Commercial Machining Operations*. PhD Thesis, University of Melbourne.
- [37]Armarego, E.J.A, Brown, R.H., 1969, *The Machining of Metals*, Prentice-Hall.
- [38]Budak, E. 1994, *Mechanics and Dynamics of Milling Thin Walled Structures*, PhD Thesis, The University of British Columbia.
- [39]Shaw., M.C., Cook., N.H, Smith, P.A, 1952, The Mechanics of Three Dimensional Cutting Operations. *Transactionf of ASME Journal of Applied Mechanics*. Vol.74/pg. 1055-1064.
- [40]Armarego, E.J.A, Epp, C.J., 1970, An Investigation of Zero Helix Peripheral Up-Milling. *International Journal of Machine Tool Design and Research*. Vol.10/pg. 273-291.
- [41]Yellowley, I., 1985, Observation of the Mean Values of Forces, Torque and Specific Power in the Peripheral Milling Process. *International Journal of Machine Tool Design and Research*. Vol.25(4)/pg. 337-346.
- [42]Celebi, C, Ozlu, E., Budak, E. 2013. Modeling and Experimental Investigation of Edge Hone and Flank Contact Effects in Metal Cutting. 14th CIRP Conference on

- Modeling of Machining Operations (CIRP CMMO), *Procedia CIRP*. Vol.8/pg. 194-199.
- [43] A. Molinari., D. Dudzinski., 1992, Stationary shear bands in high speed machining, *Comptes Rendus Acad. Sci.*, Vol.315 Serie II/pg. 399-405.
- [44] D. Dudzinski., A. Molinari., 1997, A modeling of cutting for viscoplastic materials. *Int. J. Mech. Sci.*, Vol.39/24/pg. 369-389.
- [45] E. Ozlu., A. Molinari., E. Budak., 2010, Two zone analytical contact model applied to orthogonal cutting. *Machining Science and Technology*, Vol.14:3/pg. 323-343.
- [46] M.E. Merchant., 1994, *Basit Mechanics of the Metal Cutting Process*, Transactions of ASME Journal of Applied Mechanics. Vol.A/pg. 168-175.
- [47] S.P.F.C, Jaspers., J.H. Dautzenberg., 2002, Material Behaviour in conditions similar to metal cutting: Flow Stress in the Primary Shear Zone. *Journal of Materials Processing Technology*. Vol.122/pg. 322-330.
- [48] Augustine, U., and Olisaemeka, N., 2013, Evaluation of Tool and Chip Temperature during Machining Process Using Numerical Method. *The International Journal of Engineering and Science*, Vol. 2/pg. 66-79.
- [49] Lazoglu, I., and Altintas, Y., 2002, Prediction of Tool and Chip Temperature in Continous and Interrupted Machining. *International Journal of Machine Tools & Manufacture*, Vol. 42/pg. 1011-1022.
- [50] Aslan, D., Budak, E. 2014, Semi-analytical Force Model for Grinding Operations. 6th CIRP International Conference on High Performance Cutting, HPC 2014, *Procedia CIRP*. Vol.14/pg. 7-12.
- [51] Park, H, W., Liang, S, Y., 2009, Force Modeling of Microscale Grinding Process Incorporating Thermal Effects, *International Journal of Advanced Manufacturing Technology*. Vol. 44/pg. 476-486.
- [52] Wojtas, A., Suominen, L., Shaw, B., 1998, Detection of Thermal Damage in Steel Components After Grinding Using the Magnetic Barkhausen Noise Method, *Proceedings of 7th European Conference on Non-destructive Testing*. Vol. 3, No.9, Copenhagen.
- [53] Tlustý, J., Polacek, M. 1963, The Stability of Machine Tools Against Self Excited Vibrations in Machining. *Int. Research in Production Engineering*, ASME. Pg. 465-474.
- [54] Tobias, S.A., Fishwick, W., 1993, A New Theoretical Approach for the Prediction of the Machine Tool Chatter in Milling. *ASME J. Eng. Incl.*, Vol 115/pg. 1-8.

- [55] Budak, E., Altintas, Y., 1998, Analytical Prediction of Chatter Stability in Milling-Part I: General Formulation, Part II: Application to Common Milling Systems, *ASME J. Dyn. Sys. Meas. Control.* Vol. 120/pg. 22-36.
- [56] Yang, Y., Lin, J., Xu, S., 2012, Surface Grinding Machine Stability Characteristics Limited Prediction. *Mechanical Engineering Research.* Vol. 2/pg. 114-119.
- [57] Park, H. W., 2008, Development of Micro-Grinding Mechanics and Machine Tools, PhD Thesis, Georgia Institute of Technology.
- [58] Moufki, A., Devillez, A., Dudzinski, D., Molinari, A., 2004, Thermomechanical modelling of oblique cutting and experimental validation. *International Journal of Machine Tools and Manufacture.* Vol. 44/pg. 971-989.
- [59] Altintas, Y., Budak, E., 1995, Analytical Prediction of Stability Lobes in Milling. *Annals of the CIRP.* Vol. 44/pg. 357-362.
- [60] Budak, E. and Ozlu, E., Development of a Thermomechanical Cutting Process Model for Machining Process Simulations, *Annals of the CIRP.* Vol. 57/1/pg. 97-100, 2008.
- [61] Hou, Z., Komanduri, R., 2003, On the Mechanics of the Grinding Process – Part I. Stochastic Nature of the Grinding Process. *International Journal of Machine Tools and Manufacture.* Vol. 43/pg. 1579-1593.
- [62] Rowe, W. B., Black, S. C. E., Morgan, M. N., Qi, H. S., 1997, Grinding Temperature and Energy Partitioning. *Proceeding Royal Society, Part A.* Vol. 453/pg. 1083-1104.
- [63] Rowe, W. B., Morgan, M. N., Qi, H. S., Zheng, H. W., 1993, Effect of Deformation on the Contact Area in Grinding. *Annals of the CIRP.* Vol. 42/pg. 409-412.
- [64] Hacker, R. L., 2002, Part Surface Roughness Modeling and Process Optimal Control of Cylindrical Grinding. PhD Thesis, Georgia Institute of Technology.
- [65] König, W., 1975, Properties of Cutting Edges Related to Chip Formation in Grinding, *Annals of the CIRP.* Vol. 24/1/pg. 231-236.
- [66] Ramanath, S., Shaw, M. C., 1988, Abrasive Grain Temperature at the Beginning of a Cut in Fine Grinding. *ASME Journal of Engineering for Industry.* Vol. 110/pg. 15-18.
- [67] Martellotti, M.E., 1945, An Analysis of the Milling Process. Part II: Down Milling, *Transactions of the ASME,* Vol. 67/pg. 233-251.
- [68] Philippon, S., Sutter, G., Molinari, A., 2004, An experimental study of friction at high sliding velocities. *Wear,* Vol. 257/pg. 777-784.
- [69] Jiang, J., Ge, P., Hong, J., 2013, Study on micro-interacting mechanism modeling in grinding process and ground surface roughness prediction. *International Journal of Advanced Manufacturing Technology,* Vol. 67/pg. 1035-1052.

